The Dissertation Committee for Yu-Yen Huang Certifies that this is the approved version of the following dissertation:

Immunomagnetic Microfluidic Screening System for Circulating Tumor Cells Detection and Analysis

Committee:

John X.J. Zhang, Supervisor

Andrew Dunn

Pengyu Ren

Konstantin Sokolov

Haley Tucker

Immunomagnetic Microfluidic Screening System for Circulating Tumor Cells Detection and Analysis

by

Yu-Yen Huang, B.S.; M.S.

Dissertation

Presented to the Faculty of the Graduate School of

The University of Texas at Austin

in Partial Fulfillment

of the Requirements

for the Degree of

Doctor of Philosophy

The University of Texas at Austin

December 2013

Dedication

Dedicated to my wife Hsin-Chieh Wang

and my beloved family

Acknowledgements

I would like to give my sincere appreciation to my supervisor, Professor X.J. Zhang, for his invaluable guidance, helpful advice, and full support for my research in past couple years here at the University of Texas at Austin. As the Chinese saying goes, "Once a teacher, a lifetime father."

I would also want to thank my committee members, Dr. Andrew Dunn, Dr. Pengyu Ren, Dr. Kostantin Sokolov, and Dr. Haley Tucker for insightful comments and suggestions on my dissertation research.

Special thanks to my collaborators, Dr. Johnathan Uhr, Dr. Eugene Frenkel, Nancy Lane, Dr. Michael Huebschman, and Dr. Huaying Liu at the University of Texas at Southwestern Medical Center for providing knowledge and great help, and giving substantial support on the collaborated project. In addition, I want to thank Mohammed Alkatan at Dr. Tanaka's group for the help in the sample preparation.

I would like to give a special thank to my great mentor, Dr. Kazunori Hoshino, in the Zhang Research group. He is such a great mentor that I have learned a lot from him in respect of leading and managing a research project. I also want to thank all my amazing previous and current lab mates, Dr. Ashwini Gopal, Dr. Yuyan Wang, Dr. Dajing Chen, Dr. Tushar Sharma, Dr. Youmin Wang, Dr. Lingyun Wang, Dr. Daghan Gokdel, Andrew Horton, Youngkyu Lee, Gauri Bhave, Zhiguo Wang, Ellen Blinka, Kathryn Loeffler, and Stephanie Diong. Special thanks to Peng Chen, Frank Wu, Elaine Ng, Oanh Hoang, Kaarthik Rajendran, Zach Brownlee, and Nick Triesault for the great efforts and valuable contributions to the project. I had a wonderful time here in the lab. I will miss y'all.

I need to thank my best friend and mentor, Dr. Chi-Han Chiou. We have known each other for more than ten years. He helped me tremendously to reach this point in my career. Also, I appreciate Dr. James Chen's invaluable helps since I started my life here in USA.

Most importantly, I want to express my gratitude to my beloved family, especially my daddy, mommy, and my sister. I want to share the moment with you. I do cherish your unconditional love, patience, and support to me.

Finally, I thank my wife for always being there with me. Your support, encouragement, and love made all these achievements happened. I am delighted to share the achievement, which is a good beginning of our journey, with you.

I am so lucky to have precious guidance, timely support, and continuous inspiration from all of you. This accomplishment is built upon your efforts. Some of your names may not be mentioned here even I have tried so hard not to lose any. Please accept my sincere apology and big thank-you.

"What starts here changes the world."

Yu-Yen Huang

The University of Texas at Austin

December 2013

Immunomagnetic Microfluidic Screening System for Circulating Tumor Cells Detection and Analysis

Yu-Yen Huang, Ph.D.

The University of Texas at Austin, 2013

Supervisor: John X.J. Zhang

Circulating tumor cells (CTCs) are known to escape from the primary tumor site and may settle down at the distant organ to grow a second tumor. CTCs are one of causes initiating carcinoma metastasis. Detection of CTCs has been considered to be valuable for cancer management, including diagnosis, prognosis, and clinical treatment management. However, efficient isolation, enumeration, characterization, and genetic analysis of CTCs in whole-blood samples from cancer patients are very challenging due to their extremely low concentration and rare nature (per CTC in blood cells is $1{:}10^6$–10^9). With the increasing worldwide death rate associated with cancer, there is a desperate demand for a high-sensitivity, high-throughput, and low-cost detection and separation system.

My doctoral research focused on the design and fabrications of the screening system for the detection of CTCs with further analysis of captured CTCs, such as immunofluorescence staining and fluorescence *in-situ* hybridization (FISH). The distinct significance of this research is that the development of the computer-controlled rotational holder with a series of six inverted microfluidic chips reduced the cost by significantly reducing the consumption of magnetic carriers (25% of the consumed amount used in the commercial CellSearch® system), increasing the capture efficiency by manipulating the

blood sedimentation in the microchannel, enhancing the system stability by integrating the micromagnets on the plain glass slide substrate, and achieving high throughput because of the high flow rate (2.5 mL/hr) and large screening volume (screening up to six chips in parallel with each containing 2.5 mL of blood). Immunofluorescence staining and the FISH method have been performed to prove the capability of the system. In addition, the system has been successfully applied for patient samples screening.

The incorporation of micromagnets has demonstrated that micromagnets provide localized magnetic forces to scatter the target cancer cells and free nanoparticles throughout the whole channel substrate to increase the channel space usage by 13%. Four cancer cell lines, including COLO 205 (colorectal cancer), SK-BR-3 (breast cancer), MCF-7 (breast cancer), and PC3 (prostate cancer), were spiked in blood samples from healthy donors to verify high capture efficiency of the developed system. On average, over a 97% capture rate was demonstrated for all cell lines. Moreover, the developed screening system has been successfully screened over 40 patient samples, including metastatic lung cancer, breast cancer, prostate cancer, and colorectal cancer. After capture of CTCs, immunofluorescence staining was used to identified the captured cancer cells and the FISH method was performed to characterize the isolated cancer cells by studying the gene expression of CTCs from breast cancer.

The proposed automated immunomagnetic microchip-based screening system shows high capture efficiency (average 97% for four spiked cell lines), high throughput (15 mL of blood sample per screening), high sensitivity, high specificity, and low nanoparticle consumption (75% less than CellSearch® system). The screening system provides great promise as a clinical tool for early cancer diagnosis, diagnosis, personalized therapy, and treatment monitoring.

Table of Contents

List of Tables

List of Figures

Chapter 1

Background and Introduction

According to the world cancer statistics reported by the International Agency for Research on Cancer (IARC), which is the specialized agency of the World Health Organization (WHO), global cancer deaths increase from 7.6 million in 2008 to 8.2 million in 2012. In the United States, cancer is the second most common cause of death, accounting for nearly one in every four deaths. It is imperative to control the disease progression before it consumes the life of a patient. Early diagnosis and detection are therefore keys to early cancer prevention. Recent years witnessed a massive and rapid growth in the cancer diagnostics market. This blooming market environment provides the perfect opportunity for our technology to penetrate target market segments where it will grow and establish a prominent market share. Recent market analysis from Business Wire reported a global market for the next-generation cancer diagnostics market worth $776 million in 2010 and that it is projected to grow to $5.3 billion by 2015. According to Business Wire, the cellular analysis market was worth $10 million in 2010 and is expected to increase at a 95.4% compounded annually growth rate, eventually reaching a market worth of $296 million in 2015 [1].

Therefore, a tool for the diagnosis and prognosis for cancer is in urgently needed. Current commercially available rare-cancer-cell detection systems have poor positivity of results, even for metastatic cases, and are typically used for selection and numeration only, not to mention that the high costs associated with these tests greatly limits patient market exposure. Therefore, a highly sensitive, high-throughput, and low-cost screening system for cancer disease monitoring is the most affordable solution to the urgent needs in developing and developed countries.

Here, we briefly introduce existing methods and systems for the screening of rare cells for further analysis. We start by discussing from the macroscopic cell detection systems such as the magnetic-activated cell sorting system followed by a discussion of the scaling law of miniaturization towards microfluidic chip-based immunomagnetic assay for cell separation. We then discuss the fundamentals of the flow field and magnetic field in the microchannel for the design and development of the screening device. Related design concepts, principles, and microfabrication techniques are presented and evaluated. Characterization and calibration of the screening system by the spiked experiments are then presented, and results of applying the system for the patient samples are shown in the thesis.

1.1 METASTATIC AND CIRCULATING TUMOR CELL

1.1.1 Metastatic cancer

Metastasis is the major cause of carcinoma-related death in cancer patients. Metastasis usually occurs via blood vessels and the lymphatic system. During this metastatic process of cancer metastasis, cancer cells escape from a primary tumor site and circulate through the lymphatic system and the bloodstream to other, distant organs, leading to the development of a second, solid tumor.

Cancer type	Main sites of metastasis
Breast cancer	Bone, brain, liver, and lung
Colorectal cancer	Liver, lung, and peritoneum
Lung cancer	Adrenal gland, bone, brain, liver, and other lung
Prostate cancer	Adrenal gland, bone, liver, and lung

Table 1.1: Common sites of metastasis for four types of cancer. [2]

Stephen Paget, an English surgeon, introduced the idea of a “seed and soil” theory in 1889 to describe the metastasis of cancer, in which a cancer cell was considered to be the seed while the organ microenvironments were considered to be soil [3-6]. Table 1.1 shows the common main sites of metastasis for four types of cancer, including breast cancer, colorectal cancer, lung cancer, and prostate cancer [2]. We mainly use those breast cancer cell line, colorectal cancer cell line, and prostate cancer cell line for spiked experiments here in the thesis.

1.1.2 Circulating tumor cells

Cells shed from the primary tumor site and circulating in the peripheral bloodstream are known as circulating tumor cells (CTCs). CTCs can potentially trigger the growth of additional, distant organ tumor sites, and appear to get involved in the mechanism and development of recurrent and metastatic disease.

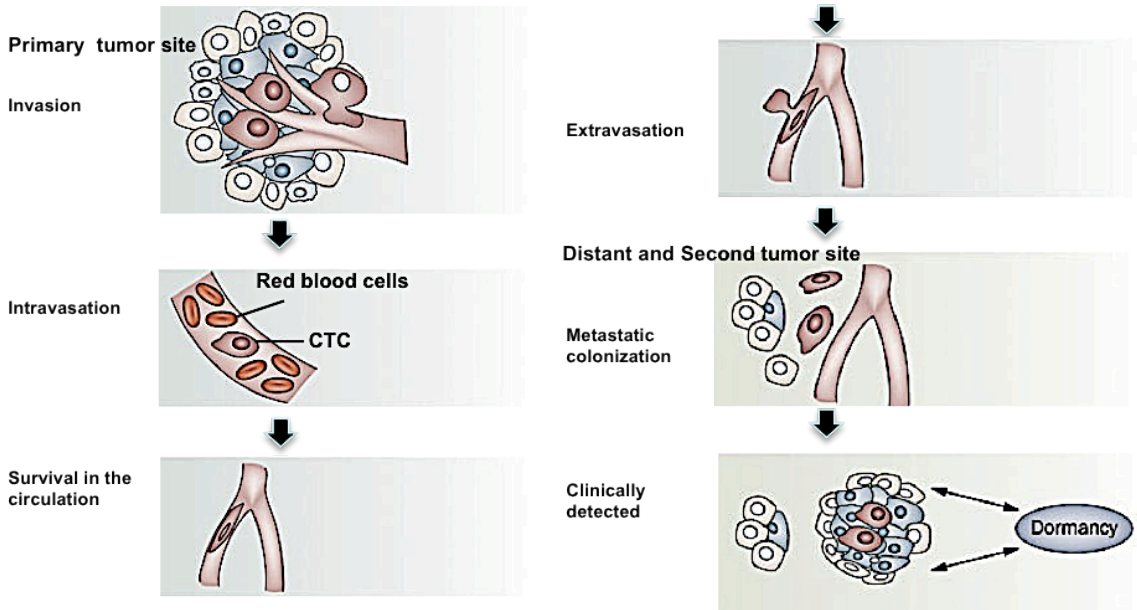

Figure 1.1: The steps of the metastatic cascade. [7]

Figure 1.1 shows the metastatic steps of cancer. Viable CTCs found in patient blood can potentially be the major causes of carcinoma metastasis, during which CTCs undergo a series of steps of local invasion, intravasation, circulation, arrest, extravasation, proliferation, and angiogenesis [8].

CTCs in the blood sample have been considered an important indicator of carcinoma progression and metastasis. Hence, accurate information on the enumeration of CTCs is critical to cancer diagnosis, prognosis, and therapeutic response monitoring [9, 10]. Capture and molecular characterization of CTCs at an early stage generate immediate clinical impact by providing an important tool to expand and delineate risk assessment, treatment selection, response monitoring, and development of novel therapies.

Due to the rarity of CTCs in the peripheral blood sample, only one CTC can be found in 1 mL of whole-blood sample containing a billion blood cells [11, 12]. Therefore, it is highly challenging for the isolation/enrichment, molecule characterization, and downstream analysis of cancer cells with such a low concentration of CTCs in a whole-blood sample. An effective CTCs detection system with high sensitivity, high throughput, high purity, and low cost is required for the advancement of both biological and clinical cancer studies.

Some biomarkers are commonly used for detecting cancer cells shed from different tumor sites. Table 1.2 shows some of the common ones for detection of several different tumor sites. Epithelial cell adhesion molecule (EpCAM) is commonly expressed in most human epithelial carcinomas. Therefore, EpCAM has been used as a diagnostic and prognostic tool for various cancers. In this thesis, we mainly use EpCAM as a surface biomarker expressed on the cancer cell for the development of a CTC detection system. In addition, the monoclonal anti-EpCAM antibody is used to modify the surface of magnetic carriers to tag the target cancer cells for cell separation.

Biomarker	Tumor site
EpCAM	Breast, Colorectal, Prostate, Lung, and Bladder
HER-2	Breast and Gastric
EGFR	Breast, Colorectal, Gastric
MUC-1	Breast, Colorectal, Prostate, and Ovarian
CD146	Breast
PSA	Prostate
EphB4	Breast, Colorectal, Head, and Neck
CEA	Breast, Colorectal, Gastric, and Pancreatic
KRAS	Colon

Table 1.2: Common biomarkers for detecting different tumor sites. [13]

The presence of CTCs in a blood sample is considered as an important indicator of many types of cancer that appear to be the mechanism of development for recurrent and metastatic cancer disease. The capture and genetic-information acquisition at the molecule scale of CTCs provide an important tool to expand and delineate risk assessment, treatment selection, response monitoring, and development of novel therapies [14, 15].

1.2 METHODS FOR RARE CELL ISOLATION

Emerging technologies for CTCs enrichment have raised a lot of attention in the scientific community and biotechnology industry around the world over the past decades. Various methods and systems have been proposed and have demonstrated the successful detection of CTCs in many reviews [16-23]. Based on the proposed detection principles, those mechanisms can be categorized into two main parts as follows.

(1) Separation based on physical parameters:

- Sizes and density gradients [12, 16-21]

- Hydrodynamic separation [24-27]
- Dielectrophoretic separation [28, 29]

(2) Affinity mediated separation:

- Immunoassay [30, 31]
- Immunomagnetic separation [9, 32-35]).

1.2.1 Fluorescence-activated cell sorting

Fluorescence-activated cell sorting (FACS) is a specialized type of flow cytometry. FACS has been widely used for sorting a heterogeneous mixture of cells based on the fluorescence signals. A number of miniaturized FACS systems based on microfluidic device have been developed [36, 37]. The FACS method is limited in that it can be used to sort cells only with large subpopulations that lack the sensitivity to separate rare cells.

1.2.2 Magnetic-activated cell sorting

Magnetic-activated cell sorting (MACS) assay has been extensively used for cell separation by applying magnetic force to separate cancer cells tagged with magnetic carriers [38], such as magnetic microbeads or nanoparticles. The magnetic tags are usually attached specifically to cancer cells through antibody–antigen interaction, leaving behind other nonparticle-labeled normal blood cells. The magnetic field source acting on those magnetic tags can be either permanent magnets [34] or electromagnets [39]. Permanent magnet provides static magnetic field, while electromagnet generate tunable magnetic field. Immunomagnetic assay has several advantages, such as high selectivity, high specificity, high throughput, great tunability, and good integration. Therefore, immunomagnetic assay is more suitable for rare CTC separation.

For selectivity, immunomagnetic assay has good sensitivity due to the antibody–

antigen bonding as the affinity-mediated immunoassay. Currently, most of the immunoassays rely solely on the overexpression of one common biomarker—the epithelial adhesion molecule (EpCAM). However, EpCAM may be down regulated during metastatic steps. Therefore, the addition of the multiple types of antibodies coated on the magnetic tags specific for multiple cancers can thus increase the separation sensitivity. High capture rates of A-431 (skin cancer cell) using EpCAM/EGFR, SK-BR-3 (breast cancer cell line) using EpCAM/HER-2, and BT-20 (breast cancer cell line) using EpCAM/MUC1 have been successfully demonstrated [40, 41].

For specificity, immunomagnetic assay increases the capture contrast between magnetic tags—labeled and non-labeled cells in terms of the surface attachment by using the magnetic force for retaining the target cells. Higher shear stress/flow rate can be applied during the flushing steps.

Affinity-mediated immunoassay is dependent on the successful contact of CTCs and surface biomarkers. Unlike affinity-mediated immunoassay, immunomagnetic assay can magnetically attract cells within a broader spatial domain to achieve high throughput. Therefore, higher flow rates can be compromised without losing the separation efficiency [34].

By using the electromagnet as a magnetic field source, magnetic field can be accurately adjusted for the tunability function of immunomagnetic assay comparing to the adhesion-based separation method. Furthermore, the magnetic field distribution and the field intensity can be fine-tuned specifically for different cell types and magnetic carrier properties.

In addition, immunomagnetic assay can be incorporated with other proposed separation methods to show that the integration capability in that magnetic field can be introduced without directly contacting cells. The integration capability has been demonstrated by integrating immunomagnetic assay with deterministic flow and inertia

focusing in serial to significantly increase the separation efficiency by removing red blood cells (RBCs), platelets, and other blood components [42].

A large amount of effort has been dedicated to inventing different types of immunomagnetic assay for cell separation in the past few decades.

The conventional magnetic-activated cell isolation system is a manual method for screening process. Bulky permanent magnets are arranged with quadrupole to magnetically attract magnetic tag-labeled cells in a radical direction toward the sidewall of the tube (e.g., conical tube and Eppendorf tube), which is usually used to store the blood sample before the separation process [43]. Several commercial MACS systems have been introduced to the market that high magnetic field gradient was generated in column tube. Commercial magnetic-activated cell sorting (MACS) systems have been developed in which high magnetic field gradient was generated in a column tube [9, 32].

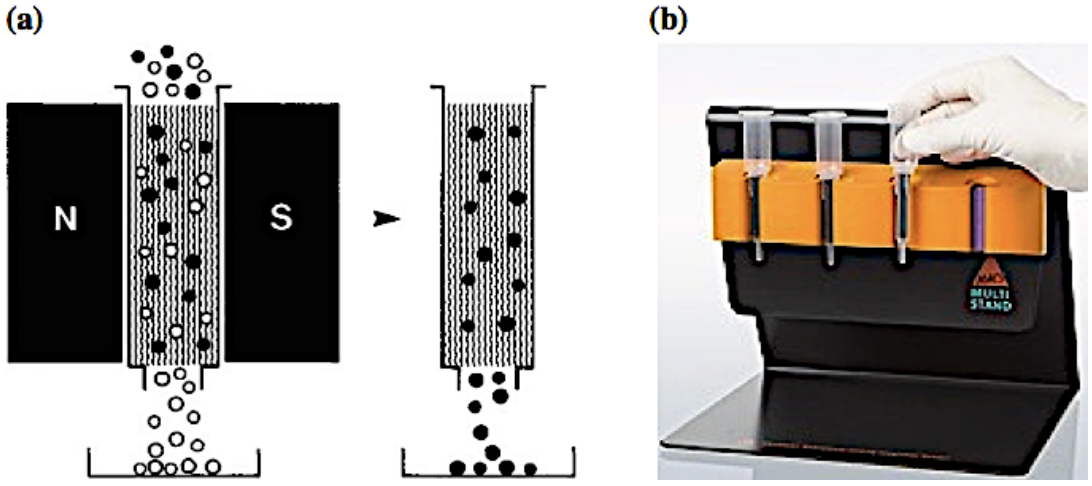

Figure 1.2: MACS system. Superparamagnetic beads were used to tag cells. (a) Principle of MACS. Bead-labeled cells were attracted to the sidewall of the tube by the applied external magnetic field while unlabeled blood cells were eluted. Black dots indicate superparamagnetic beads, and white dots indicate unlabeled blood cells. (b) Commercial product of MACS [32].

Target cells labeled with magnetic microbeads were magnetically attracted to the tube sidewall, whereas unlabeled cells were eluted. Once the external magnetic field was removed, the microbead-labeled cells could be released and collected [32]. The principle of the MACS system is shown in the Figure 1.2(a). The commercially available product is also shown in Figure 1.2(b). However, the conventional MACS system for cell separation is a time-consuming process with low throughput, especially for rare-cell separation, because of its manual operating procedures and the limited magnetic field intensity.

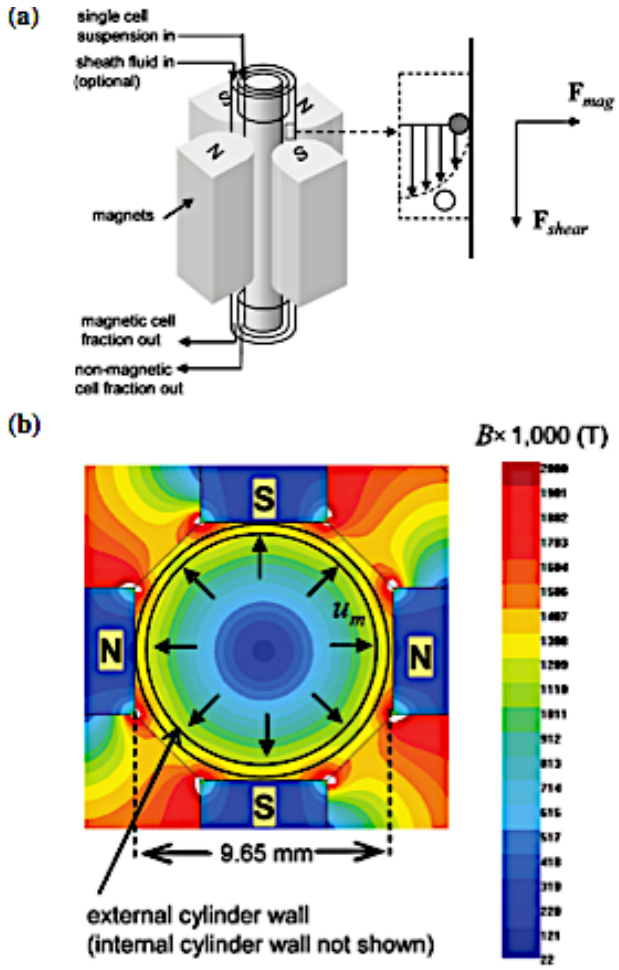

Figure 1.3: (a) Schematic of the quadrupole magnetic flow sorter (QMS) system. (b) Top view of the magnetic field simulation distributed in the tube. [44]

Figure 1.3 shows one example of MACS. Figure 1.3(a) shows the schematic of the quadrupole magnetic flow sorter system. Four magnets are placed in an alternative arrangement of polarity configuration (N-S-N-S) and exert a radial magnetic force on the magnetic carrier-tagged cells, which is represented by the gray circle. The simulated magnetic field distributed in the quadruple tube is shown in Figure 1.3(b) [44]. The magnetic field in the center is extremely low longitudinally in the tube, so magnetic carrier-tagged cells may escape from the tube instead of being magnetically attracted to the sidewall of the tube.

Subsequently, a design of the MACS system called MagSweeper technology was recently introduced in which plastic sheaths covered magnetic rods that were swept through the well to magnetically attract microbead-labeled target cells [33, 45].

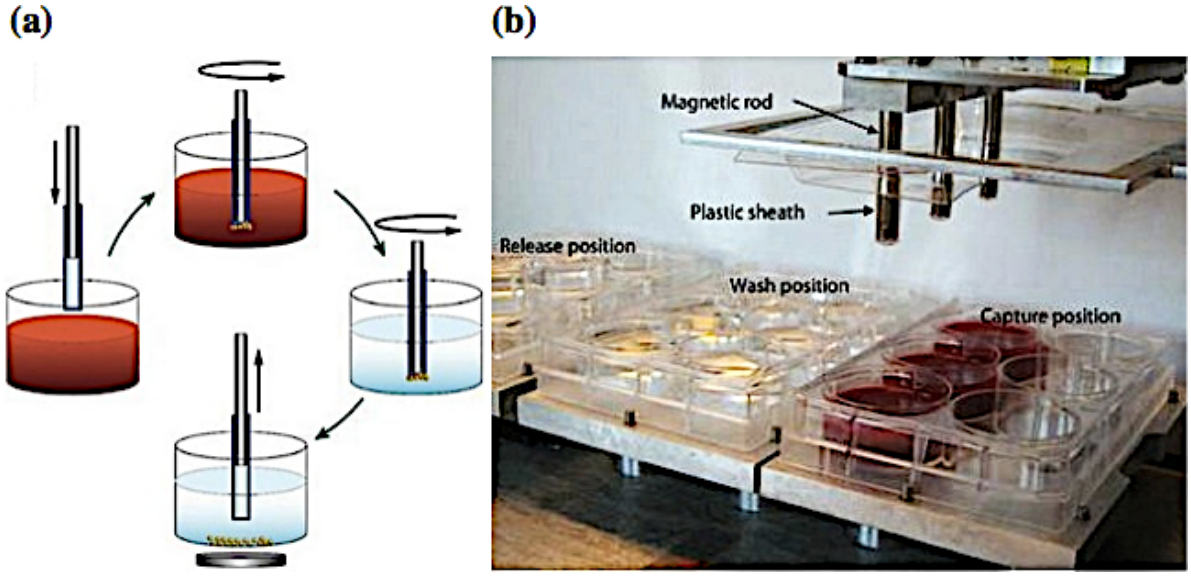

Figure 1.4: (a) Operational schematic of the MagSweeper. (b) Photography of the MagSweeper system used to isolate rare CTCs. [33, 45]

Figure 1.4 shows the operation principles of the developed MagSweeper system.

The blood samples were diluted and then pre-labeled with magnetic particles. Then the samples were loaded into the capture wells. The sheath-covered magnetic rods were swept in the wells, rotating 1.5 mm above the bottoms of the wells. Loosely bound cells were removed while the sheathed rods were being washed. An external magnetic field was applied to facilitate the release of labeled cells and excessive magnetic particles. The sample can process different samples at the same time by using three rods in parallel, as shown in Figure 1.4(a). However, during the screening process, sheaths considerably reduced the magnetic force on the magnetic rods leading to the lower capture efficiency. Figure 1.4(b) shows a photograph of the MagSweeper system.

Targeting CTC detection, a commercial system (Veridex,LLC, Raritan, NJ) was developed, also based on the MACS method. CellSearch® is currently the only system that has been approved by the US Food and Drug Administration (FDA) for clinical diagnostics of breast, colorectal, and lung cancers, as shown in Figure 1.5.

Figure 1.5: FDA-proved CTC detection system, CellSearch® system, including (a) the automated sample preparation system and (b) the MagNest test kit. [46]

Figure 1.5(a) shows the automated sample preparation system. Figure 1.5(b) shows the MagNest kit, which is used for microscopic observation. The commercially available screening system consists of a CellSave™ preservative tube (Immunicon,

Huntingdon Valley, PA) for collection, preservation, and transportation of blood samples. A CellSearch® profile kit (Veridex, LLC, NJ) containing ferrofluids and capture-enhancement reagent was used for the screening. CTCs labeled with ferrofluids conjugated based on EpCAM were enriched from other unlabeled blood cells. A semi-automated microscope was utilized for sample scanning and data acquisition (CellSpotter Analyzer, Veridex, LLC, NJ) [47, 48]. Many papers have been published using CellSearch® to study the correlation of enumarated CTCs level and the survival rates of cancer patients [49-55]. However, the CellSearch® system is primarily limited by its low capture efficiency. Besides, the system re-suspends the captured cells in the original screen solution after fluorescence imaging instead of collecting them. Therefore, no cells can be retrieved, and no further analysis can be done with the captured CTCs.

Conventional magnetic-activated cell sorting systems reveal the inspiring topic of CTC study. As research into CTCs advances, higher requirements are placed on the enrichment techniques [56, 57]. The conventional MACS system is not designed for molecular analysis. In addition, their bulky size and bad portability impose restrictions on their applications for point-of-care biomedical systems. Therefore, new technology is needed to provide better control of the magnetic and hydrodynamic forces acting on the target cells flowing in the channel for enhanced enrichment.

1.2.3 Immunoassay-based separation method

CTCs can be differentiated from other normal blood cells based on the biomarkers expressed on the cell surface. Direct force for cell capture can be provided directly by the affinity ligands coated on the capture surface.

Antibody-antigen interactions display better selectivity than physical properties separations. Affinity mediated immunoassay was first demonstrated by coating the three-dimensional micro posts structures with anti-the epithelial cell adhesion molecule

(EpCAM) antibodies [30]. Figure 1.6 shows a lung cancer cell expressing EpCAM antigen captured by a three-dimensional micropost conjugated with anti-EpCAM antibody.

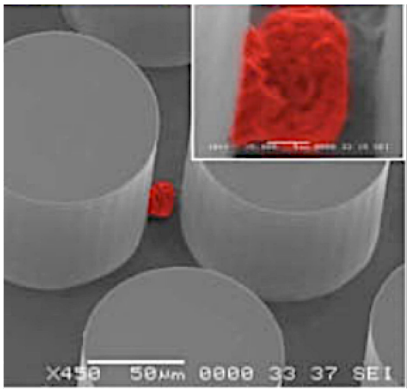

Figure 1.6: SEM image of one NCI-H1650 lung cancer cell captured by a micropost coated with anti-EpCAM. The inset shows a high magnification view of the captured cell. [30]

A number of devices with engineered three-dimensional structures have been proposed to help increase the capture efficiency by taking advantage of the enhanced surface-to-volume ratio [31, 58]. However, shear stress acting upon the captured cells on the surface of the three-dimensional structure may cause damage to or loss of the cells. Therefore, relatively low flow rate limits the affinity-mediated immunoassay of transporting to the capture surface. It is also difficult to select the appropriate flow rate for facilitating the interactions between target cells and surface biomolecules while dissociating the nonspecific bonds and removing non-target cells from the three-dimensional structures.

Fluid-permeable nanoporous membrane structure have been proposed recently to be integrated with the immunoassay to enhance the surface reactions with the target cells and reduce nonspecific bonding [59, 60].

1.2.4 Electrical properties-based separation

Some cell separation methods are performed based on the electrical properties of cells. Cells are polarized by the AC electrical field and controlled by the applied dielectrophoresis (DEP) force. The DEP force applied on the cells is dependent on properties of the AC electrical field, the dielectric of the surrounding fluid medium, and the density of the cells [61]. CTCs and normal blood cells were levitated to different heights and then transported with different flow velocities in the parabolic flow profile. Blood cells move faster near the center of the channel, while CTCs move slower near the surface and are separated [28, 62]. The DEP separation system, which is a label-free method, is suitable for dealing with large amounts of blood samples in a flow-through device so that target cells can be collected for further analysis. However, a larger chamber is required to increase the separation efficiency. In addition, the requirement for the DEP system is an external power supply, which limits the portability of the system for further point-of-care clinical use.

To further improve the separation sensitivity and specificity, antibody–antigen interactions have been adopted to provide addition cell differentiation. Biological recognitions take advantage of the enhanced surface area per unit volume in microstructures to increase the chance of cell adhesion.

1.2.5 Cell separation based on cell physical properties

Label-free separation based on physical properties takes advantage of one or more intrinsic differences of the CTCs' properties (such as size, density, deformability, and electrical charges) that distinguish them from other normal blood cells. For the size-filtration method, the principle is that the carcinoma cells are assumed to be generally larger than other normal blood cells in the blood samples [22, 63, 64]. A filter-based method, which is referred to as isolation by size of epithelial tumor cells (ISET), was

developed to isolate CTCs from the peripheral blood sample [63-65]. A high-density microcavity array was reported to trap target cells on the filter structure by applying negative pressure on the detection system [22]. The deficiency of the filtration method is that target cells easily get clogged on the filter structures along with other blood cells due to low pore density and multiple pore fusion, which lead to low capture efficiency [11, 66, 67]. In order to avoid the cell-clogging issue, lysis of blood cells (e.g., red blood cells) becomes a necessary step before the filtration process. However, lysis of blood cells raises another issue of cell loss.

Based on the similar buoyant density of cells, density gradient centrifugation is applied for the isolation of target cells [68, 69]. The demonstrated maximum capture efficiency of the density gradient centrifugation was 70% [70]. In addition, separation method based on the cell deformability can provide an alternative to the current cell enrichment techniques [18, 71]. The filtration structure may not be able to differentiate between cancers cells that are physically similar to normal blood cells although the filter-based approaches are not limited by the cell types. When the target cells pass through the filtration structure, increasing shear stress may cause potential damage or loss of target cells limiting the system throughput. Therefore, both the filter method and the density gradient centrifugation method lack specificity resulting in low separation efficiency.

Manipulating the hydrodynamic forces on the target cells in a streamline is an alternative to the filtration system for cell separation. Continuous-flow deterministic array was reported to separate blood components based on the hydrodynamic sizes [26].

The asymmetric pinched flow fraction method demonstrates that cells with different sizes and shapes move along different streamlines and can eventually enter different outlets for being collected [72]. Microvortices can be applied to isolate CTCs based on size difference as a biomarker, in which target cells with larger diameters migrate and are enriched in the expansion-contraction trapping reservoirs [25, 73]. The spiral structure of microchannels used the Dean vortex flow presented inherently in the

curvilinear chamber to move larger CTCs against the inner wall and collect them from the inner outlet [74, 75].

The streamline-based separation method can be operated with a high flow rate without significantly increasing the shear stress on the target cells. However, the sample usually needs to be significantly diluted largely before the screening process, which limits the separation efficiency.

1.3 MICROFLUIDIC CELL SORTING SYSTEM

People are now allowed to make miniaturized tools to observe, measure, and manipulate extremely small targets because of the advancement of micro/nanotechnology. For rare cell detections, such microsystems provide precise control of the hydrodynamic flow, transportation, and biological interactions in the microchannel. Combination of immunomagnetic assay and microchip technology has been well established for separation of rare cells.

Microfluidic immunomagnetic assay uses magnetic carriers (e.g., beads/particles) conjugated with specific antibodies to label target cancer cells. The external magnetic field is applied for capturing.

Integration of microchip-based and immunomagnetic assay was proposed for the analytical magnetapheresis, which was reported to compare magnetic properties of iron-rich protein (ferritin) labeled human lymphocyte and magnetite-doped dynabeads [35, 76].

Figure 1.7 shows the system of the analytical magnetapheresis. The samples were stored in a syringe before they were pumped into a carrier medium-filled microchannel, which was placed over permanent magnets, at a controlled flow rate. Magnetized cells and dynabeads were magnetically attracted to the interpolar gap of permanent magnets. The cell sample was permanently fixed and stained on the sample slides for microscopic

analysis. Magnetic susceptibility was measured and calculated by the developed analytical magnetapheresis for the ferritin-labeled lymphocyte and the necessary number of ferritin molecules per lymphocyte for the magnetic separation.

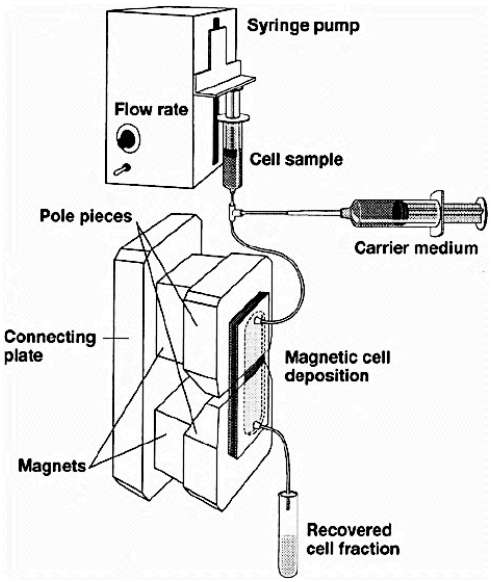

Figure 1.7: Setup of one early analytical magnetapheresis system, which was used to study human lymphocyte. Cells were trapped at the interpolar gap of the magnets. [76]

A microchip system was proposed based on continuous-flow ferrofluid hydrodynamics to sort a mixture of particles and live cells simultaneously. Figure 1.8 shows the microdevice with a stack of four permanent magnets placed close to a microfluidic channel to sort different sizes of cells based on ferrohydrodynamics. The system involved manipulation of cells within ferrofluid suspension under the external magnetic fields in the later part of the microchannel. Escherichia coli (strain MG1655), Saccharomyces cerevisiae (baker's yeast), and two different sizes of fluorescent polystyrene microparticles were screened for the separating experiments. The system demonstrated high capture efficiency (~100%) and high throughput (107 cells per hour)

[77, 78]. For clinical screening, the developed system needs further optimization to increase the separation resolution for cells with smaller differences.

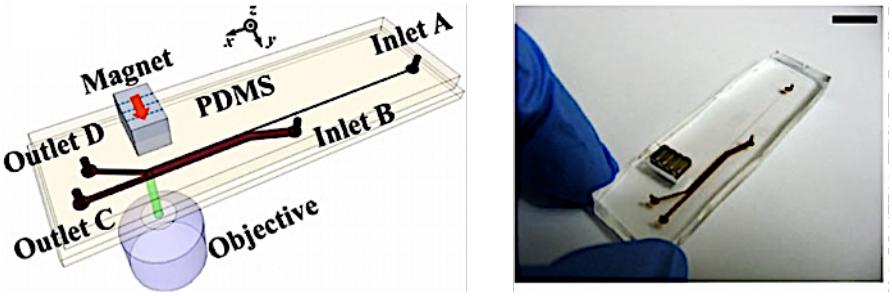

Figure 1.8: Microchip-based immunomagnetic CTC separation system in deflecting mode. Permanent magnets were placed to the sidewall of the microfluidic channel to sort different cell lines into different streamlines and collect them at the end of the channel. [77]

The immunomagnetic assay can be used to retrieve viable CTCs; therefore additional functionalities, such as cell culture, can be fulfilled [79].

The device composed of a tilt-inlet channel with a certain angle in a main microfluidic channel with two rows of dead-end side chambers, as shown in Figure 1.9, to store attracted CTCs and avoid being damaged by shear stress. A permanent magnet was placed outside of the lower row of side chambers to magnetically collect magnetic bead-attached CTCs. The device showed good separation efficiency of 87% using spiked M6C breast cancer cells. Isolated CTCs along with RBCs were cultured for molecular analysis (reverse transcription polymerase chain reaction, RT-PCR) after the lysis of RBCs. The developed system can be used to process large sample volumes, multiple types of CTCs, and other molecules [79].

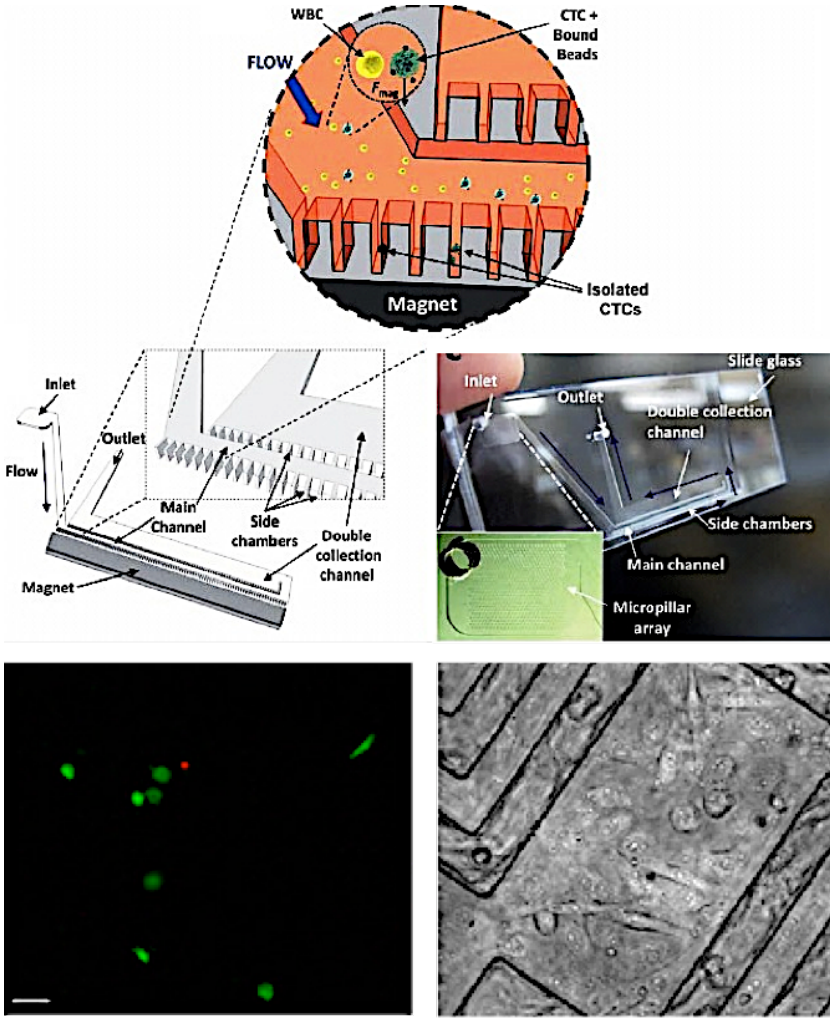

Figure 1.9: Immunomagnetic microchip integrated with cell storage chamber to retrieve and culture CTCs on chip. [79]

As mentioned earlier, immunomagnetic assay can be integrated with other separating mechanisms to demonstrate better isolation capability. A CTC-iChip containing three separation stages of debulking, inertial focusing, and immunomagnetic was introduced for CTC separation [42]. The system incorporated three microfluidic functions to replace RBCs lysis and centrifugation, hydrodynamic sheath flow in flow cytometry, and magnetic-activated cell sorting, as shown in Figure 1.10. The first stage in the developed system was the hydrodynamic size-based filtration that it used an array of micropillar structures in which RBCs, platelets, plasma proteins, free magnetic beads,

and other blood components were discarded through a top outlet. The remaining CTCs and WBCs were then transferred to the second stage for inertial focusing before moving to the third stage where immunomagnetic separation was performed to collect the CTCs through a top outlet. The CTC-iChip was capable of immunomagnetically sorting epithelial and non-epithelial cancer cells in both negative and positive modes. The captured cells were used for further molecular analysis of a single cell. The microfluidic device performed high capture efficiency for different cancer cell lines expressing different EpCAM levels.

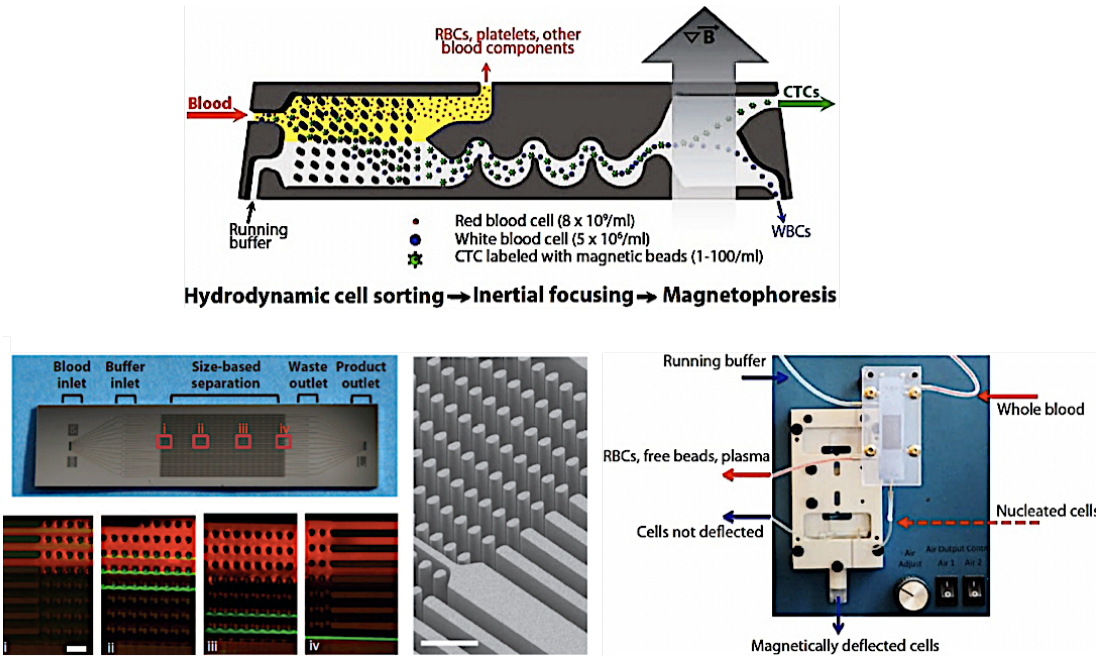

Figure 1.10: Hybrid immunomagnetic microchip for CTC detection, including hydrodynamic cell sorting, inertial focusing, and magnetophoresis separation. RBCs, platelets, and other blood components were removed in advance. [42]

Microchip-based immunomagnetic assay provide better control of flow field and magnetic field compared with the conventional MACS. Smaller channel height of a

miniaturized microchip improves the magnetic capture. However, the miniaturization is limited by the requirements of avoiding cell clogging and maintaining laminar flow inside the channel. In addition, the channel has to be made large enough to maintain a high throughput system. To overcome the contradiction of throughput and separation efficiency, some groups came up with different approaches to increase the local magnetic field by integrating small-scale magnets inside the microchannel.

The trend from macrotubes to microchips inspired novel ideas of using in-channel structures to precisely modulate the magnetic field to facilitate cell separation. The micromagnets were engineered to generate a strong localized magnetic field. These magnetic responsive elements inside the immunomagnetic channel enhanced the near-field interactions between the cells and the magnetic field [34, 35, 80]. Incorporation of these micro magnetic flux sources provided a new way for better CTCs' separation without sacrificing the system throughput.

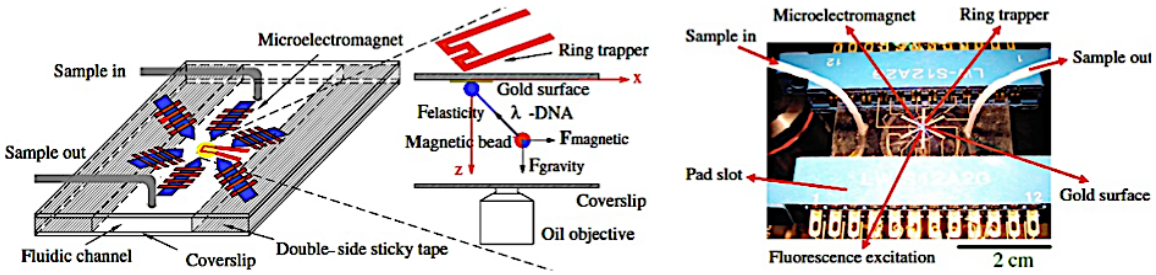

Figure 1.11: Three-dimensional image of the magnetic tweezers integrated with micro-electromagnets, a ring trapper, a microfluidic channel, and a gold-patterned surface for the manipulation of a DNA molecule. [81]

Micro-electromagnet or static micromagnets are two ways to induce the localized micromagnetic fields [82-85]. The micro-electromagnets usually involve the fabrication of three-dimensional microcoils on the planar substrate inside the microchannel, and

apply an additional current source to actuate the microcoil and generate a magnetic field, as shown in Figure 1.11 [81].

For the electromagnets, the magnetic field intensity can be easily adjusted by tuning the applied current. However, the external power source limits the portability of the system. Strength of the micro-electromagnet is also limited due to the weaker magnetic field and the issue of heat generation.

The static magnetic approach is more widely adopted, which directly patterns soft magnetic materials onto the channel substrate, using conventional photolithography and deposition techniques [82-85]. Fabricated static micromagnets can be easily magnetized by the external magnetic field to generate a locally enhanced magnetic field that is 100 times stronger than those generated by electromagnets. Therefore, static micromagnets exhibit real potential for serving as point-of-care compact systems.

Semiconductor fabrication techniques were commonly used to fabricate the micromagnets [82-88]. In addition, fabrication of shrink-induced micromagnets was proposed that nickel was deposited onto shape memory polymer films. Upon heating, the polymer film shrinked in lateral dimension, causing the nickel film to wrinkle and buckle [89]. Moreover, micromagnets were thermomagnetically patterned using heat irradiation through a mask to selectively switch the magnetization direction of a thin film micromagnet, forming an array of oppositely magnetized polarities micromagnets [90, 91]. Furthermore, ferromagnetic material used PDMS to encapsulate ferroferric oxide powder into the master template made of SU-8 photoresist. Micromagnet array was formed upon PDMS demoulding from the master template [92].

These above-mentioned micromagnets can be easily integrated in microfluidic channels for particles/particles-labeled cells sorting, focusing, and isolating application [86, 91, 93].

In addition to the fabrication methods, the reported micromagnets have been made into different structures for various purposes. For immunomagnetic cell separation,

micromagnet structures affect the intensity and distribution of the localized magnetic field, which directly determines the surface retaining force and the capture range.

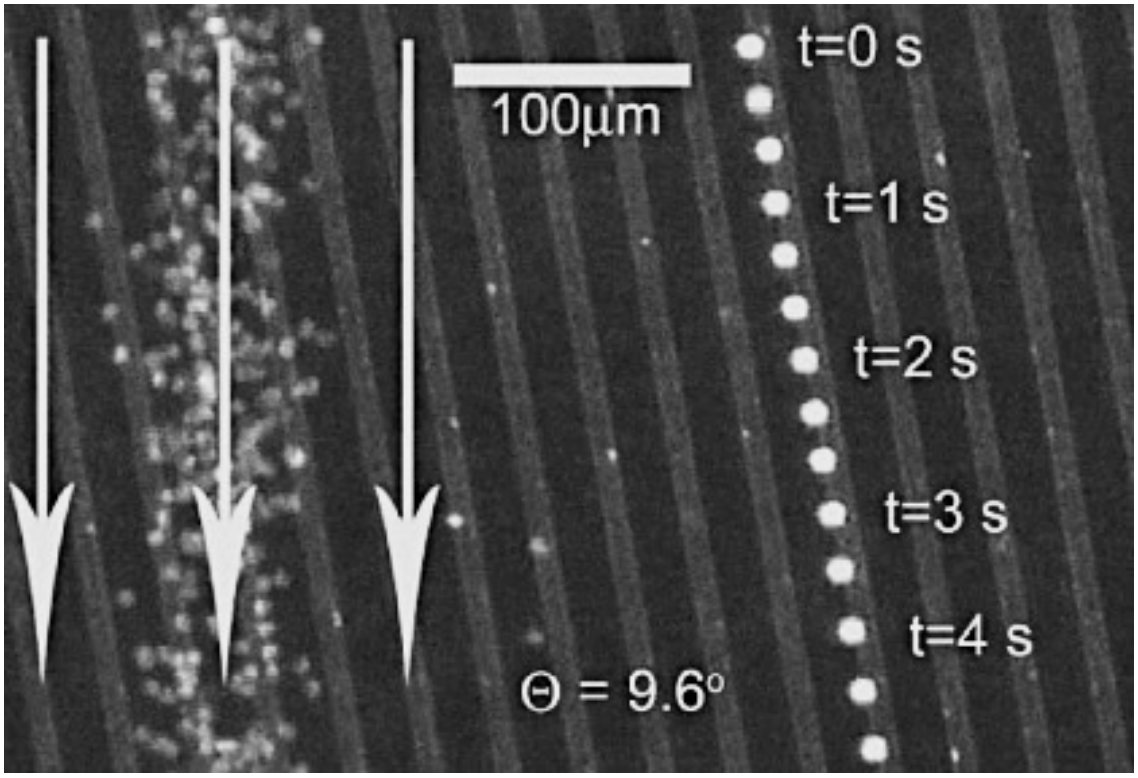

Figure 1.12: Magnetic stripe for guiding and sorting cells. [93]

The demonstrated structures include the microstripes, micropillars, microgrooves, and microchessboard. For the microstripes structure, the nickel stripe was deposited onto the substrate to alter the directions of cells with different magnetic labels. Leukocytes were successfully separated and collected in the microchannel [84, 86, 93, 94]. Figure 1.12 shows the micromagnetic stripes used to guide and sort cells. Leukocytes have been successfully isolated from whole-blood samples.

Ferromagnetic micropost structures were incorporated in the microchannel, and can be used to capture targets on the micropost surface. The system was used to separate

magnetic microbeads from nonmagnetic beads [92, 95-98]. Fabricated micropillar structures are shown in Figure 1.13.

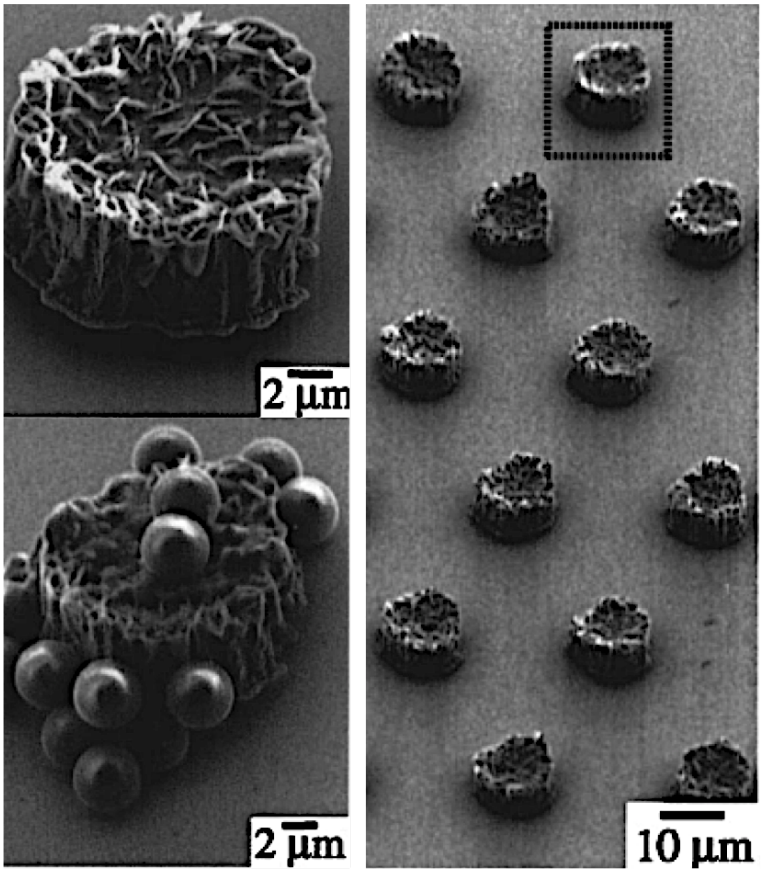

Figure 1.13: Magnetic stripe for guiding and sorting cells. [95]

The microgroove structure, as shown in Figure 1.14, was fabricated using the shrinking mechanism that targets were directly captured inside the channel in positive collection mode, or nontargets were retained in negative collection mode [89].

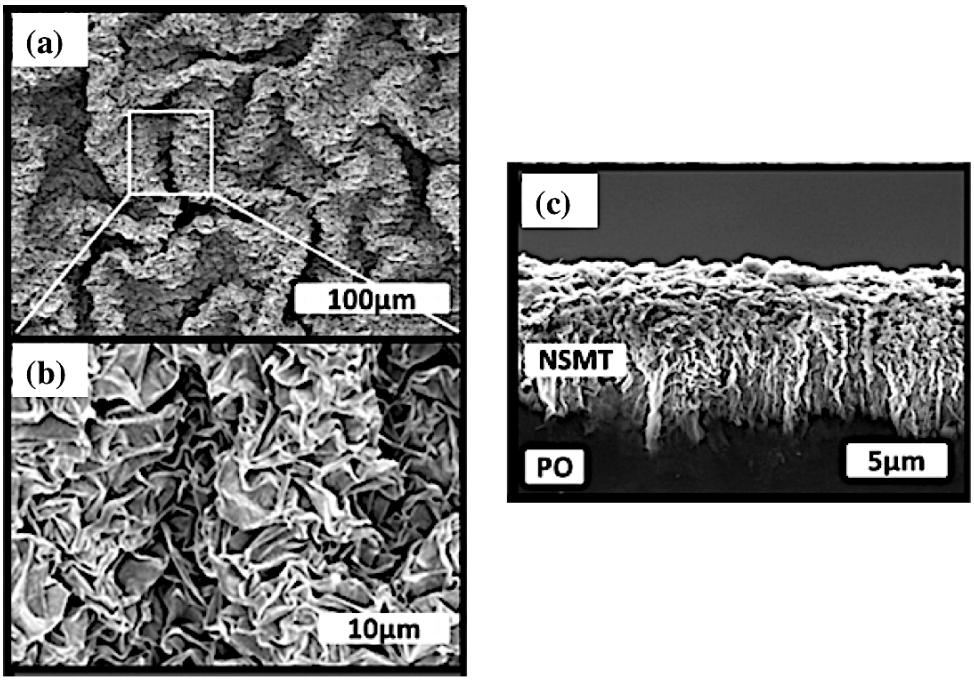

Figure 1.14: (a)(b) SEM images of shrinking structures. (c) Cross section of SEM image of structures. [89]

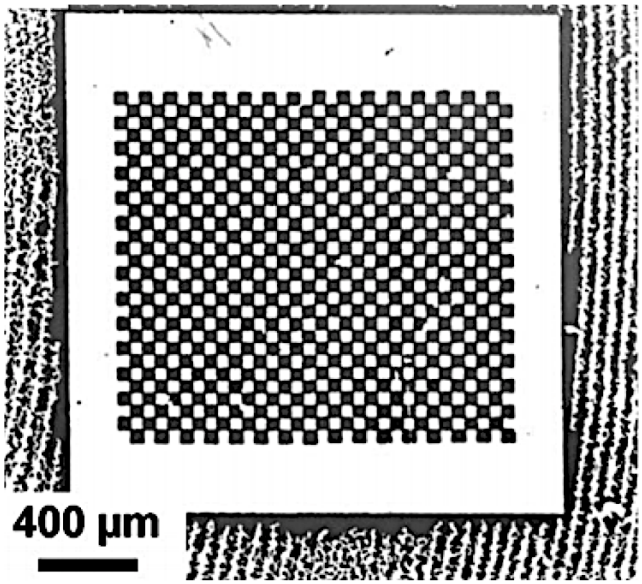

Figure 1.15: Chessboard pattern of magnetic micromagnets. [90]

For the microchessboard, the heat irradiation was used to fabricate structures; the resolution and alignment can be well controlled in an alternating pattern. Similarly, the

system has been demonstrated the capability of separating mixture of magnetic and nonmagnetic microbeads [90, 91, 99]. Figure 1.15 shows chessboard-patterned magnetized micromagnets.

Table 1.3 summarizes the fabrication principles, materials, micromagnet dimensions, capture range, and applications.

Type	Fabrication Technology	Dimensions	∇B^2 (T^2/m)	Capture region	Applications
Strips [93]	Etching Sputter coating	Width: 10 μm Thickness: 2 μm Period: 35 μm	~ 50	10 μm	Separation of leukocyte and red blood cells
Pillars [99]	Soft lithography Electrodeposition	Height: 7 μm Diameter: 15 μm	~ 500	50 μm	Microbeads filtration
Chessboard [91]	Deposition Pulse laser irradiation	Feature size: 50 μm ~100 μm, Reversal depth: 1.1 μm ±0.12 μm	~ 5	40~70 μm	Microparticles separation
Grooves [89]	Deposition Heating Shrinking	Height: 20 μm	~ 30	60~70 μm	Microbeads separation and DNA extraction

Table 1.3: Comparison of the four types of micromagnet structures [23].

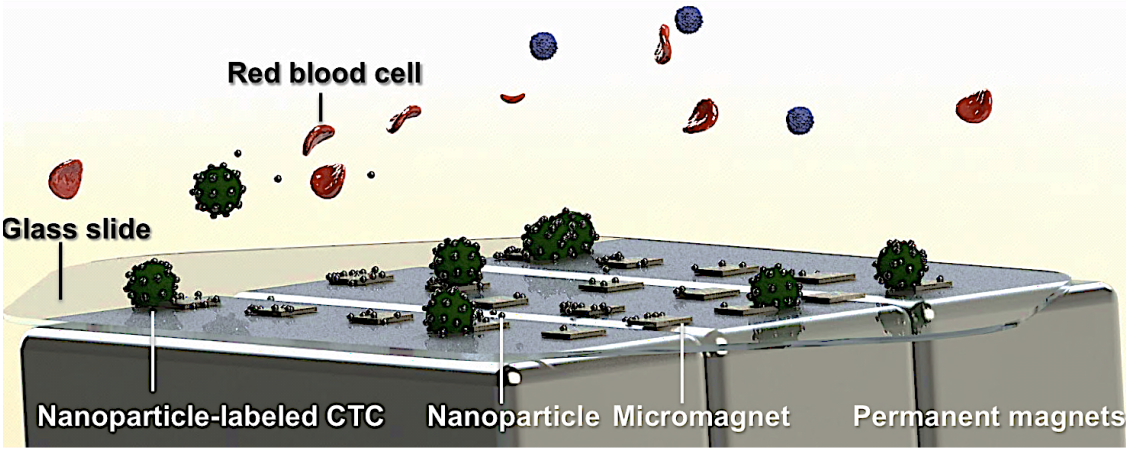

Figure 1.16: Schematic of microchip-based screening system integrated with patterned micromagnets for cell separation.

A patterned thin-film micromagnet can also be designed and applied for CTCs separation. The micromagnet, with optimized thickness at nano-scale, can generate sufficient force to magnetically attract the CTCs. The patterned array of micromagnets not only increased the capture rate but also scattered the cells to make full usage of the space inside the channel. Figure 1.16 shows the design schematic of the microchip-based screening system integrated with patterned micromagnets for cell separation.

Thin-film micromagnets integrated with the immunomagnetic CTC detection system was used to provide locally enhanced magnetic filed, minimize possible physical damage to the captured target cells, reduce the aggregation of cells or nanoparticles, provide retrievable cells after capture for further molecular studies, and offer a simple and robust fabrication process.

1.4 Downstream cellular analysis

In a conventional MACS system, like CellSearch®, fluorescent signal was the only available outcome. However, by using microchip-based immunomagnetic detection assay and integrating in-channel magnetic structures, CTCs can be precisely captured and retrieved, which enables analysis beyond the immunofluorescence. Meanwhile, as the development of single-cell profiling techniques, CTCs have made significant contributions to oncology and clinical studies, as expected. Potential downstream molecular studies for CTCs can be performed using a set of advanced tools, including polymerase chain reaction (PCR), reverse transcription polymerase chain reaction (RT-PCR), quantitative reverse transcription polymerase chain reaction (qRT-PCR), digital PCR, and fluorescence *in-situ* hybridization (FISH) on selected cells [30, 31, 42, 100, 101]. On one hand, findings like correlation between primary tumors and corresponding CTCs [102] or heterogeneity of different cancer cell lines [45, 103] may have clinical implications for discoveries of new drugs and targeted therapeutic strategies in patients.

On the other hand, breakthroughs regarding the gene expression of CTCs [57], and epithelial-mesenchymal transition (EMT) could help gain insights into metastasis [56].

FISH has been considered as a rapid, reproducible, reliable, and powerful tool for probing the genetic information of cancer cells at the chromosomal scale [104, 105].

HER-2 (human epidermal growth factor receptor 2), also known as HER-2/*neu* or c-*erb*B-2, is a member of the epidermal growth factor receptor (EGFR/*erb*B) family [105]. HER-2 is located at 17q12 and encodes a 185 kDa transmembrane, receptor-like intrinsic tyrosine kinase activity [106]. Amplification or over-expression of HER-2 proto-oncogene has been shown to be an indicator in the development and progression of breast cancer. Amplification and overexpression of HER-2 account for approximately 20–30% of breast carcinomas. Measured copies of HER-2 have been associated with a shorter survival and an increased risk of recurrence of cancer. FISH has been commonly used to measure the copy number of HER-2 and chromosome *in situ* [65, 107-116].

Here we use the FISH method to study the genomic information, such as HER-2^{+} and HER-2^{-} of spiked cancer cells and CTCs from patient samples captured by the developed screening system.

1.5 Dissertation organization and Major contribution

The major contributions of the project have been listed as follows. 1) Design and fabricate an automated micromagnet-integrated microfluidic screening system for detection of rare cells, known as circulating tumor cells (CTCs). 2) The theoretical and experimental characterizations of the developed screening system have been performed. In addition, high capture efficiency, high throughput, and accurate enumeration have been demonstrated by performing spiked screening experiments. 3) The developed system has been successfully applied for clinical screening of patient samples. The screening system is capable of achieving high sensitivity and specificity for clinical

application. 4) Downstream analysis for the molecular characterization of isolated cancer cells (CTCs) has been performed.

This dissertation is arranged as follows. “Chapter 1: Introduction” reviews the background and significance of metastasis and CTCs, as well as currently existing rare cell detection and separation technologies. In addition, present downstream analysis methods for cancer cells are discussed.

In Chapter 2, the principle of the operation of the system is introduced. Besides, it explores the basic theory of hydrodynamics and magnetophoresis for the design of microchannel and magnetic force determination. We also discuss the biological interaction between the magnetic carrier and the target cancer cell.

Chapter 3 describes the experimental results for the development and fabrication of the screening system, including the microfluidic device, computer-controlled rotational system, rocking system, patterning of array of micromagnets, sample preparation, screening step, separation process, staining step, and identification of captured CTCs. In addition, we also discuss the screening results of magnetic field measurement of different magnets, immunofluorescent staining of cells, and downstream analysis.

Chapter 4 discusses the calibration of the proposed system by performing spiked screening experiments and the clinical application for patient samples. Results of the downstream analysis are also included.

In Chapter 5, conclusions are made for the proposed screening system, and future work is discussed for possible directions for the project.

Chapter 2

Theory and Methods

In order to optimize the detection system, we present the theoretical study of the key parameters for the screening system.

We first describe the operation principle of cell separation. The principle of magnetic carrier tagging of the target cancer cells, surface biomarkers on the cancer cells, hydrodynamic flow, and magnetic field distribution in the microchannel regarding the scaling law for immunomagnetic separation are discussed. We then analyze the device functionality based on the key parameters, which are critical to the capture efficiency of the separation method.

2.1 PRINCIPLE OF OPERATION

For the immunomagnetic assay, magnetic carrier is used to tag the target cell, as shown in Figure 2.1 [41, 117]. The magnetic carriers are usually conjugated with monoclonal antibodies (e.g. EpCAM) specific to biomarkers (antigens) expressed on the cell surface. The magnetic carrier-tagged cell is magnetically attracted to the channel substrate by the magnet.

The magnetic carrier, such as iron oxide (Fe_3O_4), can be coated with a polymer, including dextran, albumin, or polyethylene. The polymer coat on the magnetic core can be a variety of functional groups, such as amino, aldehyde, hydroxyl, sulfate, and carboxyl groups [118]. In addition, a uniform gold layer, which is gold shell, is commonly used to coat the magnetic carrier surface. Plasmonic gold-coated iron-oxide particles provide novel imaging approaches and photothermal/hyperthermia therapy of cancer [41, 119-121].

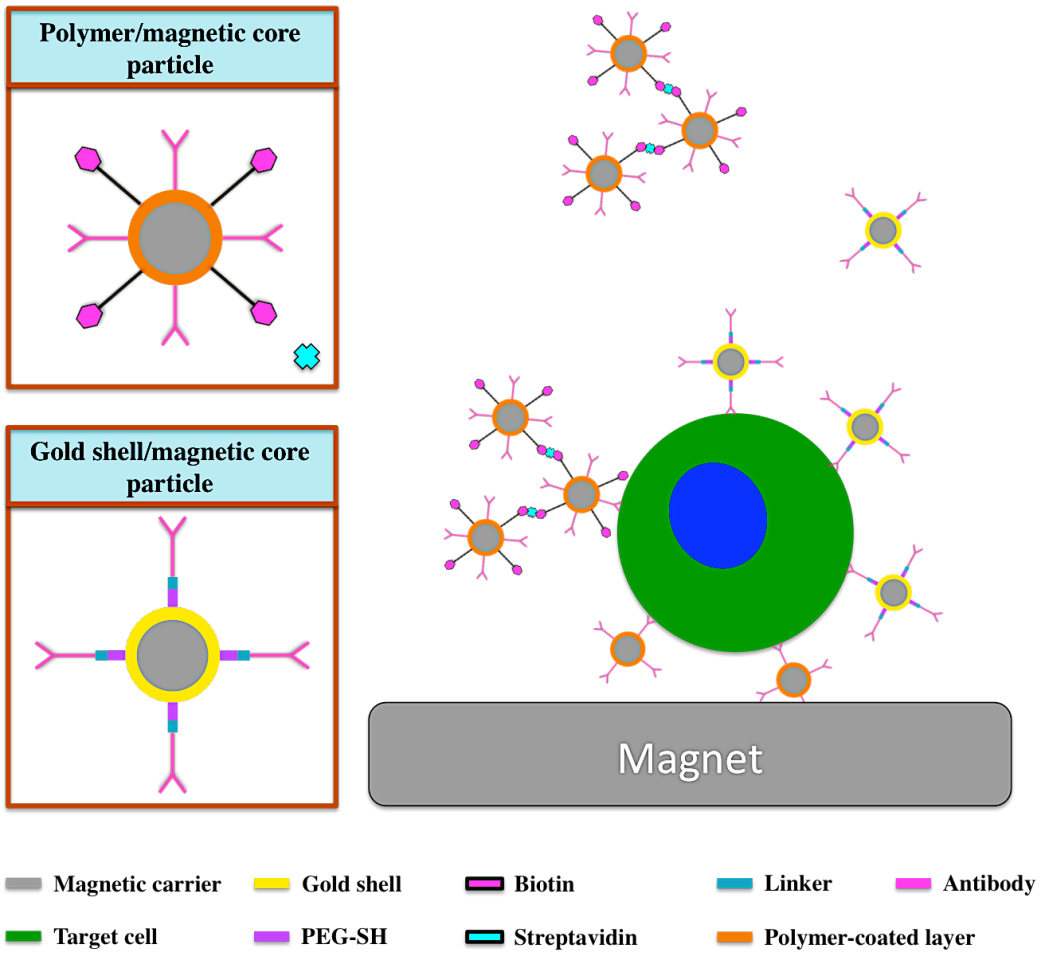

Figure 2.1: Schematic of polymer-coated magnetic core particle or gold shell/magnetic ore particle used for tagging. [41]

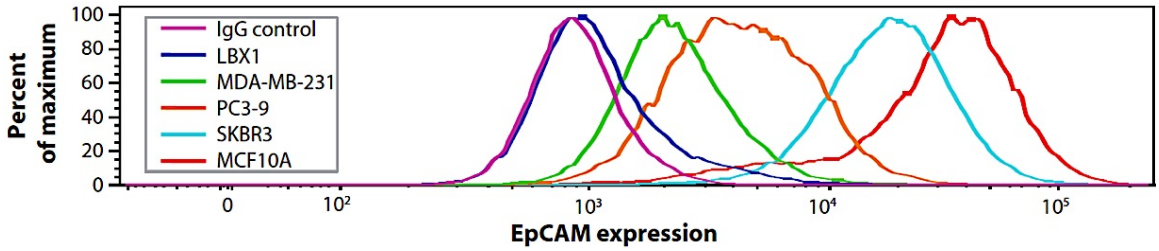

Figure 2.2: Comparison of EpCAM expression level in five different cell lines. [42]

The epithelial adhesion molecule (EpCAM) is usually overexpressed in primary and metastatic carcinomas. The number of magnetic carriers attached to the cancer cell is

strongly associated with the EpCAM expression level. Figure 2.2 shows the expression level of EpCAM in five different cell lines, including LBX1, MDA-MB-231, PC3-9, SK-BR-3, and MCF10A cell lines. Here we focus on only three cell lines—MDA-MB-231 (breast cell line), PC3-9 (prostate cell line), and SK-BR-3 (breast cell line), and MCF10A (breast cell line). MCF10A has the highest EpCAM expression level compared to the EpCAM expression level of another four cell lines.

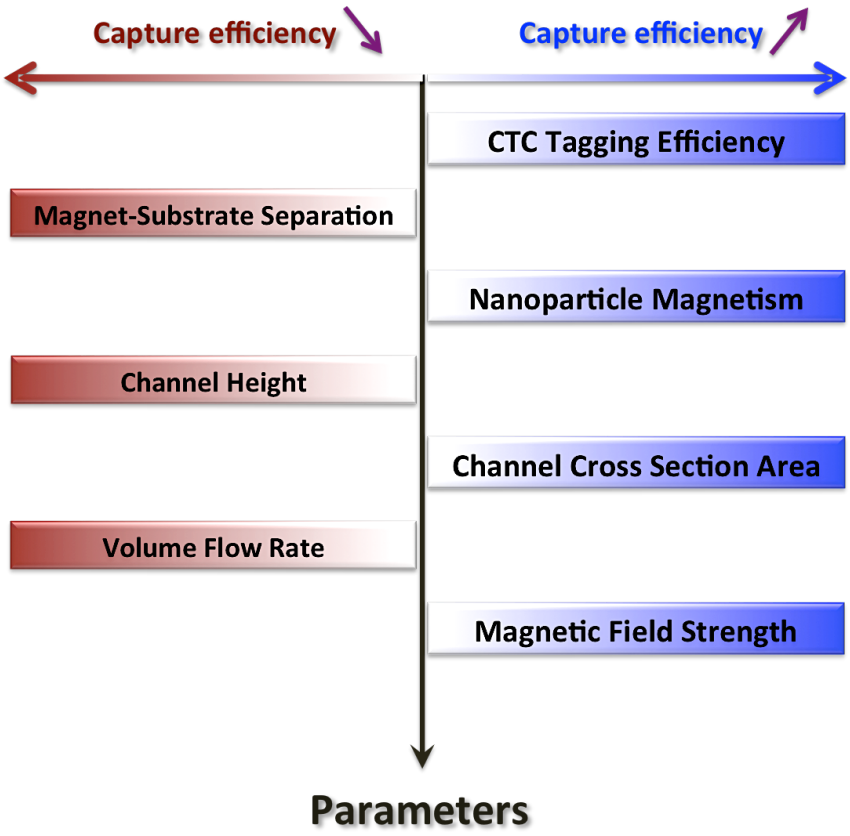

Figure 2.3: Multiple parameters affect capture efficiency.

Figure 2.3 shows some key parameters that significantly affect the capture efficiency of the cell separation system. Efficiency variation is related proportionally to those parameters marked in blue and inversely with those in red. Those parameters are

discussed and optimized to achieve high capture efficiency of the developed screening system.

To address how the physical principles of immunomagnetic assay evolve over the length-scale and to assist in future design, the scaling laws of the immunomagnetic assay are discussed. Figure 2.4 illustrates the physical model in which magnetic force (F_{mag}), hydrodynamic drag force (F_{drag}), gravitational force (F_g), and buoyancy force (F_{buo}) dominantly affect the motion of target cells, which are tagged with magnetic nanoparticles, in a flow environment under an external magnetic field.

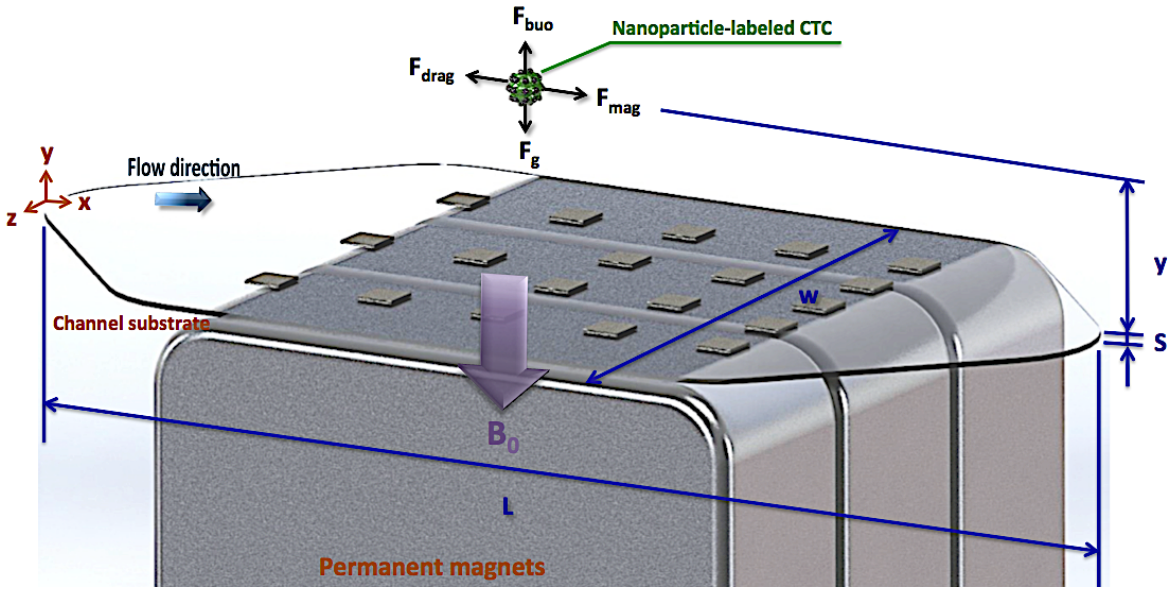

Figure 2.4: Physical model of nanoparticles-labeled cell in microchannel.

A simplified model of the microchannel is defined under the assumptions below [34]:

- The distribution of the magnetic field is uniform in the *x* direction;
- The flow field is laminar and uniform in *x*–*z* plane;

- The velocity profile in y direction is a parabolic profile defined by the flow rate Q.

Based on the property of the nanoparticles and the labeling efficiency, the magnetic force, which is in the order of 10^{-10} N, is about 100 times larger than the gravitational force, which is in the order of 10^{-12} N, on the CTCs [76, 122]. In addition, F_{mag} and F_{drag} are two dominant forces acting on a nanoparticle in the microchannel. We therefore simplify the calculation so that only F_{mag} and F_{drag} are considered.

In the capture region of the microchannel, hydrodynamic drag force (F_{drag}) is strongly correlated to the flow field so that F_{drag} is determined by the flow rate (Q) and channel dimensions, including length (L), width (W), and height (H). Magnetic force (F_{mag}) is dependent on the applied magnetic field generated by the magnetic flux (B_0) of the permanent magnets, thickness (S) of the channel substrate, magnetic susceptibility ($\Delta\chi_p$) of the magnetic tags (magnetic particles), and labeling efficiency of magnetic tags labeled on the cell so that the number of particles tagged on each target cell is represented as N.

If the dimensions of the permanent magnets are significantly larger than the capture region of the microchannel in the y direction, the magnetic field within the capture region can be represented as

$$B(y) \propto \frac{B_0}{(S+y)^2} \ , (0 < y < H) \tag{2.1}$$

The average time (τ) that a cell travels in the microchannel can be estimated using the dimensions of the capture region and flow rate. The average time (τ) is as follows:

$$\tau = \frac{W \cdot H \cdot L}{Q} \tag{2.2}$$

The magnetic force acting on a particle (F_{mag}) is dependent on the magnetic dipole (m) of the nanoparticle and the magnetic field B, given by the equation below [82]:

$$F_{mag} = (m \cdot \nabla)B \tag{2.3}$$

The total magnetic moment of a nanoparticle can be expressed using:

$$m = \frac{V_p \Delta\chi_p}{\mu_0} B \tag{2.4}$$

V_p is the volume of a single nanoparticle. μ_0 is the magnetic permeability of vacuum ($\mu_0 = 4\pi \times 10^{-7}\ T \cdot m \cdot A^{-1}$). To simplify the calculation, $\nabla \times B$ is assumed to be zero ($\nabla \times B = 0$). The magnetic force (F_{mag}) acting on a magnetic particle is simplified to the following equation:

$$F_p = \frac{V_p \Delta\chi_p}{2\mu_0} \nabla B^2 \tag{2.5}$$

where $\Delta\chi_p$ is the volumetric magnetic susceptibility of the particle. V_p is the velocity of the nanoparticle.

Eventually, the magnetic force acting on a cell labeled with N nanoparticles (F_c) is the summation of the all forces from all the nanoparticles tagged on the cell.

$$F_c = N \times F_p \tag{2.6}$$

where N is the total number of magnetic nanoparticles attached to the cell.

When the cells move along the laminar flow within the capture region of the microchannel driven by the magnetic force, we assume a quasi-static motion that Stokes'

drag force equals to the magnetic force in the capture region. The equation below shows the Stokes' drag force.

$$\mathrm{F_{drag}} = 6\pi\eta R\Delta v \tag{2.7}$$

The Stokes' drag force generated against the magnetic force determines the instant relative velocity of the cell. Therefore, the instant relative velocity of the cell can be calculated as follows:

$$\Delta \mathrm{v} = \frac{\mathrm{R_c^2}\Delta\chi_c}{9\mu_0\eta}\nabla B^2 \tag{2.8}$$

where $\mathrm{R_c}$ is the radius of the cell and η is the viscosity of the medium. $\Delta\chi_\mathrm{c}$ is the effective magnetic susceptibility of the cells that $\Delta\chi_\mathrm{c}$ is represented as:

$$\Delta\chi_\mathrm{c} = N\frac{R_p^3}{R_c^3}\Delta\chi_p \tag{2.9}$$

Therefore, the average velocity of cells inside the microchannel can be calculated by averaging across the channel height.

$$V_{ave} = \frac{1}{H}\frac{R_c^2\Delta\chi_c}{9\mu_0\eta}\int_0^H \nabla \mathrm{B(x)}^2 dx \tag{2.10}$$

To determine the required magnetic field strong enough for a successful capture, we equate the vertical distance that the cells move in the *y*-direction to the height of the microchannel ($v_{ave}\cdot\tau = H$), yielding

$$B_0 = \frac{9\mu_0\eta}{R_c^2\Delta\chi_c} \times \frac{H \cdot FR}{W \cdot L} \times \frac{1}{(S+H)^{-4} - S^{-4}} \tag{2.11}$$

2.2 MODELING AND SIMULATION

We build a computer-based analytical program to assess the device functionality. The developed program traces the trajectory of particles in the microchannel. In addition, the capture rate for suspended particles can be estimated by computing calculations for particles uniformly entering the microchannel.

2.2.1 Flow field in the microchannel

Reynolds number (Re), which is the ratio of inertial force to viscous force, is usually used to characterize the fluid flowing in a microfluidic channel, defined as [123]

$$Re = \frac{\rho V_{ave} L}{\eta} \tag{2.12}$$

where ϱ is the fluid density, V_{ave} is average velocity of the flow, L is the characteristic length, and η is the viscosity.

In the microfluidic channel, it is defined that Re<400 for laminar flow, 400<Re<1000 for the transition region, and Re>1000 for turbulent flow [124].

The parameters, such as flow rate (Q) and channel height (h), need to be optimized to minimize shear stress on the cell fixed on the channel substrate for the laminar flow in the microchannel. Figure 2.5(a) shows the parabolic flow in the channel. Figure 2.5 (b) shows the difference in the shear stress acting on the cell captured on the channel substrate between two different channel heights under the same flow rate.

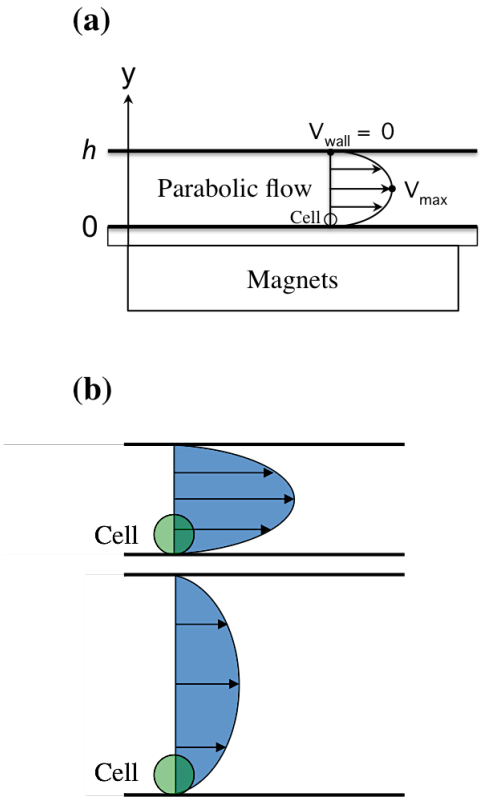

Figure 2.5: (a) Schematic of the cross-section of the channel showing the parabolic flow. (b) Different shear forces acting on a cell captured on the channel substrate with different channel heights under the same flow rate.

The relationship between the channel height (h), the flow velocity (V), and flow rate (Q) is represented as below:

$$V(y) = -\frac{4V_{max}}{h^2} \times y(y-h) \tag{2.13}$$

$$Q = \int_0^h V(y)\,dy = \frac{2}{3}\,hV_{max} \tag{2.14}$$

Therefore, the shear force acting on the cell bound on the channel bottom can be indicated in the following equation.

$$F = \iint_0^{Cell\ diameter} \tau \left.\frac{dV}{dy}\right|_{y=h} dh$$
$$= -\tau \left.\frac{4V_{max}(2y-h)}{h^2}\right|_{y=h} = -\frac{8V_{max}}{h} = -\frac{12Q}{h^2} \qquad (2.15)$$

Based on the equation (2.15), the required magnetic field intensity can be minimized by decreasing the channel height (H) and increasing the cross-section area ($W \times L$) of the microchannel. The scaling laws justify the developed miniaturized microchannel for cell separation.

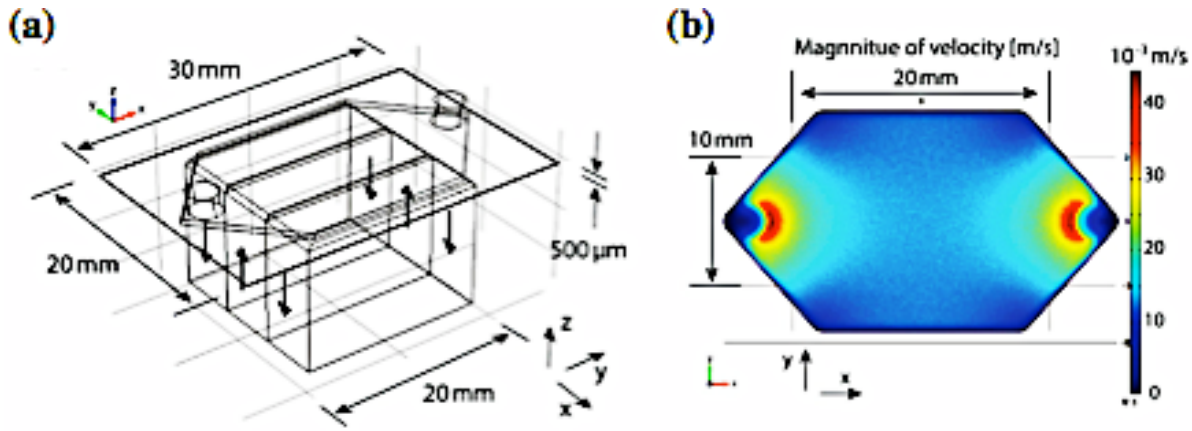

Figure 2.6: Configuration of the microfluidic immunomagnetic separation device [80]. (a) Three-dimensional model created for finite element analysis software COMSOL. (b) Flow velocity magnitude (mm/s) calculated with the sample flow rate (Q) of 10 mL/hr. [80]

A schematic photograph of the microfluidic device for the immunomagnetic assay-based cell separation is shown in Figure 2.6(a). Channel dimensions are indicated for finite element analysis software COMSOL. Figure 2.6(b) is the flow velocity magnitude calculated with the sample flow rate of 10 mL/hour.

The average velocity flow velocities is given as

$$v_{ave} = \frac{Q}{(\frac{w}{h})} = 0.33\times10^{-3}\ (m/s) \tag{2.16}$$

The velocity is within the typical values of those found in previous studies of microchip-based separators demonstrating that the velocities are in the order of from 10^{-6} to 10^{-3} m/s [34, 44, 76, 80, 125-128].

2.2.2 Magnetic field in the microchannel

Figure 2.7 shows a simulated distribution of magnetic flux density made by an array of three magnets.

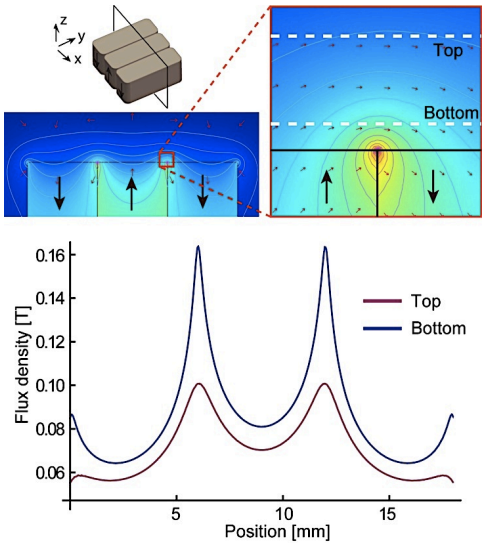

Figure 2.7: Simulated magnetic flux density. The contour plot is for the magnetic potentials. Magnetic flux densities at the top and bottom of the microchannel are plotted. A large magnetic field gradient is induced by the alternating arrangement of the three magnets. [34]

For efficient attraction of magnetic nanoparticles, which essentially act as small dipoles, magnetic field gradient rather than absolute field strength is required. A strong but uniform magnetic field rotates the dipole orientation but does not attract it. Alternately arranged magnets with opposite polarities next to each other make a large gradient. We used three NdFeB block magnets with a maximum energy product of 42 MGOe (grade 45 N42).

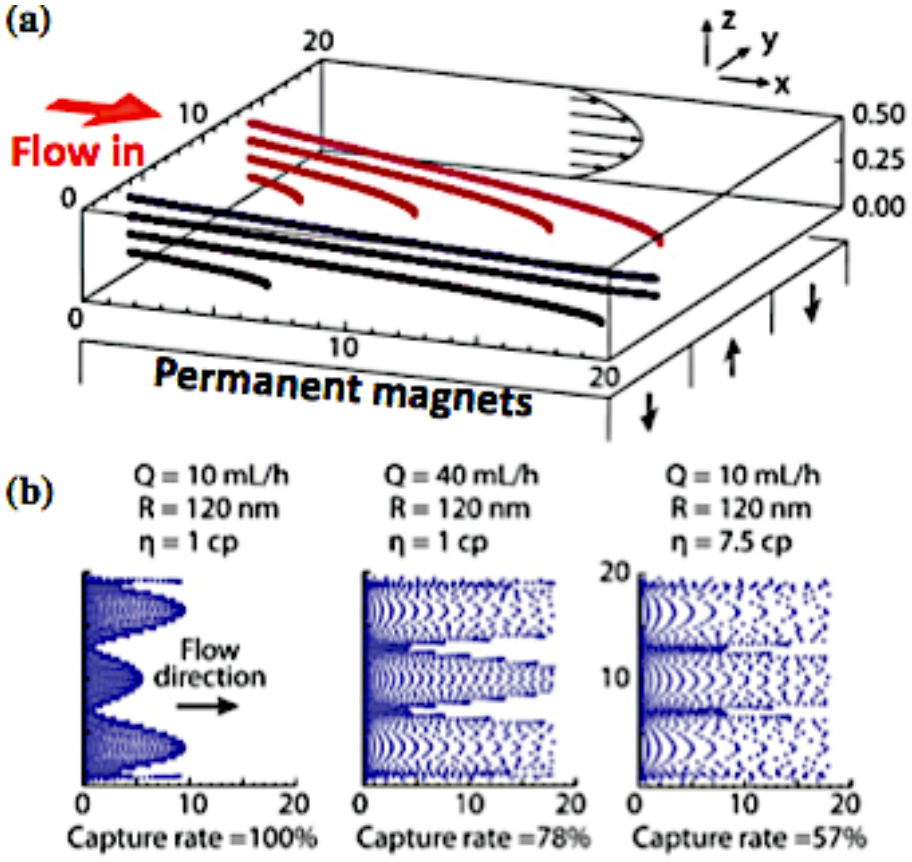

Figure 2.8: Computer-based analysis of the device functionality. (a) Particle trajectories in the microchannel. Q = 10 mL/hour, R_p= 50 nm, and η = 1 cp. (b) Ferrofluids captured on the glass slides. First two pictures are for buffer solution (η = 1 cp); the third picture is for blood (η = 7.5 cp). [34]

A gauss meter was first used to measure the magnetic field induced by one magnet, and the obtained intensity value was used to further calculate the result with three magnets. The microchannel is located on top of the array. The flux densities at the bottom (150 μm from the magnet) and the top (650 μm from the magnet) of the channel are also shown in Figure 2.8. A strong gradient is created to attract nanoparticles between adjacent magnets.

Figure 2.8(a) shows an example of trajectories of particles with two different initial positions (indicated in black and red) in the microchannel. Some particles are trapped by the externally applied magnetic force so that other un-trapped nanoparticles escape from the microchannel. Particle distributions for two different flow rates (10 mL/h versus 40 mL/h) are shown in the first two pictures of Figure 2.8(b). The third picture of Figure 2.8(b) shows the result with the medium of blood sample. Here the blood viscosity is set to be $\eta_B = 7.5\times10^{-3}\ kg \cdot m^{-1} \cdot s^{-1}$.

Here we use an array of permanent magnets (three NdFeB block magnets, product of 42 MGOe, grade N42, 3/4″ × 1/2″ × 7/32″, magnetized through 3/4″) with opposite polarities next to each other. Three magnetic-filed arrangements have been performed. 1) A stack of three parallel permanent magnets is placed on a 150 μm thick glass coverslip [Figure 2.9(a)(c)]. 2) A stack of three parallel permanent magnets is placed on a 150 μm thick glass coverslip with a 1 mm spacer gap (elastic sheet magnet, which is sized at 10 mm ×20 mm ×1 mm) introduced at the front end of the microchannel between the magnets and the microchannel, as shown in Figure 2.9(b)(d). The space gap is used to create a magnetic field gradient, increasing throughout the whole microchannel. 3) A 1 mm thickness glass slide is in the inverted microchip.

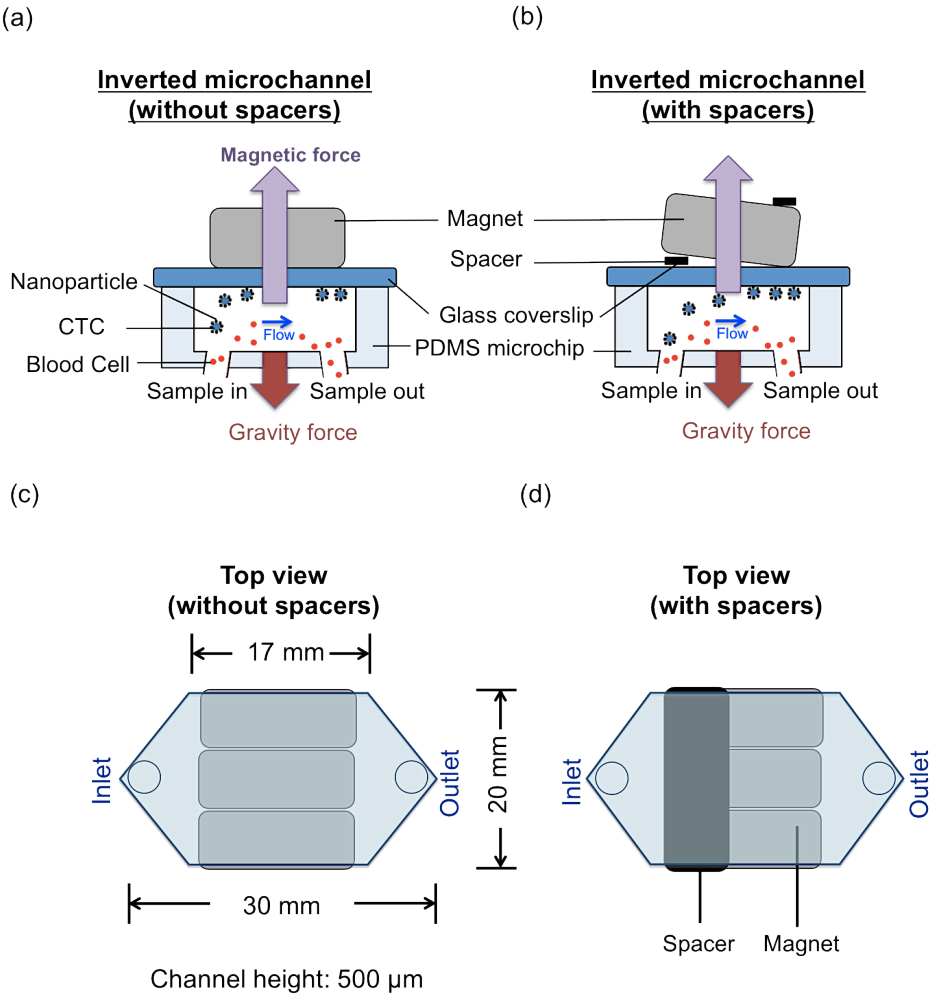

Figure 2.9: Schematics of magnetic field arrangements. (a) Inverted microchip with no spacers placed between magnets and glass coverslip. (b) A spacer is placed close to the front end of the microchannel between magnets and glass coverslip. (c) Top view of a microchannel and permanent magnets. (d) Top view of a microchannel and permanent magnets together with a spacer. [35]

We measured the magnetic field of one magnet by using a gauss meter. After acquiring the measured data, we used the measured values to define parameters in the simulation and calculated the result of three magnets with opposite polarities arranged next to each other. We used COMSOL for the magnetic field simulation. Figure 2.10(a) plots the magnetic field flux density distribution for a plane 200 µm away from the bottom substrate of the microchannel calculated using commercial finite element method

(FEM) software COMSOL. In order to demonstrate our idea of smoothing the magnetic field gradient by adding spacers, we compared the magnetic flux densities at three different sites [Lines 1, 2, and 3 in the inset of Figure 2.10(b)] over the channel.

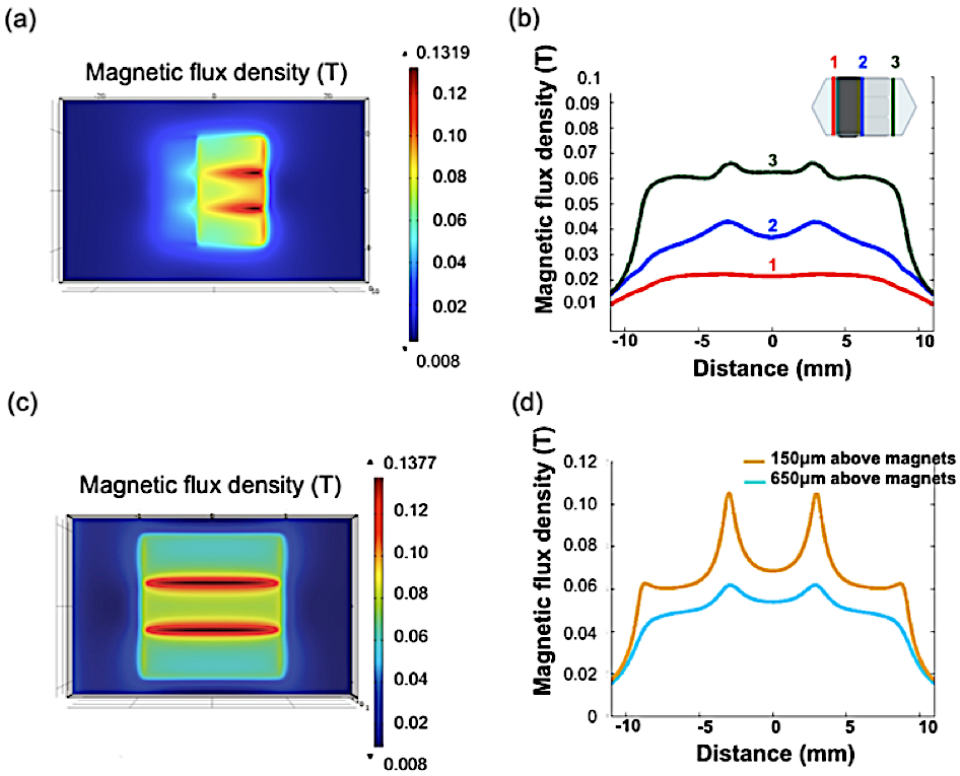

Figure 2.10: Magnetic field distribution in the microchannel, calculated using COMSOL. (a) Magnetic field distribution of three parallel magnets with a spacer. (b) Magnetic flux densities at different locations across the channel (line 1, 2, and 3) at the height of 200 μm in the microchannel. (c) Magnetic field distribution of permanent magnets without any spacers. (d) Plots of magnetic flux densities at the top and the bottom of the microchannel. [35]

A schematic of three magnets and a coverslip along with a spacer is shown in Figure 2.11(a). Magnetic flux densities at different locations over the microchannel from the inlet to the outlet (X_3, X_2, X_1, and X_0) are compared. Magnetic flux densities are simulated 200 μm above the channel substrate. Results are plotted in Figure 2.11(b).

Magnetic forces along lines X_3 and X_2 are large enough to attract most target cells and nanoparticles. Magnetic flux density distribution for a plane 200 μm away from the channel substrate is plotted in the red dashed line. Therefore, the glass slide does not significantly reduce the magnetic force acting on the magnetic nanoparticles.

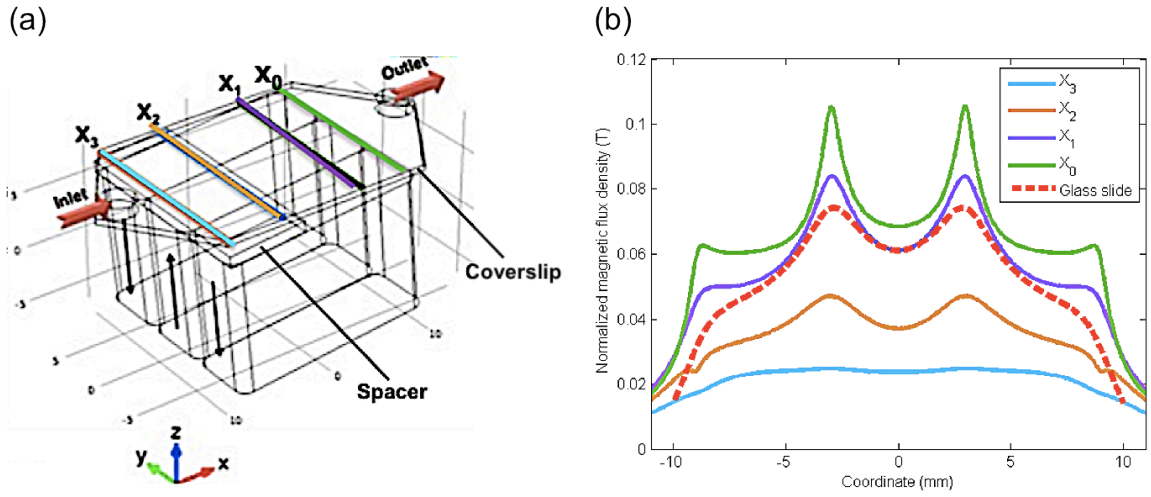

Figure 2.11: (a) Schematic of a coverslip placed over three parallel magnets along with a spacer close to the front end of the microchannel. Lines X_3, X_2, X_1, and X_0 indicate the locations for magnetic flux density simulation. (b) Plotted simulated magnetic flux densities of line X_3 (blue), X_2 (yellow), X_1 (purple), and X_0 (green). Magnetic flux density distribution 200 μm above the glass slide substrate is plotted in the red dashed line.

The downscaling modifications of microchannel dimensions are limited by the requirements of maintaining laminar flow through the microchannel, and the need to avoid clogging of the microchannel. Therefore, the integration of micromagnets is used to enhance the localized magnetic force.

In terms of modulating the magnetic field, especially designing the micromagnet patterns and integrating them with a screening system for rare cell isolation, there are several governing design parameters that need to be addressed, such as lateral dimension

of a single micromagnet element, thickness of a single micromagnet element, and spatial periodicity of the micromagnet array, as illustrated in Figure 2.12.

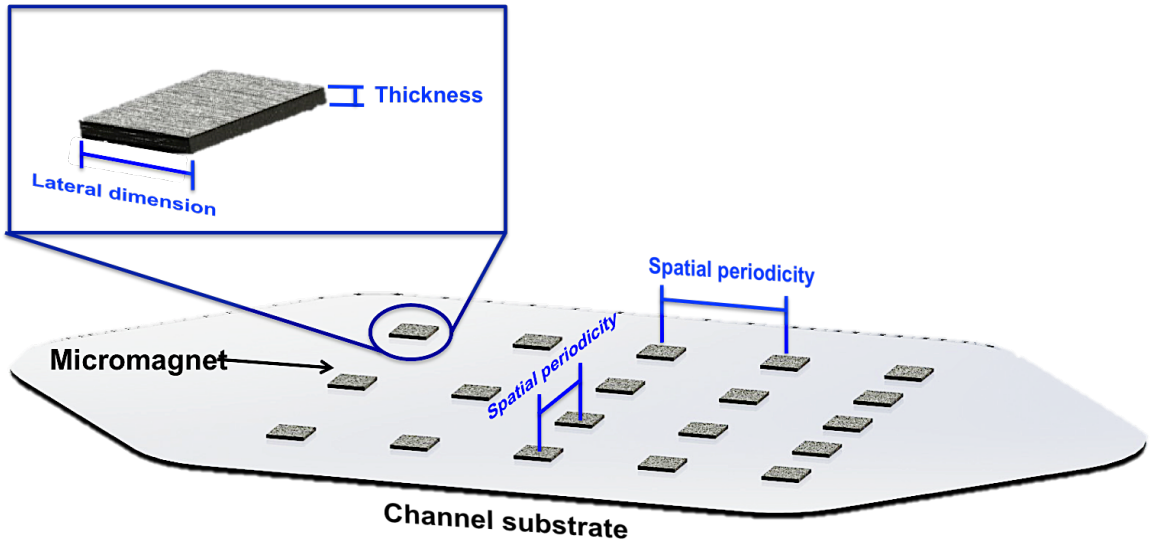

Figure 2.12: Schematic of an array of the patterned micromagnets. Key parameters, including the lateral dimension, spatial periodicity, and thickness of the thin film micromagnets are depicted.

Lateral dimension refers to the length and width of a single micromagnet element, which determine the lateral interaction distance of the micromagnets. Larger lateral size of the micromagnets leads to the broader affected area. Micro-scale patterning can be easily fabricated using conventional photolithography techniques.

Thickness of a micromagnet indicates the distance of the depositing layer extruded from the microchannel substrate. Thickness affects the system performance hydrodynamically and magnetically in the microchannel. Thick micromagnets can disturb the laminar flow in the microchannel, creating turbulent flows as a microscale mixer [31, 129]. However, thick micromagnets (three-dimensional microstructure, such as micropost or pillar structure) also generate issues such as a higher possibility of physically

damaging the cells by the flowing hydrodynamic force and creating more imaging focal planes, making the identification process more difficult and time consuming. Therefore, thickness determines the magnitude of the magnetic force and the vertical interaction distances of the micromagnets. Thicker micromagnets produce stronger magnetic forces and attract target cells farther away from the channel substrate. Depending on different intended applications, the proper thickness of the micromagnet needs to be optimized to balance these factors. In the CTC detection system, permanent magnets provided the attractive forces for capture, and the micromagnets were designed to retain the cells in the near-surface region.

Spatial periodicity is used to describe the distance between adjacent micromagnet elements in the array. It can be engineered to adjust the distribution of the captured CTCs on the channel substrate. The interaction distance of each micromagnet element—that is, the lateral dimension of the micromagnets, mainly decides appropriate spatial periodicity.

Free nanoparticles magnetically aggregate around micromagnets following the directions of the external magnetic field and the flow field, which work equivalently as enlarged micromagnets with different sizes and properties. The CTCs were trapped by the nanoparticles aggregated around the micromagnets in most cases.

Micromagnets patterned on the microchannel substrate can provide a locally enhanced magnetic field in the channel. A ferromagnetic material (nickel) is deposited on the channel substrate to introduce localized magnetic forces to magnetically attract magnetic particle-tagged cells. Figure 2.13(a) shows the schematic of localized magnetic forces induced by the permanent magnet, which is alternately arranged, and micromagnets. Figure 2.13(b) shows that higher magnetic field gradients occur at the edges of the micromagnets. The magnetic flux density passing through the micromagnet in the x-direction is greatest when the micromagnet's width (W) is larger than its height (h) of the micromagnet.

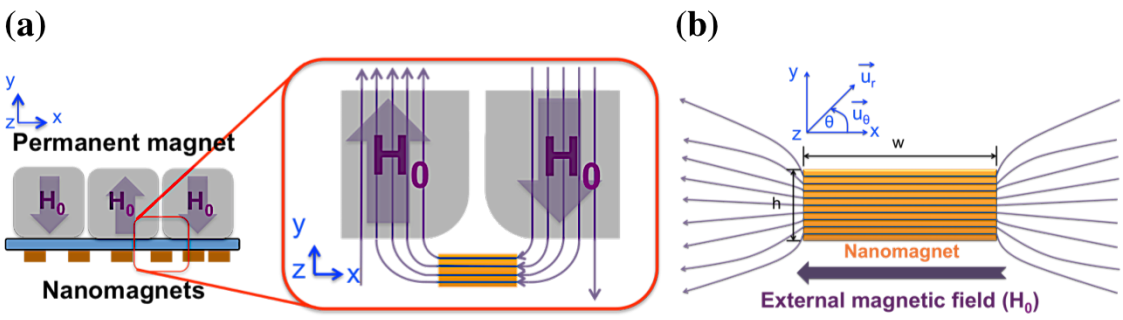

Figure 2.13: Schematic of micromagnets patterned on the microchannel substrate. (a) Locally enhanced magnetic field generated by the micromagnet, which is magnetized by permanent magnets placed on top of the capture substrate. (b) Magnetic flux density travels through a micromagnet located between two permanent magnets in the *x*-direction. A uniform external magnetic flux density (H_0) deforms around the micromagnet and generates a high magnetic field gradient. [130]

The magnetic force generated by a micromagnet acting on a nanoparticle can be calculated as [131]

$$\overrightarrow{F_p} = -\frac{2k\Delta x V_p a^2}{\mu_0 r^3}\left[k\left(\frac{w}{h}\right)\frac{a^2}{r^2} + \cos 2\theta\right] B_i\, H_0 \overrightarrow{u_r} - \frac{2k\Delta x V_p a^2}{\mu_0 r^3}(\sin 2\theta) B_i\, H_0 \overrightarrow{u_\varphi}, r > a \quad (2.17)$$

where $B_i = 2\left(\frac{w}{h}\right) H_0$, $k = \frac{\mu_m - \mu_B}{\mu_m + \mu_B}$, $\Delta x = x_p - x_B$

B_i is the inner magnetic flux density of the micromagnet
χ_{NP} and χ_B are the susceptibilities of the nanoparticle and the buffer solution
μ_{NP} and μ_B are the permeability of the nanoparticle and the buffer solution
V_{NP} is the volume of the nanoparticle
a is the lateral dimension of the micromagnet
r and θ are the cylindrical coordinates of the distance and angle
H_0 is the external magnetic field
$\vec{u}_r$ and $\vec{u}_\theta$ are unit vectors for the distance and angle in the cylindrical coordinate

In the developed immunomagnetic screening system, the micromagnets are made

of nickel and chromium, with dimensions of 20 μm (width), 250 nm (thickness), and saturation magnetization $\overrightarrow{M_{es}} = 7\times10^{-6} A \cdot m^{-1}$. We first calculated the magnetic field generated by a single micromagnet, and plotted the distribution of both *X* and *Y* components along horizontal lines, with three different heights (*h* = 5 μm, 15 μm, and 30 μm) on top of the micromagnet.

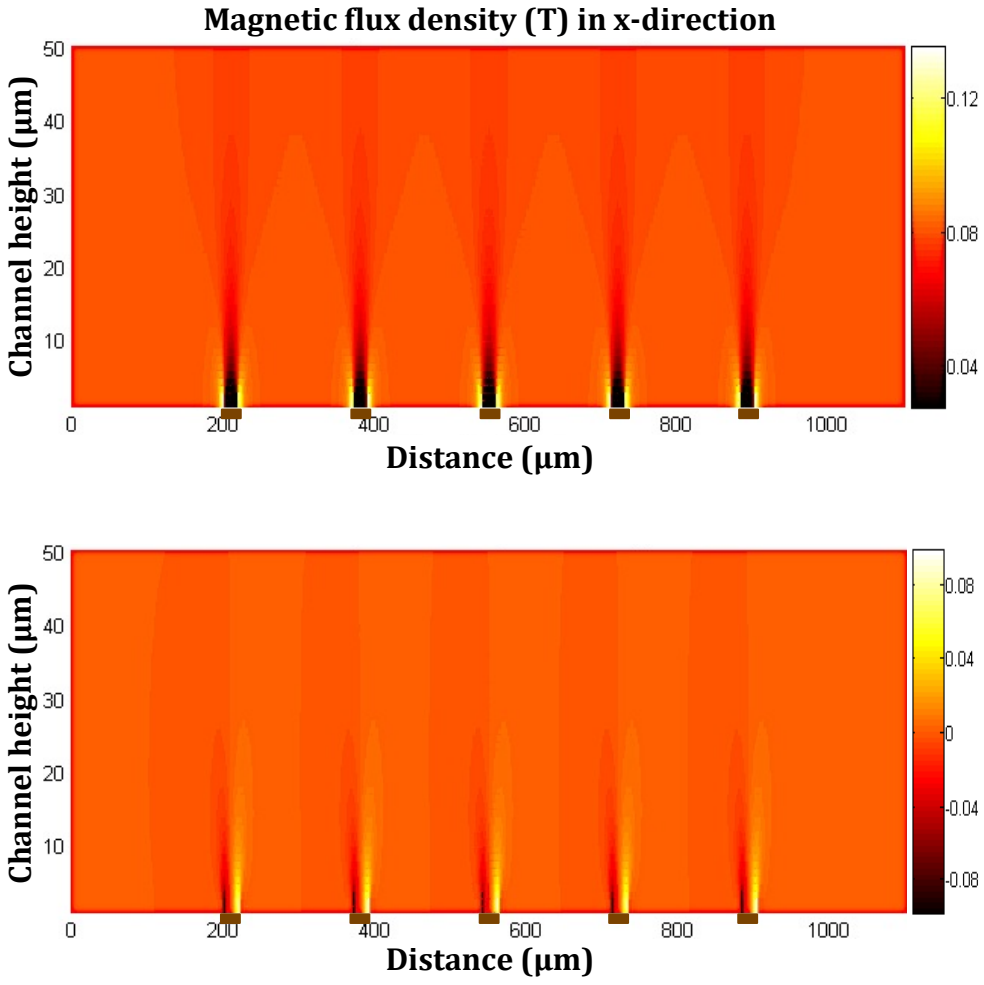

Figure 2.14: Magnetic field distribution within the microfluidic channel space obtained using COMSOL. The strongest spots of the magnetic field are around the edges of the micromagnets in x direction and y direction.

The results can be seen in Figure 2.14, where the micromagnet is shown as a brown box (indicating only the later position). The magnetic field distribution is calculated using finite element method (FEM) software COMSOL.

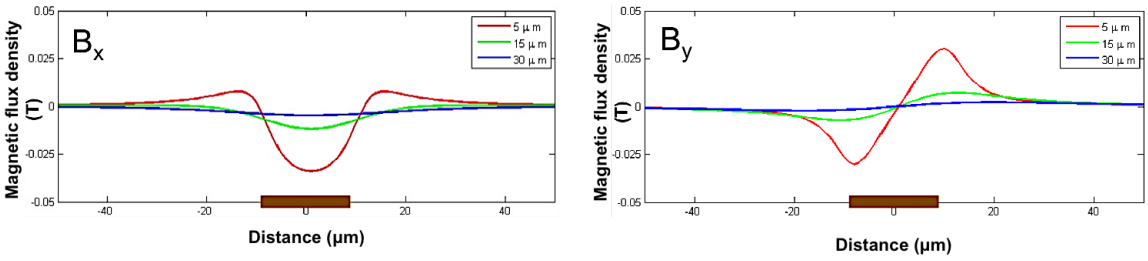

Figure 2.15: Magnetic flux density calculated for a single micromagnet element. The gray box indicates the lateral position of the micromagnet. The curves were plotted along horizontal lines with different heights (h =5 μm, 15 μm and 30 μm) on top of a single micromagnet.

Figure 2.15 shows the calculated results of a single micromagnet. In the lateral direction, the magnetic field becomes completely flat outside the range of ~40 ± 5 μm. While in the vertical direction, the magnetic field decays fast as the distance to the micromagnet increasing and turns into a straight line with value equaled to 0 T at the height of 30 μm. The magnetic force is dependent on the gradient of the magnetic field (∇B^2) based on our previously proposed theory [80]. Therefore, the lateral interaction distance of the patterned thin-film micromagnets was 50 μm ~ 60 μm in total, with the vertical interaction distance being ~30 μm.

In addition, we also performed calculations for micromagnet array (here, an array consisting of five micromagnet was used), with the external magnetization along the horizontal direction. The dimension of each micromagnet was consistent with the single element study (20 μm × 250 nm), and the edge-to-edge space between adjacent micromagnets was 100 μm. We calculated the magnetic field X/Y components along a

horizontal line 10 μm above the micromagnet array. The array generated a magnetic field with profiles just like the spatially reproducible ones from a single micromagnet based on the results in Figure 2.15. Key features, including the shape and interaction distances of each element remain the same in the array.

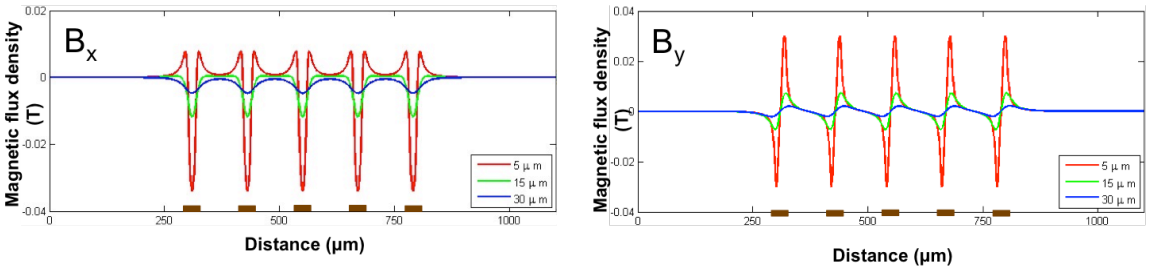

Figure 2.16: Magnetic flux density calculated for an array of five micromagnets. The curves were plotted along horizontal lines with different heights (h =5 μm, 15 μm and 30 μm) on top of micromagnets.

The magnetic field distribution can be further optimized by adjusting the dimensions of each micromagnet, spatial periodicity of the array, especially considering the high variances of the field intensity, and direction of the external magnetic field generated by the permanent magnets.

2.3 Summary

We first introduce the principle of antibodies modifying the magnetic carrier surface so that it can be used to bind to the cell surface. We then discuss the simulation and modeling of the flow field and magnetic field distribution in the microchannel. Three types of microdevices, including glass coverslip substrate, coverslip substrate with a spacer placed close to the inlet, and glass slide substrate, are presented. Key parameters, such as magnetic force and hydrodynamic force, acting on the magnetic carrier-tagged cell in the microchannel, channel height, flow rate, magnetic carrier diameter, and distribution of magnetic micromagnets on the channel substrate, are discussed as well.

Chapter 3

Experimental Design and Protocol

To achieve highly efficient detection of rare cancer cells in whole-blood samples, we describe a new method of microchip-based immunomagnetic screening system, in which the benefits of both immunomagnetic assay and the microfluidic device are combined. The screening system is operated in a flip-flop mode, where a computer-controlled rotational holder and rocking of reservoirs with an array of microfluidic chips inverts the microchannels. We discuss key components necessary for the screening system.

First, we introduce the design and fabrication of the microfluidic device. Next, comparisons of different magnetic field arrangements, including orthogonal and parallel arranged permanent magnets—with and without a spacer between permanent magnets and the channel substrate—and an array of micromagnets patterned on the channel, are discussed. We then show the sample preparation for the screening of cell separation. After introducing the sample preparation and screening process, we give the details of the staining and identification of isolated cancer cells. Last, we talk about the downstream analysis of captured cells.

3.1 SCREENING SYSTEM

The computer-controlled screening system was developed to achieve high capture efficiency of separation of circulating tumor cells for further genomic study. The system consists of biocompatible microchip, arranged permanent magnets, patterned micromagnets, magnetic nanoparticles, etc.

3.1.1 Microfluidic chip

The microchannel is made by a standard molding technique using polydimethylsiloxane (PDMS) (Sylgard184, Dow Corning, Midland, MI, 10:1 prepolymer to curing agent). Laser cut acrylic master was attached to a plain acrylic plate to be a master. An aluminum mold was screwed to the acrylic plate. PDMS was then poured to the mold and put in the oven for four hours with 50ºC. After being cured, PDMS chip was bonded on a glass bottom substrate, which serves as a sample slide for the captured tumor cells. Dimensions of the micro-channel are shown in Figure 3.1 (a). Blood sample filling the microchannel is shown in Figure 3.1 (b).

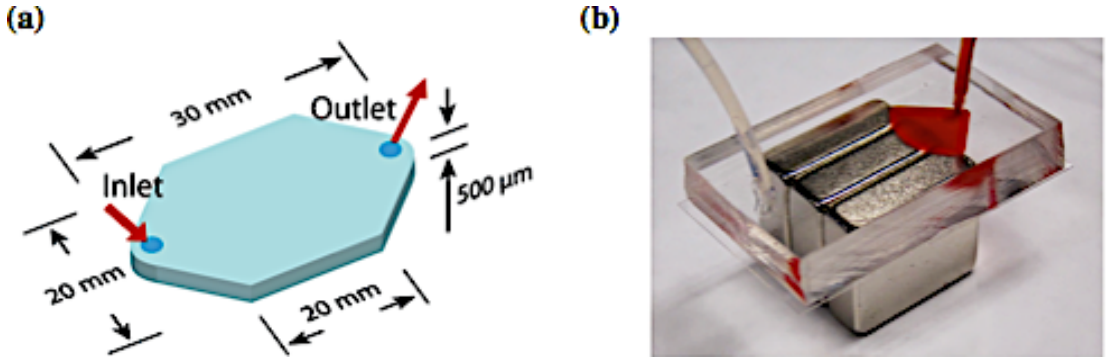

Figure 3.1: (a) Dimensions of the microchannel. (b) Photograph of the fabricated microfluidic device shows that blood is filling the microchannel. [34]

PDMS microchips are pre-cleaned with methanol solution. Both PDMS microchip surface and micromagnets-patterned glass slide substrate undergo O_2 plasma (Nordsom march asher PX-250) treatment for 2 minutes. Next, treated surfaces of PDMS microchip and glass slide substrate are then bonded to each other.

Inlet tubing was connected to 14 mm long soft silicon rubber tubing (McMASTER-CARR), while the other end of tubing was connected to a 19 gauge flat-head needle (McMASTER-CARR), which was used to connect to a reservoir. The outlet

tubing was connected to 40 mm long soft silicon rubber tubing that the other end of tubing was connected to a female luer fitting, which was used to connect to a waste syringe.

Micromagnets are fabricated by standard photolithography, thermal deposition, and lift-off technique. Fabrication process is shown in Figure 3.2.

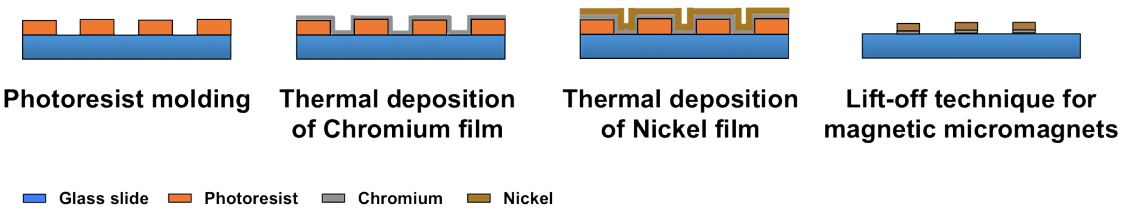

Figure 3.2: Fabrication of magnetic micromagnets on a glass substrate.

Firstly, patterns of micromagnets are defined by spin-coating the positive photoresist (AZ5209) onto the standard glass slide. Patterns of the micromagnets were then photo-defined on photoresist by selective exposure to UV light through a photo-mask. The residual photoresist on the glass substrate is removed by the O_2 plasma (Nordsom march asher PX-250). Next, 15 nm thick chromium layer was thermally deposited as the adhesion layer after which the 250 nm thick nickel metal material was thermally deposited on a photoresist-patterned glass substrate to form micromagnet structure. In the last fabrication step, lift-off technique was used to remove patterned photoresist and leave behind an array of magnetic micromagnets.

3.1.2 Magnetic field measurement

For the efficient attraction of magnetic nanoparticles, which essentially act as small dipoles, magnetic field gradient rather than absolute field strength is required. A

strong but uniform magnetic field rotates the dipole orientation but does not attract it. Alternately arranged magnets with opposite polarities next to each other make a large gradient. A strong magnetic gradient is created to attract magnetic nanoparticles between adjacent magnets.

To assess the efficacy of the magnetic field, control experiments with ferrofluid nanoparticles suspended in a buffer solution were performed with different magnet orientations. Optical densities of the nanoparticle solution were used to obtain quantitative evaluation of the capture efficiency of magnetic particles. We tested two types of magnet orientations.

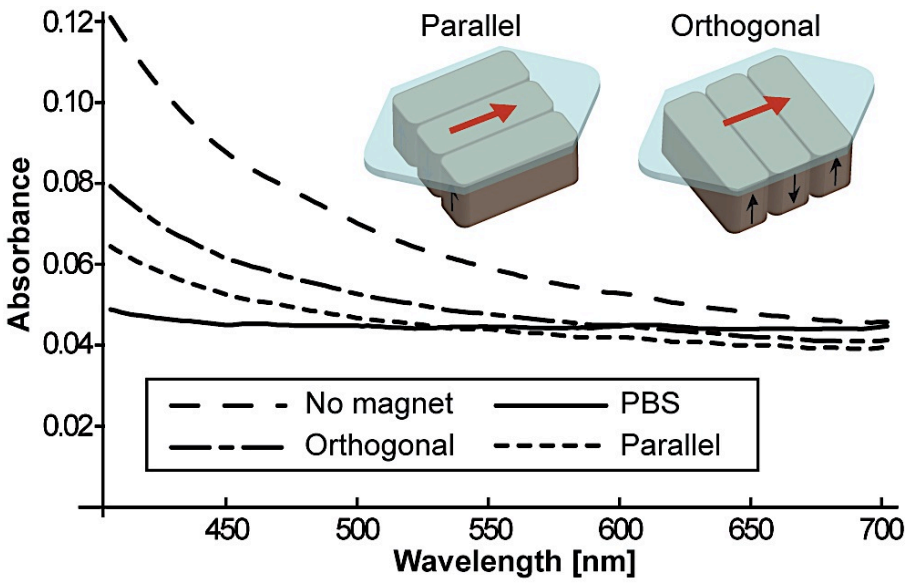

Figure 3.3: Control screening experiment with only nanoparticles in buffer solution in the flow channel. Optical transmission is measured for orthogonal and parallel arrangements of magnets. The parallel arrangement showed the better capture efficiency. [34]

Figure 3.3 is the result of the measurements with three magnets placed in orthogonal and parallel arrangement with regard to the flow direction. With lower flow

rates, such as 5 mL/hour, almost all of the particles are captured, and it is difficult to assess the capture efficiency. Therefore the flow rate was deliberately set to be 40 mL/hr for the measurements, which is much higher than those used in experiments involving cancer cells. The dominant areas for attracting magnetic nanoparticles are the lines between two adjacent magnets. The parallel arrangement gives particles longer exposure to the magnetic field gradient induced by those areas. All of the following experiments were made with the three magnets in the parallel arrangement.

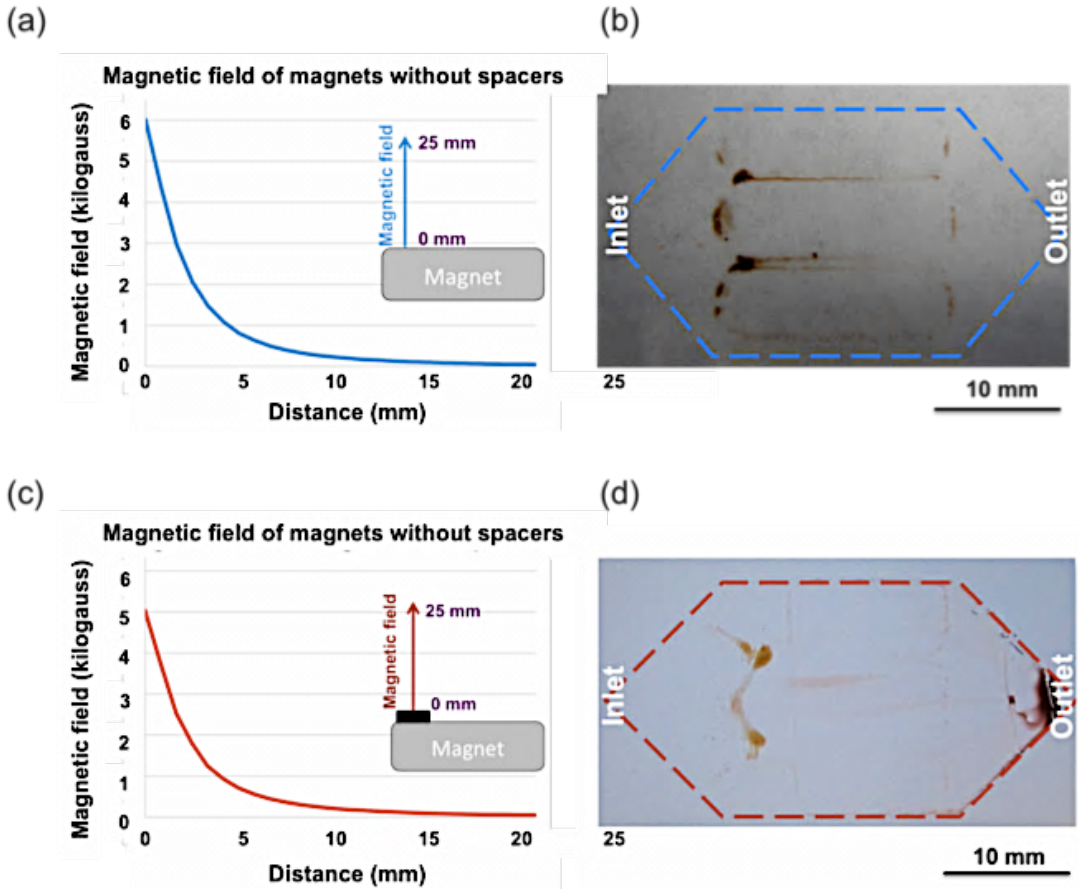

Figure 3.4: (a) Measured magnetic field of a permanent magnet without any spacers. (b) More nanoparticles aggregated close to the front end of the glass coverslip when no spacer was induced. (c) Measured magnetic field of a permanent magnet together with a spacer. (d) Fewer nanoparticles aggregate in the front end of the glass coverslip. [35]

Figure 3.4(a) shows the measured magnetic field induced by a permanent magnet without any spacers. The distribution of nanoparticles on the channel substrate after the screening is shown in Figure 3.4(b). Many particles were aggregated on the glass coverslip substrate along the strong magnetic field. Figure 3.4(c) shows the measured magnetic field of a permanent magnet attached with a spacer. With the spacer, fewer nanoparticle aggregates can be seen in the front end of the microchip, as shown in Figure 3.4(d).

It is observed that the spacer decreases the magnetic field, reducing the gradient, and thus reducing the magnetic force acting on nanoparticles in the microchannel. Magnetic field flux density distribution for a plane 200 μm away from the channel substrate with no spacers placed on top of the magnets is shown in Figure 3.4(c). Moreover, in order to prove that the cells will be captured onto the surface of the microchannel, we compare the magnetic flux density at the bottom and the top of the channel as shown in Figure 3.4(d).

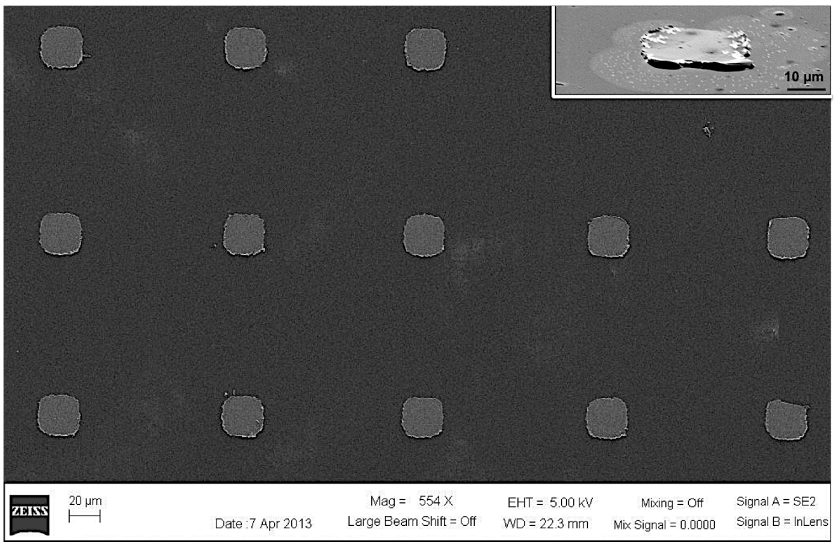

Figure 3.5: SEM images of the fabricated patterned thin film micromagnets. The size of a single micromagnet is 20 μm ×20 μm ×250 nm, and edge-to-edge distance between adjacent patterns is 100 μm. Inset shows a fabricated micromagnet.

Figure 3.5 shows the scanning electron microscope (SEM) of images of the top view of an array of fabricated micromagnets. The inset shows overview of one single micromagnet. The dimension of one micromagnet is 20 μm ×20 μm ×250 nm. The distance from the edge of one micromagnet to the edge of another one is designed to be 100 μm.

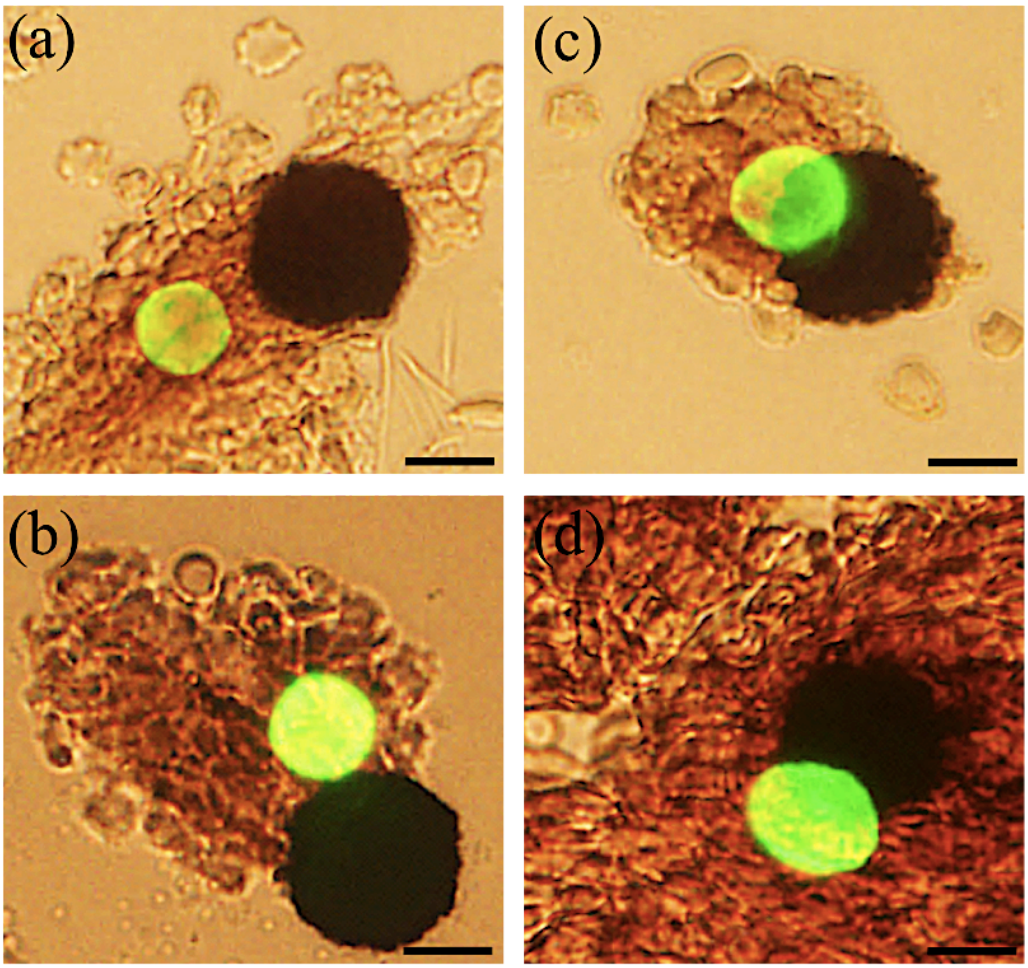

Figure 3.6: Overlay of fluorescent image and bright field image of a FITC-stained cancer cell captured by a micromagnet magnetically, while free nanoparticles were attracted to a micromagnet. (a) A cancer cell is captured by aggregated free nanoparticles. (b) A cancer cell is captured next to a micromagnet. (c)(d) A cancer cell is captured on top of a micromagnet. Scale bar is 10 μm.

Figure 3.6 shows an overlay of a bright field image of nanoparticles and a micromagnet, as well as a cancer cell stained with FITC (green) captured either by aggregated nanoparticles that are attracted to a micromagnet magnetically Figure 3.6(a), next to a micromagnet Figure 3.6(b), or by the micromagnet Figure 3.6(b)(d).

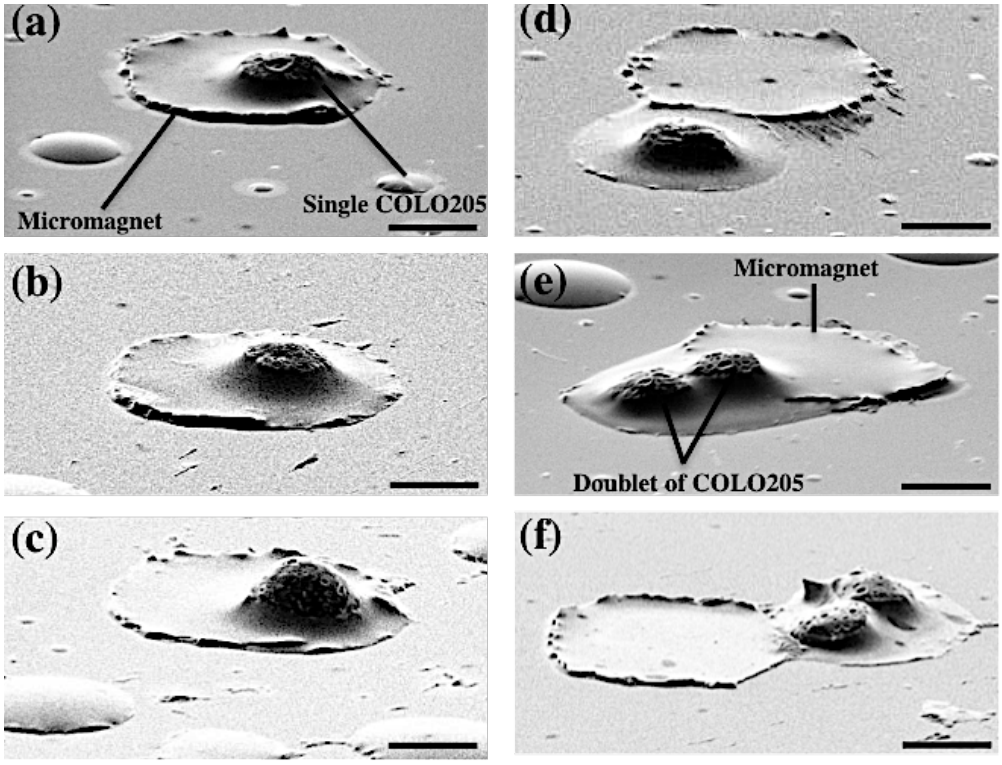

Figure 3.7: SEM images of a single COLO 205 cancer cell (breast cancer cell line) or one doublet captured by a micromagnet. Scale bar is 10 μm. (a)(b)(c) One single cancer cell captured on top of a micromagnet. (d) A cancer cell captured next to a micromagnet. (e)(f) Two cancer cells captured next to a micromagnet.

Figure 3.7 shows the SEM images of a COLO 205 cancer cell or doublet captured by a micromagnet. The scale bar is 10 μm. Figure 3.7 (a), (b), and (c) show the cancer cell captured on top of the micromagnet. The cell in the Figure 3.7 (d) is captured next to the micromagnet. In Figure 3.7 (e) and (f), two cancer cells are captured next to the micromagnet.

3.1.3 Rocking of the reservoir

In order to prevent the blood cells from settling down in the reservoir, which would cause damage to the target cancer cells in the blood sample, a rocking system has been designed to keep the blood sample mixed during the screening process. Figure 3.8 shows the rocking of an array of microchips during the screening process [35].

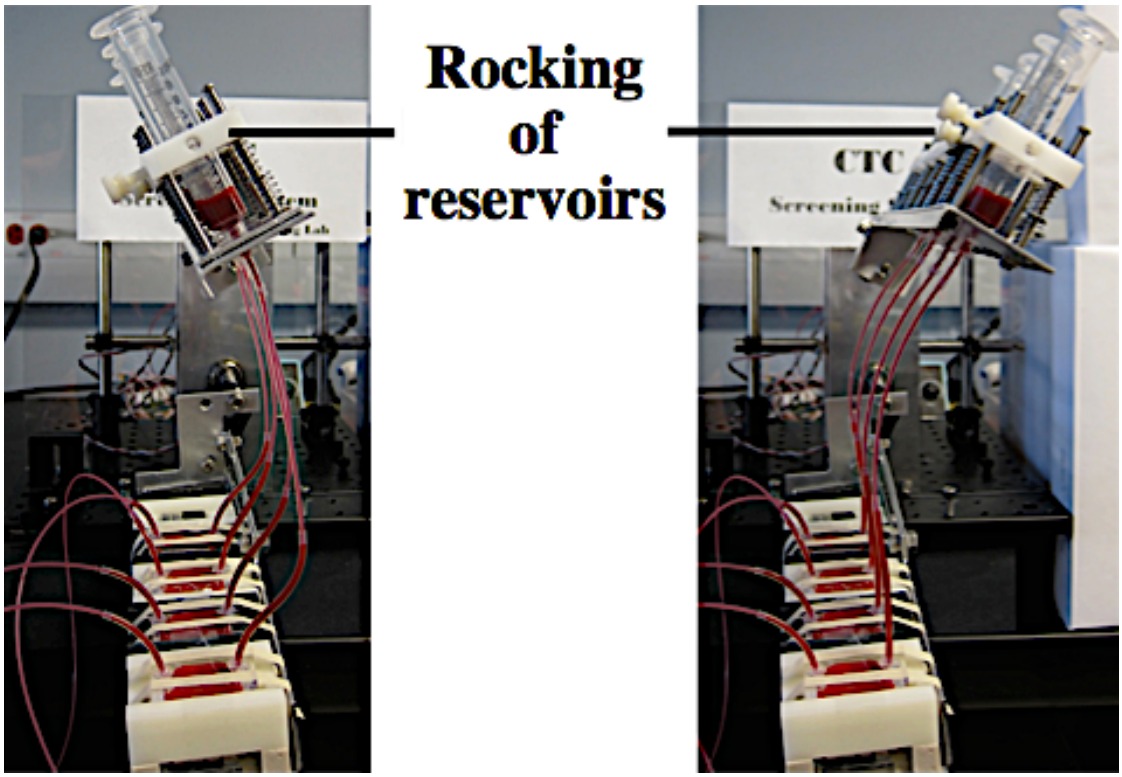

Figure 3.8: Automated screening system for rocking of microchips. [35]

3.1.4 Flip-flop of microchips

We developed an automatic rotational microchip holder, which comprises DC motors and optical position sensors. Figure 3.9 shows the developed screening system. A

LabVIEW program is used to control the position of the rotating arm. The system is able to dynamically rotate the orientation of the microfluidic chips to keep them operating in the best orientation during the screening process. The screening system is capable of screening up to six samples simultaneously [35].

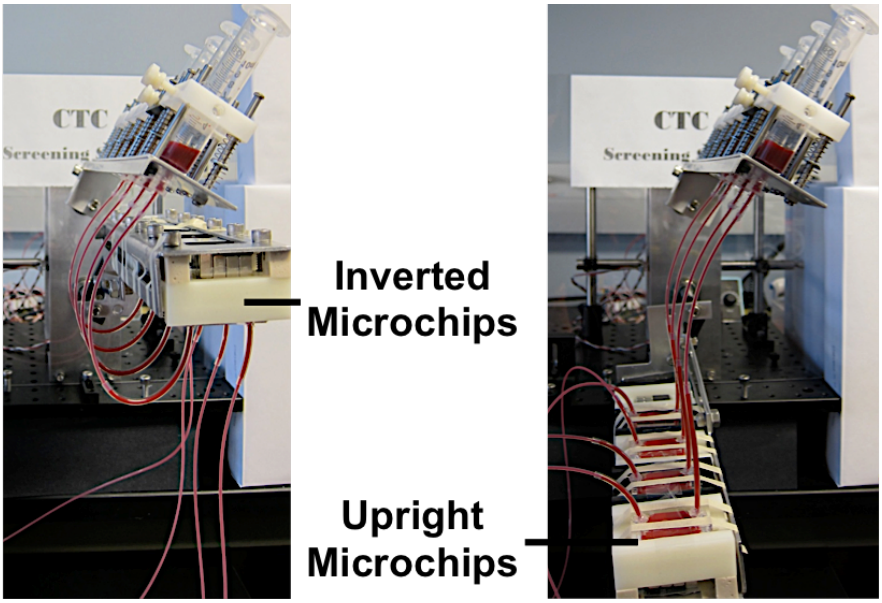

Figure 3.9: Automated screening system for parallel screening and rotation of microchips. [35]

3.2 SCREENING EXPERIMENT AND RESULTS

3.2.1 Blood sample preparation

Blood samples from a healthy donor were spiked with control cancer cell lines and screened to calculate the capture rates. Vacutainer™ tubes (BD, Franklin Lakes, NJ) containing ethylenediaminetetraacetic acid as an anticoagulant (EDTA tubes), and CellSave™ tubes (Veridex, LLC, NJ) were used to draw blood. We used several human cancer cell lines, including COLO 205 (a type of colorectal cancer), SK-BR-3 (a type of

breast cancer), MCF-7 (a type of breast cancer), and PC3 (a type of prostate cancer) to provide a good simulation of clinical screening.

First, cultured cells were harvested, centrifuged, and re-suspended in either buffer solution. Cells were counted with a hemocytometer and diluted in phosphate-buffered-saline (PBS) to prepare a solution with approximately 20,000 cells/mL. Then, 10 μL of cell suspension were added to each 2.5 mL aliquot of whole blood to prepare a sample spiked with 200 cells. The same amount of solution (10 μL) was also dispensed on each of two glass slides as counting controls. The number of cells actually spiked into the blood was determined by using the average of the two control slides as 100%, and then the percent recovery was calculated. Control blood samples, which were not spiked with cancer cells, were prepared along with spiked ones, and all of the following procedures were performed in parallel.

The blood samples we prepared in CellSave™ tubes were screened 24–48 hours after spiking, simulating the actual screening situation of patient blood. The CellSave™ tube contains fixative agent so that samples can be sent from areas that are distant from the laboratories. In addition, we performed testing with blood prepared in standard EDTA tubes as a reference. The EDTA tube we used here (Vacutainer™ tube) is for general-purpose blood collection and does not contain preservative or fixative agents. The samples were screened just after spiking to minimize possible antigen deactivation. A blood sample collected in either an EDAT tube or a CellSave™ tube was added to a conical polypropylene falcon tube (BD, Frenklin Lakes, NJ) so that each conical tube contained 2.5 mL of blood sample.

Before screening, the blood was processed as follows: first, 2.2 mL of dilution buffer solution (Veridex, LLC, NJ) was added to the 2.5 mL of whole-blood sample and centrifuged at 800G for 10 minutes. Supernatant containing plasma as well as the dilution buffer solution was removed, and the buffer solution was added again to make a total volume of 3.5 mL of the screening sample. These steps replaced blood plasma with the

dilution buffer solution. The CellSave™ tubes contain cell-fixative reagents and tend to make the blood sample more viscous than the EDTA samples. Viscosities of blood samples collected in an EDTA tube and a CellSave™ tube were measured after the dilution step. Second, a suspension of anti-epithelial cell adhesion molecule (EpCAM) functionalized Fe_3O_4 nanoparticles (18.8 μL) were added to the blood sample. Then the blood sample mixed with nanoparticles was manually mixed upside down 15 times. Next, 18.8 μL of capture-enhancement reagent (Veridex, LLC, NJ) were added to the blood. The blood sample was again mixed upside down another 15 times. The sample was then incubated in a strong magnetic environment provided by the immunicon magnetic cell separator quadrupole flow for 10 minutes, while 75 μL is the standard amount used in the CellSearch® system.

Therefore, only 25% of the amount used in the commercially available CellSearch® system was used for the screening experiments here. The whole sample preparation process took about two hours.

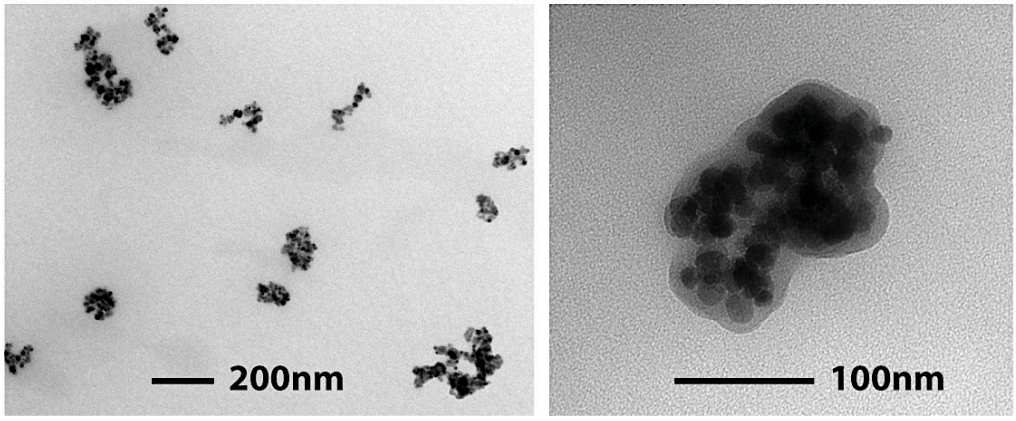

Figure 3.10: TEM images of Fe_3O_4 magnetic nanoparticles (Ferrofluids). [34]

A commercial Fe_3O_4 nanoparticle (Ferrofluid®, Veridex, LLC, NJ), which has been functionalized with anti-EpCAM, is used to tag cancer cells for immunomagnetic

separation purpose. The typical sizes of Fe_3O_4 nanoparticles range from 100 nm to 200 nm. Figure 3.10 shows the TEM images of magnetic nanoparticles (Ferrofluids) [34].

3.2.2 Separation process

Before the blood sample was transferred into the reservoir from the conical tube, the microchannel was filled with PBS to eject air bubbles. Blood samples were then transferred from conical tubes to the reservoirs by an automatic pipette. Next, the spiked samples were driven pneumatically at a continuous rate by a syringe pump (Standard Infuse/Withdraw PHD 22/2000 Syringe Pumps, Harvard apparatus). Flow rate was set to be 2.5 mL/hour during the separation process.

After the blood sample flowed through the microchannel, the flushing step was introduced to continuously flow PBS into the microchannel to remove unlabeled cells, including red blood cells (RBCs), white blood cells (WBCs), and nontarget cells from the microchannel substrate. The flow rate for the flushing step was 5 mL/hour. Typically 4 mL of PBS was added. The screened microchip was then cooled down by ice for 10 minutes. After flushing, 1 mL of ice-cold acetone at the same rate (5 mL/hour) was introduced to the channel to fix cancer cells on to the glass slide substrate. After being disassembled from the PDMS microchip and dried completely, the bottom glass slide was stored at 4°C until staining.

3.2.3 Immunofluorescence staining

The captured cells were fluorescently stained with anti-cytokeratin (CK, protein found in epithelial tissue, positive test, Mouse anti-cytokeratin, pan-FITC, Sigma-Aldrich, St. Louis, MO), anti-CD45 (found on leukocytes, negative test), and DAPI

(stains DNA found in cell nucleus, positive test; Vectashield Mounting Medium with DAPI, Vector Laboratories, Inc., Burlingame, CA).

First, the sample slide was rinsed/rehydrated with PBS solution containing 0.1% Tween 20 (Boca Scientific) for five minutes. A KimWipe was then used to remove excessive solution. Second, blocking buffer (Boca Scientific) was added on the sample slide for five minutes. The sample slide was incubated for one hour. Again, excessive solution was removed by using a KimWipe. Next, the sample slide was rinsed with PBS once. Excessive PBS was then removed. Staining solution (300 μL), including anti-CK and anti-CD45, was added to the slide. The incubation step was used for the sample slide. After the 45-minutes incubation, the sample slide was immersed in PBS containing 0.1% Tween 20 three times for five minutes each. Next, a mixture of DAPI and mounting media (the ratio was set to be one to one) was added to the sample slide. A coverslip was used to cover the glass slide. Finally, the stained sample slide was stored at 4°C for thirty minutes before following the cell identification step.

3.2.4 Identification of captured and stained cells

Figure 3.11 shows fluorescence images of a captured COLO 205 cell and a leukocyte using a color CCD camera (Olympus DP72) and separate filter cubes for red [excitation peak wavelength (Ex) 535 nm, bandwidth (BW) 50nm, dichroic mirror (DM) 565 nm long-pass (LP) and emission peak wavelength (EM) 610 nm, BW 75 nm], green (Ex 480 nm BW 40 nm, DM 505 nm LP, Em 535 nm BW50 nm) and blue (Ex 350 nm BW 50 nm, DM 400 nm LP, Em 460 nm BW50 nm).

A trained observer distinguished cancer cells from other cells that remained on the slide after the flushing step. Cancer cells are (a) DAPI positive, (b) CK positive, and (c) CD45 negative, while leukocytes are (d) DAPI positive, (e) CK negative, and (f) CD45

positive, as shown in Figure 3.11. The bottom raw picture in Figure 3.11 shows one example of captured CTC and WBCs stained with DAPI, CK, and CD45.

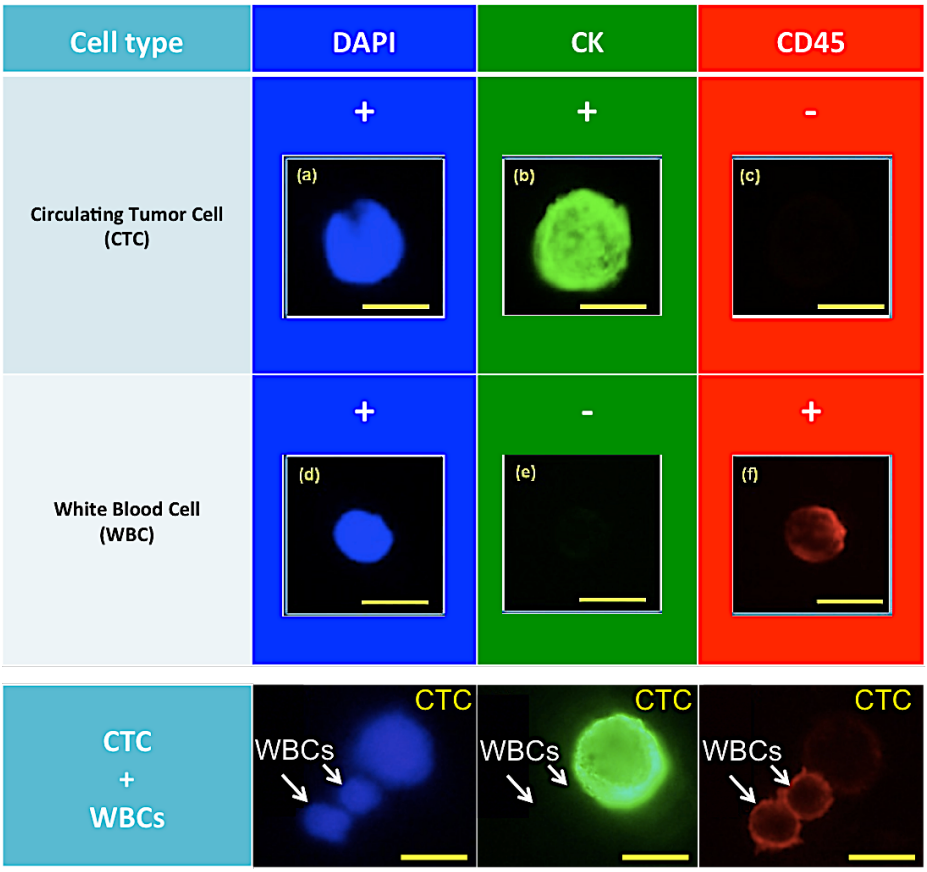

Figure 3.11: Example of (a) DAPI (blue), (b) CK (green), and (c) CD45 (red) fluorescence images of capture COLO205 cell. (d) DAPI, (e) CK, and (f) CD45 images of a white blood cell, which shows clear CK negative and CD45 positive images, is also shown. Scale bar = 10 μm. An example of fluorescence image of a CTC along with two WBCs is shown in the bottom raw picture.

To implement objective identification, numerical analysis of the size and the fluorescence values of cells were performed. Fluorescence intensity was accessed by Weber contrast defined as follows:

$$C = \frac{I - I_b}{I_b} \tag{3.1}$$

in which I is the mean intensity of a cell and I_b is the background intensity. An idealized diameter was calculated from the cell area of a binary image calculated from the cytokeratin image.

	Mean	Standard Deviation
DAPI	6.6	2.0
CK	9.5	1.7
CD45	0.6	0.3
Diameter (μm)	15.2	2.2

Table 3.1: Mean value and standard deviations of fluorescence intensities as contrast values and idealized diameters of captured COLO 205 cells. [34]

Table 3.1 shows the mean values and the standard deviations of the three fluorescent contrast values and the idealized diameters for 61 cells identified as cancer cells by a trained observer. Based on the values, we made a normalized evaluation function in the following formula:

$$E = \frac{(DAPI - \overline{DAPI})^2}{\sigma_{CD45}^2} + \frac{(CK - \overline{CK})^2}{\sigma_{CK}^2} + \frac{(CD45 - \overline{CD45})^2}{\sigma_{CD45}^2} + \frac{(Dia. - \overline{Dia.})^2}{\sigma_{Dia.}^2} \tag{3.2}$$

where $DAPI$, CK, $CD45$ and $Dia.$ are the contrast values and the diameter of a single cell, $\overline{DAPI}$, $\overline{CK}$, $\overline{CD45}$, and $\overline{Dia.}$ are the mean contrast values and diameter of the 61 cells, and σ_{DAPI}, σ_{CK}, σ_{CD45}, and $\sigma_{Dia.}$ are the standard deviations of the contrast values and the diameters of the same 61 cells, respectively. We found that 60 of the 61 cancer cells

satisfied $E < 10$, 55 satisfied $E < 8$, and 50 satisfied $E < 5$, while none of the cells identified as noncancer cells satisfied the same criteria. The largest E value found among cancer cells was 11.9, which was the only cancer cell with an E value higher than 10. This was caused by a large diameter (21.9 μm, contribution to E: 9.6). Other larger E values tend to be caused by a large diameter or an intense *CK* value (largest contribution from *CK*: 7.5). On the other hand, the two smallest E values found in noncancer cells were 10.7 and 13.6, which were exceptionally small. For other noncancer cells, even though we just calculated E values for those that were somehow categorized as "confusing" cells, values were mostly more than 30 or even more than 100. $E = 10$ seems to be a safe value as an elimination factor. The result ensures its agreement with the subjective cell-identification process made by the trained observer, as well as the feasibility of a future computer-based automated cell-identification process.

3.3 DOWNSTREAM ANALYSIS

To analyze the cells and to acquire genomic information, such as cancer stage, epithelial to mesenchymal transition (EMT) status of cancer cells, and molecular biomarkers for different cancer types, DNA and RNA are extracted from the collected cancer cells by using the fluorescence in-situ hybridization (FISH).

We prepared spiked samples and screened patient samples for the FISH experiment. We spiked two breast cancer cell lines for the spiked experiments. Those cell lines were SK-BR-3 and MDA-MB-231. Each sample slide was spiked with ~2000 cancer cells. Patient sample slides from two different breast cancer patients were also prepared. Two probes, including chromosomes 17 (CEP17) and HER-2/neu, were used along with dual-color fluorescence signal for the FISH experiment. The slide was immersed in the 1X PBS solution for two hours to remove the coverslip and the DAPI

mounting medium. The FISH experiment was mainly performed at the Department of Pathology, the University of Southwestern Medical Center.

3.4 Summary

We introduced the experimental setup, including design and fabrication of the microfluidic device, magnetic field arrangements (external magnetic field and micromagnet), blood sample preparation, sample staining, and identification. Furthermore, we discussed the downstream analysis, which is FISH, for captured cancer cells.

For the developed screening system, we significantly reduced the cost of the system so that the amount of nanoparticle suspension added was also reduced to 25% of the amount used in the commercially available CellSearch® system. Such microchip-based CTC detection in patient blood enables new diagnostic tools to record the status of disease activity as well as clonal evolution of molecular changes for early cancer detection.

Chapter 4

CTC screening system and Downstream analysis

We demonstrate the capability of the screening system by discussing some key parameters, such as the capture efficiency of upright microchip and inverted microchip, and the effect of red blood cells sedimentation on the capture of cancer cells. Furthermore, the stability test and selectivity test of the screening system are included. Since the system has been successfully applied for patient sample screening, the results are also presented in the chapter. Last, the results of genetic study of collected cancer cells from spiked samples and patient samples by using the fluorescence in-situ hybridization (FISH) method are discussed.

4.1 SCREENING OF SPIKED SAMPLES

In order to optimize the magnetic field distribution in the microchannel, we designed different arrangements of magnets for the capture efficiency test. Magnetic field distribution was theoretically studied and experimentally measured. COMSOL was used for simulation of the magnetic field. Optical density measurement was used for a particle-only experiment to assess the capture efficiency to optimize the magnetic field arrangement.

4.1.1 Gravity effect

We describe a computational analysis method to evaluate the efficacy of immunomagnetic rare cell separation from non-Newtonian particulate blood flow. We calculate local viscosity distributions induced by red blood cells (RBCs) sedimentation. A sedimentation and viscosity model is introduced based on the experimental

measurements. The computational field is divided into small unit-control volumes, where the local viscosity distribution is dynamically calculated based on the experimentally found sedimentation model. For analysis of rare cell separation, the local viscosity distribution is calculated as a function of the volume RBC rate. The direction of gravity has an important role in such a sedimentation-involved cell-separation system. We evaluated the separation efficacy with multiple design parameters including the channel design, channel operational orientations (inverted and upright), and flow rates. The results showed excellent agreement with real experiments to demonstrate the effectiveness of our computational analytical method. We demonstrated higher capture efficiency with the inverted microchannel configuration. We conclude that proper direction of blood sedimentation significantly enhances separation efficiency in microfluidic devices.

We performed experimental measurements to calibrate the relation between the RBC volumetric concentration and local viscosity, using a cone plate viscometer (DV-I+, Brookefield, Middleboro, MA). We used a centrifugal process to replace blood plasma with a buffer solution. It is possible to replace plasma without significantly losing rare cells contained in blood. Samples were prepared in the following way: first 2.5 mL of blood is drawn from a healthy subject, added with 3.5 mL of PBS, and centrifuged at a relative centrifugal force (RCF) of 800G for 10 min. Supernatant containing plasma as well as buffer and formed sediment of white blood cells and platelets is removed.

Table 4.1 shows the viscosity of the EDTA tube containing the blood sample and the viscosity of the CellSave™ tube, which has the blood sample. The shear rate we used for the measurement was $2s^{-1}$. The below equation shows the viscosity.

$$cP = 10^{-3}\, kg \cdot m^{-1} \cdot s^{-1} \tag{4.1}$$

Tube	EDTA	CellSave™
Shear rate ($2s^{-1}$)	6.1 cP	7.2 cP
Shear rate ($20s^{-1}$)	3.3 cP	3.9 cP
Shear rate ($200s^{-1}$)	2.3 cP	3.0 cP

Table 4.1: Measurement of viscosities of blood samples contained in an EDTA tube and a CellSave™ tube.

The results are shown in Table 4.2. Obviously, the viscosity is directly proportional to the RBC volumetric concentration, with an approximately linear relationship. The buffer solution is added again to make the suspensions with volume RBC rates ϱ_{RBC} = 50, 25, 12.5, 6.3, and 3.1. The processed blood is mixed well, and 2 mL of the sample is measured in a transparent tube with an inside diameter of 4.2 mm and kept stable for hours.

Red blood cell volumetric concentration	50	25	12.5	6.3	3.1
Viscosity (cP)	18.4	15.3	6.13	7.15	5.11

Table 4.2: Measurement results of viscosities of different RBC volumetric concentration

In order to study the effect of blood sedimentation on cell separation, we performed comparative experiments of real cancer cell separation with different channel orientations to acquire the capture efficiency. The conditions used here are as follows:

(a) Upright, flow rate 10 mL/h, standard channel (channel width = 17 mm)

(b) Inverted, flow rate 10 mL/h, standard channel (channel width = 17 mm)

For each condition, we performed two experiments with the real microchannel. Noteworthy is that we used a rotational holder to place microchannels in an inverted or upright position. A 100 μL aliquot of cancer cell suspension that contains an average of 150 COLO 205 cells is spiked in 2.5 mL of healthy blood sample. Blood plasma was replaced with buffer solution. When we removed plasma after the centrifugal process, care was taken not to disturb the thin layer between plasma and RBC and to save rare cells contained there. The number of magnetic particles (N) attached to a rare cell depends on several experimental conditions such as the type of the rare cell, amount of antigen expression on the cell surface, concentration of introduced magnetic nanoparticles, and so on. We first found N = 20,000 to match the simulation and experimental rare cell capture rates for condition a; then the same condition of N = 20,000 was used for all the other conditions of b–d. Note that in the case of our simulation, the capture rate is a monotonically increasing function of N.

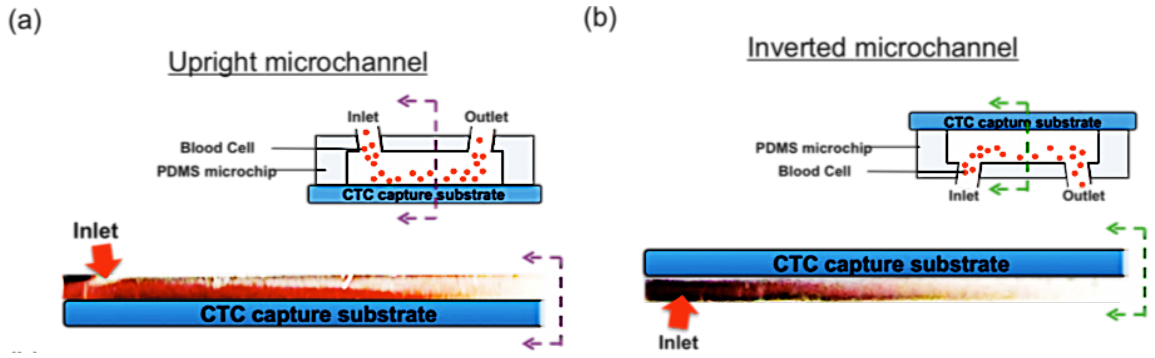

Figure 4.1: Experimental images of blood sedimentation in microchip of a flip-flop operation. (a) Sedimentation layer of RBCs is on the CTC capture substrate that acts as a barrier for the capture of CTC in the upright channel. (b) RBC sedimentation layer covers the opposite plane of the CTC capture substrate that target CTCs experience less viscous force by the RBCs to be captured on the CTC capture substrate. [35]

Figure 4.1 shows the experimental results of RBC sedimentation in the upright channel and the inverted channel. The microchannel was filled with PBS followed by the introduction of RBCs suspension. The flow rate was set to be 10 mL/h. With the upright channel, RBC sedimentation covers the bottom substrate, which is the CTC capture substrate. It is observed that the substrate is being covered by the layer of RBCs, as shown in Figure 4.1(a), in the upright case. Figure 4.1(b) is the inverted channel. Therefore, in the upright channel, RBCs sedimentation on the CTC capture substrate acts as a barrier layer for target cells to be captured on the substrate. Compared to the upright channel, nanoparticle-labeled target cells can be easily attracted to the channel substrate in the inverted channel.

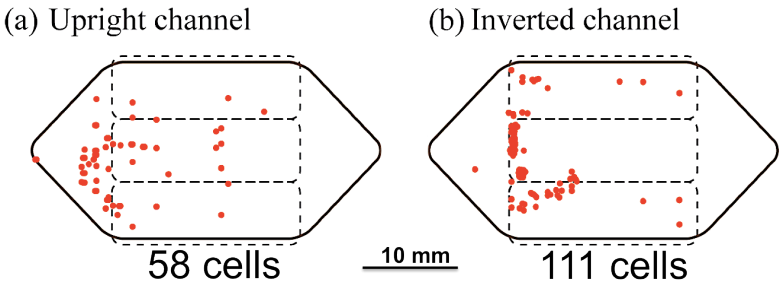

Figure 4.2: Map of spiked cancer cells (COLO 205 cells) on the glass coverslip. (a) On the upright channel, fewer cancer cells (58 cells). (b) More cancer cells (111 cells) were captured by the inverted channel. [35]

Maps of the captured CTCs are shown in Figure 4.2 for both experiments and simulations. For the experiments, locations of the captured cells were recorded with a mechanical positioning stage. In addition, an average of 150 cells (COLO 205 cell line) were spiked into the blood sample for the experiments. On the upright channel [Figure 4.2 (a)], 58 cells were found on the coverslip while on the inverted channel, more cancer cells (111 cells) were found on the coverslip [Figure 4.2 (b)]. Because of high viscosity of the dense RBC layer that covers the capture surface, the upright channel shows low

capture efficiency compared to the inverted channel. Due to a high viscous layer of RBCs covering the substrate in the upright channel, it is more difficult for cancer cells to get close to and finally be captured onto the channel substrate. Therefore, more cells are captured on the channel substrate of the inverted channel in comparison to the cells captured on the substrate of the upright channel.

4.1.2 Capability performance

We performed screening experiments with different numbers of COLO 205 cells spiked in the samples ranging from ~10 to ~1500 in 2.5mL blood samples. CellSave™ tubes were used, 7.5 μL ferrofluid suspension was added per 1mL blood, and the flow rate was 10 mL/hour. The results are shown in Table 4.3. Comparable results were obtained for cases with both the smaller (~10) and larger numbers (>1,000) of cells.

	Ctrl 1	Ctrl 2	Ctrl average	Cells count	Capture rate
1	14	12	13.0	7	54%
2	52	45	48.5	37	76%
3	81	84	82.5	58	70%
4	164	150	157.0	160	102%
5	968	893	930.5	625	62%
6	1477	1496	1486.5	1129	76%

Table 4.3: Capture rates for different numbers of spiked cancer cells. [34]

In order to assess the number of cancer cells that were nonselectively trapped in the device, a blood sample of 2.5 mL was spiked with approximately 100,000 cells and

screened normally but without the permanent magnets. No cancer cells were captured by the experiment, which proves the high selectivity of our device.

To evaluate the capture efficiency of the developed screening system, we performed the spiked experiment for the capture rate.

We define the capture rates in the following way to evaluate the capture efficiency:

$$Capture\ rate\ (\%) = \frac{Number\ of\ cells\ found\ in\ the\ sample}{Average\ number\ of\ cells\ found\ in\ control\ slides} \times 100\% \quad (4.2)$$

Two control slides were prepared from the same cell suspension and at the same time as the blood sample was spiked. Similar capture rates were found regardless of how long (0–48 hours) the samples were kept following spiking. This result shows promise for future clinical applications. With slower flow rates, many of the cells tend to be trapped with aggregations of nanoparticles on the channel substrate. Sometimes, weakly CK+ cells were found behind a particle aggregation but did not satisfy either the observer's or the computer's criteria to be counted as a cancer cell, resulting in relatively low capture rates. With a smaller amount of added particle suspension (18.8 μL per 1mL of pre-processed blood) and faster flow rate, cells were spread in larger areas and easier to observe, which made the optimal condition for the higher average capture rates of 90%.

SK-BR-3 (breast cancer line), COLO 205 (colorectal cancer line), and PC3 (prostate cancer line) cell lines were used for spiked experiments to calculate the capture efficiency of the screening system with glass coverslip substrate. The experimental results are summarized in Table 4.4. The screening experiment spiked with PC3 cells also demonstrated a comparable result with a capture rate of 88%.

Cell	Tube	Ferrofluid/blood (µL/mL)	Flow rate (mL/hr)	Ctrl 1	Ctrl 2	Ctrl average (A)	Cell found (C)	Capture rate (C/A)	Average capture rate
COLO 205	EDTA	30	2.5	75	46	60.5	61	108	79%
	EDTA	30	2.5	115	114	114.5	92	80	
	EDTA	30	2.5	139	130	134.5	92	68	
	CellSave	30	2.5	75	46	60.5	40	66	65%
	CellSave	30	2.5	139	130	134.5	70	52	
	CellSave	30	2.5	48	53	50.5	49	96	
	CellSave	7.5	2.5	109	126	117.5	125	106	53%
	CellSave	7.5	2.5	180	193	186.5	83	28	
	CellSave	7.5	2.5	180	193	186.5	53	44	
	CellSave	7.5	10	252	275	263.5	239	91	90%
	CellSave	7.5	10	252	275	263.5	257	98	
	CellSave	7.5	10	252	275	263.5	267	101	
	CellSave	7.5	10	252	275	263.5	228	87	
	CellSave	7.5	10	252	275	263.5	240	91	
	CellSave	7.5	10	252	275	263.5	203	77	
SK-BR-3	CellSave	7.5	10	711	927	819.0	713	87	86%
	CellSave	7.5	10	711	927	819.0	704	86	

Table 4.4: Capture rates of spiked blood sample experiments. [34]

Table 4.5 shows the results of the spiked screening experiments of COLO 205, PC3, and SK-BR-3 cells for glass coverslip substrate with the introduction of a spacer placed between the permanent magnets and glass coverslip substrate. Using the screening system for the spiked experiments, the average capture rates for SK-BR-3, MCF-7, PC3, and COLO 205 cells were 90%, 100%, 99%, and 98%, respectively. Capture rate could be more than 100% when the number of cells added to the spiked sample is more than the

number of cells prepared for the control samples due to concentration variations in small sampling aliquots.

Cell	Ferrofluid/blood (μL/mL)	Flow rate (mL/hr)	Ctrl 1	Ctrl 2	Ctrl average (A)	Cell found (C)	Capture rate (C/A)	Average capture rate
SK-BR-3	7.5	2.5	568	671	619.5	598	97%	97%
PC3	7.5	2.5	50	21	35.5	38	107%	107%
COLO 205	7.5	2.5	86	95	90.5	99	109%	94%
	7.5	2.5	89	72	80.5	117	145%	
	7.5	2.5	89	72	80.5	111	138%	
	7.5	2.5	114	119	116.5	89	76%	
	7.5	2.5	86	83	84.5	80	95%	
	7.5	2.5	86	83	84.5	83	98%	
	7.5	2.5	109	137	123	116	97%	
	7.5	2.5	130	127	130	23	51%	
	7.5	2.5	216	215	220	191	87%	
	7.5	2.5	275	N/A	275	208	76%	
	7.5	2.5	211	168	190	182	96%	
	7.5	2.5	72	68	70	60	86%	
	7.5	2.5	126	116	121	114	94%	
	7.5	2.5	121	107	114	82	72%	
	7.5	2.5	112	115	114	105	92%	

Table 4.5: Capture rates of spiked blood sample experiments.

To evaluate the capture efficiency of the developed micromagnet-patterned glass slide substrate screening system, we used COLO 205 (colorectal cell line), PC3 (prostate cell line), SK-BR-3 (breast cancer cell line), and MCF-7 (breast cancer cell line) for the spiked experiments. We ran experiments using micromagnet-patterned glass slides and plain glass slides in parallel for comparisons. Both capture rates and CTC capture distribution patterns were investigated. We located those captured cancer cells on the

channel substrate for the comparison. Both capture rates and CTC capture distribution patterns were investigated.

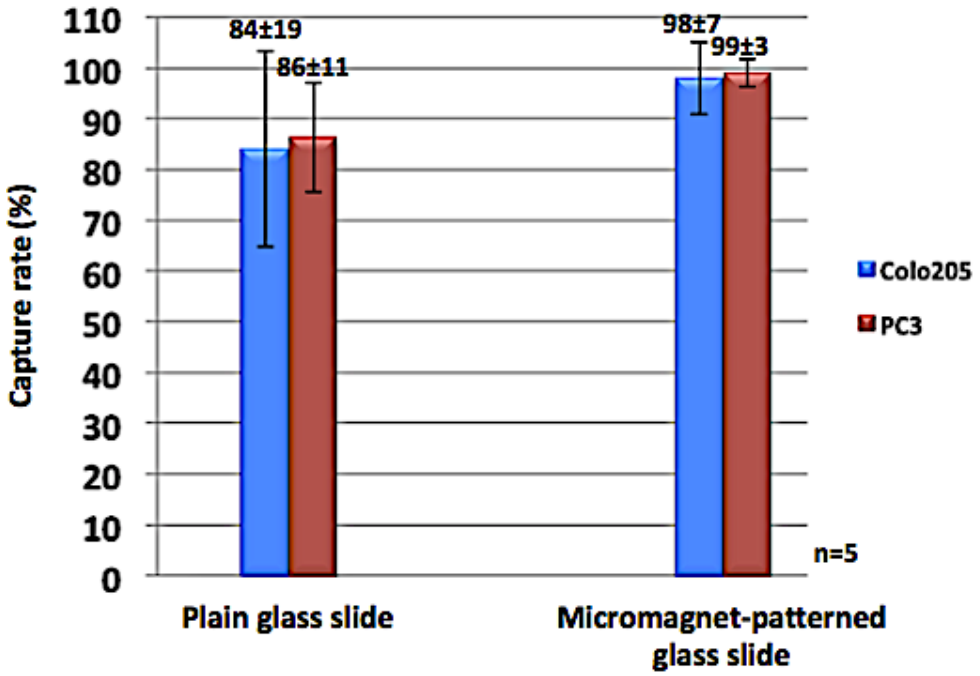

Figure 4.3: Capture rates of COLO 205 and PC3 spiked experiments. Both plain glass slide and micromagnet-patterned glass slide showed high capture rates for COLO 205 and PC3 cell lines. The capture rate of micromagnet-patterned glass slide is 16% higher than the capture rate of plain glass slide.

According to the experimental data in Figure 4.3, the capture rate for COLO 205-spiked experiments of microchannel without micromagnets (plain glass slide) was 84±19%, and the micromagnet-patterned glass slide yielded a capture rate of 98±7%. For PC3-spiked experiments, microchannel without micromagnets (plain glass slide) was 86±11%, and the micromagnet-patterned glass slide yielded a capture rate of 99±3%. The patterning of micromagnets on the channel substrate significantly improved the capture rate for 16% on average. In addition, the smaller capture rate variations indicated improved working stability of the micromagnets system (COLO 205: 19% vs. 7%, and

PC3: 11% vs. 3%). We believe that the improvement would be more distinct with a cell line that has a lower EpCAM surface expression, such as a PC3 cell line.

We also performed the spiked experiments for SK-BR-3 and MCF-7 cell lines. Figure 4.4 shows the experimental results of the spiked screening for SK-BR-3 and MCF-7 with micromagnet-patterned glass slide. For SK-BR-3-spiked experiments, microchannel without micromagnets (plain glass slide) was 90±9%, and the micromagnet-patterned glass slide yielded a capture rate of 100±5%.

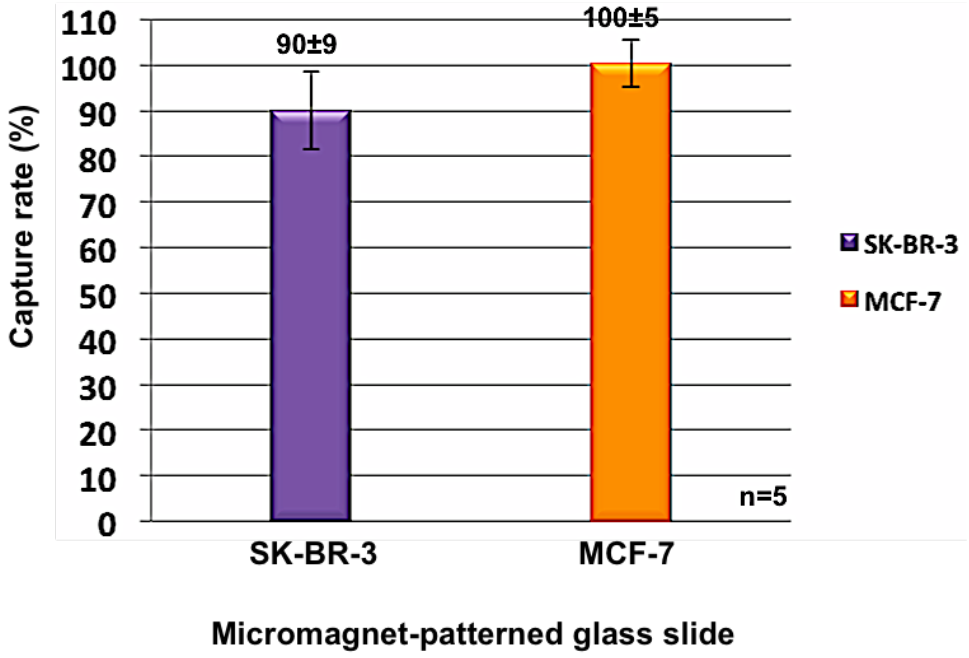

Figure 4.4: Capture rates of SK-BR-3 and MCF-7 spiked experiments. Both plain glass slide and micromagnet-patterned glass slide showed high capture rates for SK-BR-3 and MCF-7 cell lines. Capture rate of micromagnet-patterned glass slide is 18% higher than the capture rate of plain glass slide.

Figure 4.5 shows the distribution of the captured CTCs on the glass slides with and without micromagnet patterns, where all the cells captured by the micromagnets are represented as purple dots, cells captured by an aggregated nanoparticle line are represented as blue dots, and other captured cells are represented as orange dots. The

position of each cell can be accurately located using the integrated coordinate system on the glass slide. For the plain glass slide, most cells were captured around the edges of the permanent magnets. In contrast, the cells captured on the micromagnet glass slides were more scattered than those on the plain glass slide, especially in the front part of the channel.

The aggregation of target cells and excessive free nanoparticles on the substrate have been issues associated with the immunomagnetic assay, which usually weakens the systems by quenching fluorescence signals and burying or even damaging the captured target cells. The patterned thin-film micromagnet system provides an effective way to alleviate the aggregation issues.

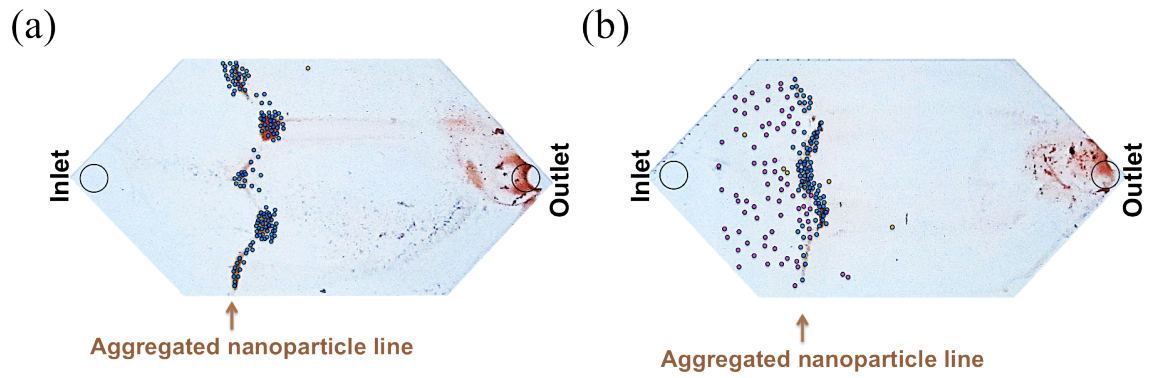

Figure 4.5: Experimental results of spiked COLO 205 cells using plain glass slide and micromagnet glass slide for comparison. (a) Distribution of COLO 205 cells on the plain glass slide. (b) Distribution of COLO 205 cells on the micromagnet-patterned glass slide.

Figure 4.6 shows the experimental results of the cell distribution histogram. The micromagnets increased the efficiency of the channel space usage for capture by about 13% (plain glass slide: 8%, micromagnet slide: 21%). In addition, micromagnets patterned on the glass slide significantly scattered the cells captured on the glass slide.

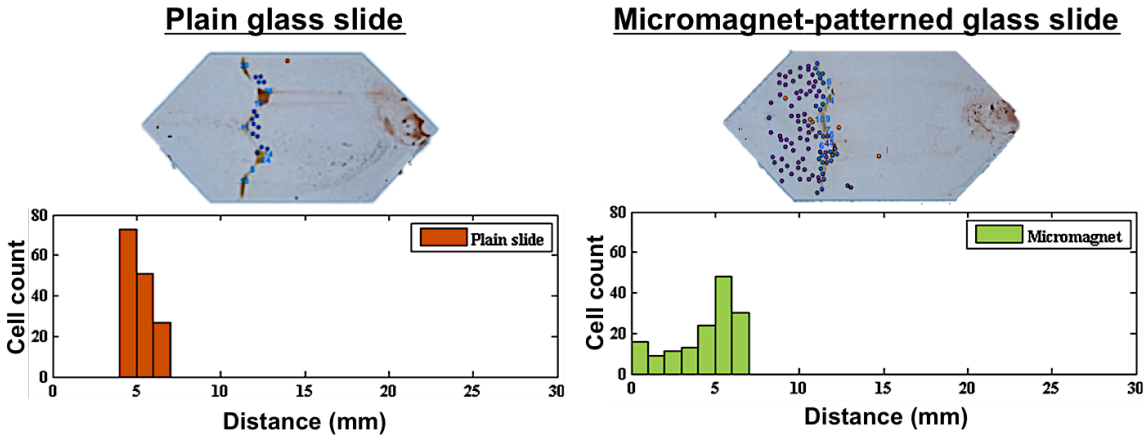

Figure 4.6: Distribution of cells and nanoparticles on the plain glass slide and micromagnet glass slide are compared. Histogram shows the distribution of the captured cancer cells along the microchannel substrate. Distance is defined as the range between the inlet port and the capture point of the cell.

We also categorized those captured cells into three parts, which are cells captured by micromagnets [Figure 3.6(b–d)], aggregated nanoparticles line [Figure 3.6(a)], and other areas, for the comparison of plain glass slides and micromagnet glass slides.

Figure 4.7 shows the percentages of each category for the plain glass slide and micromagnet glass slide. For the plain glass slide, most COLO 205 cells (90% of spiked cells) were captured along the nanoparticle-aggregated line. About 60% of spiked COLO205 cells were captured by patterned micromagnets on the glass slide, while only 35% of cells were captured along the nanoparticle-aggregated line. With the design and fabrication of micromagnets, the percentage of spiked cells captured on the nanoparticle-aggregated line was reduced by 55% (from 90% to 35%) to avoid the possible damage of captured cells caused by stacked free nanoparticles.

Free nanoparticles tend to aggregate on the strong magnetic field gradient that occurs at the edges of permanent magnets. The aggregated free nanoparticles may damage the captured cells or interfere with the identification of stained cells. To prove

that the array of patterned micromagnets is capable of scattering the free nanoparticles and cells throughout the microchannel, we measured the fluorescence intensity of stained cells captured on the plain glass slide and the micromagnet glass slide.

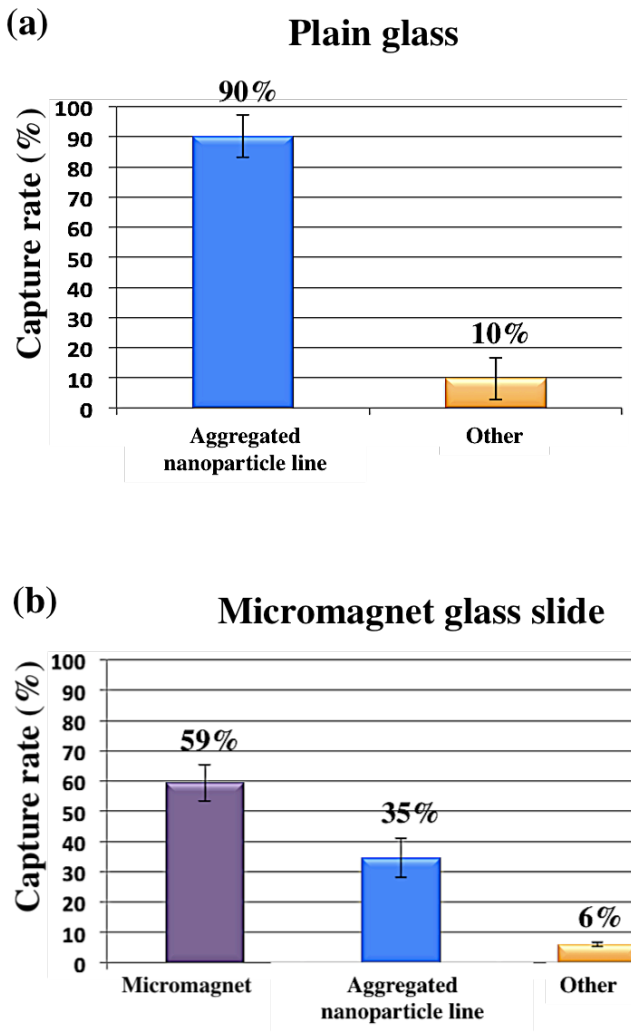

Figure 4.7: Spiked COLO 205 cells captured by aggregated line, micromagnets, or other areas. (a) Most cells (90% of spiked COLO 205 cells) were captured on the nanoparticle-aggregated line on the plain glass slide. (b) Many cells (59% of spiked COLO 205 cells) were captured by patterned micromagnets. Only 35% of spiked COLO 205 cells were captured on the nanoparticle-aggregated line on the micromagnet glass slide compared to 90% of spiked COLO 205 cells that were captured on the nanoparticle-aggregated line on the plain glass slide.

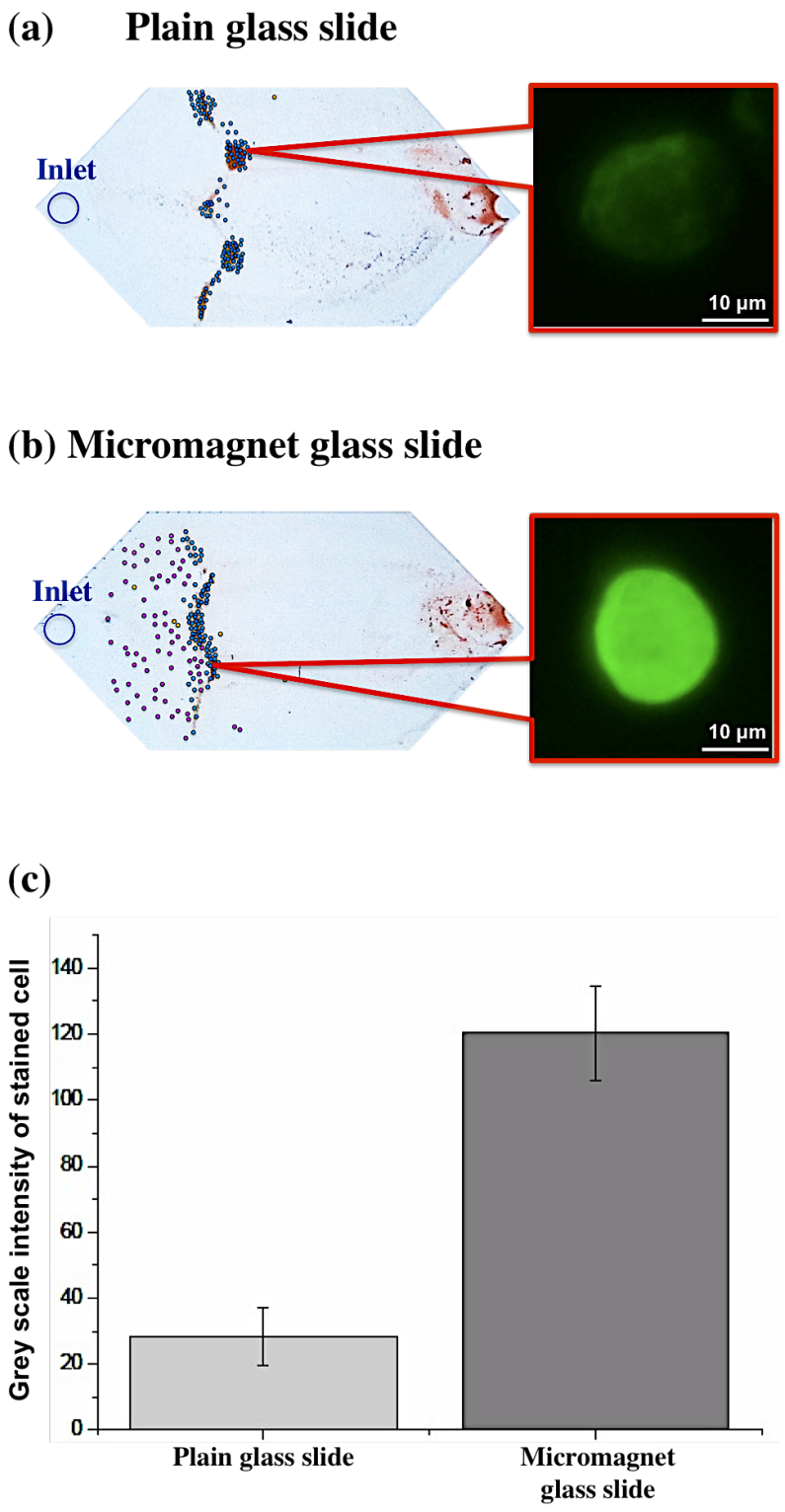

Figure 4.8: (a) Fluorescence image of a cancer cell captured on a plain glass slide. (b) Fluorescence image of a cancer cell captured on a micromagnet glass slide. (c) Grayscale intensity of stained cells.

Figure 4.8(a) shows the mapping of cancer cells captured on the plain glass slide, the fluorescence image of a stained cancer cell located on the nanoparticles-aggregated area. Figure 4.8(b) shows the same information for cancer cells captured on micromagnet glass slide. Figure 4.8(c) shows the grayscale intensity of stained cells. The intensity of the cell captured on the plain glass slide is four times greater than that of the cell on the micromagnet glass slide. Therefore, patterned micromagnets significantly reduce the possibility of miscounting the cell during the identification process.

4.2 PATIENT SAMPLE SCREENING

The developed screening system (glass coverslip with a spacer placed close to the inlet) was applied to the clinical study of isolating CTCs from patient samples. CTCs were successfully isolated from patients' blood samples with a variety of types of cancer.

4.2.1 Specificity

Combining the benefits of immunofluorescence staining and anti-EpCAM coated nanoparticle labeling the target CTCs, the system shows high specificity for the clinical screening of patient samples.

Figure 4.9 shows immunofluorescence images of captured CTCs separated from clinical samples. Figure 4.9(a) shows a single CTC found from two patient samples. In addition, we were able to find clusters of CTCs in clinical samples [Figure 4.9 (b)]. Clusters of CTCs could detach from the proliferation of intravascular cancer cells [132]. A cluster of 50 CTCs was captured from patient sample number 2, a blood sample from a female subject with breast cancer disease. More than a thousand CTCs were found from the patient sample number 9 [Figure 4.9(c)], who had stage 4 lung cancer. Unlike spiked cancer cells, CTCs separated from clinical samples vary in size, shape, and CK expression level. Cancer cells in Figure 4.9(c) also show a lower level of CK compared to

the higher CK level of spiked cancer cells. Cultured cancer cell lines such as PC3, SK-BR-3, and COLO 205 that are commonly used for spiked screening experiments express more EpCAM or cytokeratin than CTCs from clinical samples since some CTCs are believed to undergo epithelial-mesenchymal transition (EMT) while circulating in the bloodstream [133, 134].

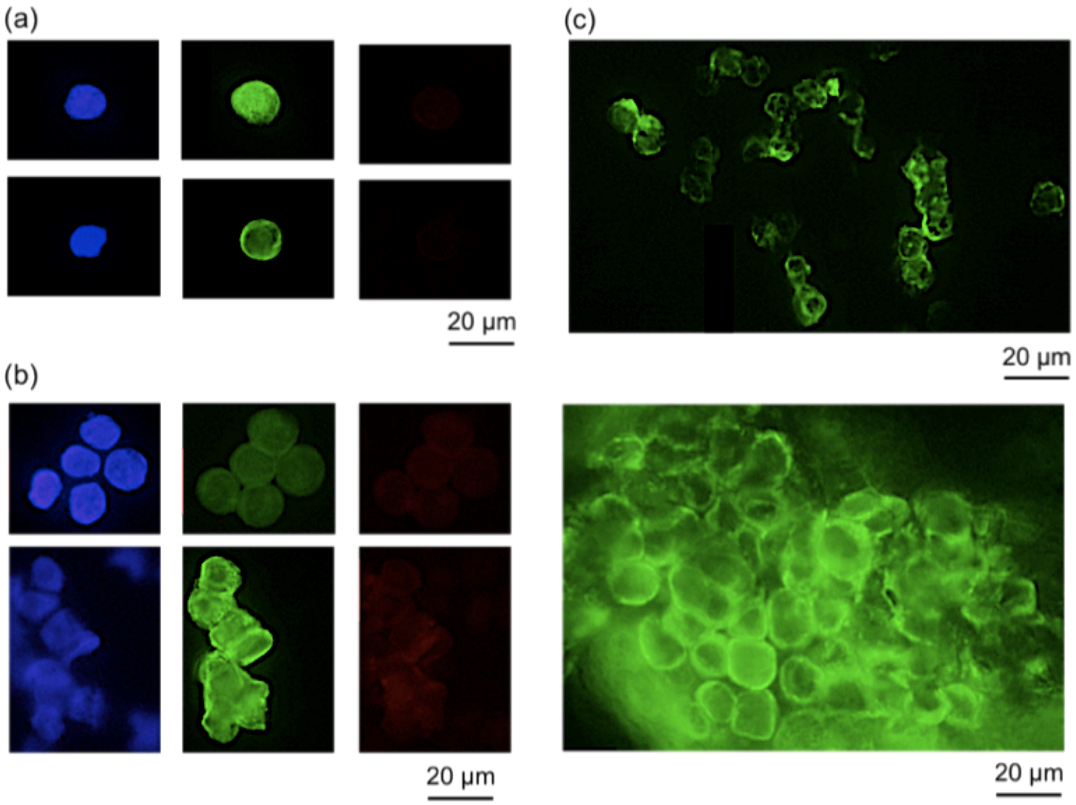

Figure 4.9: Fluorescence images of captured CTCs from patient samples. (a) Singlet CTCs isolated from patient samples. (b) Clusters of CTCs separated from patient samples. (c) Clusters of CTCs from a patient sample. [35]

After demonstrating high capture efficiency of the micromagnet-patterned glass slide for the screening system, we applied the system for the clinical screening. Figure 4.10 shows that a single CTC or one doublet from patients' whole blood samples were captured by patterned micromagnets.

In the plain glass slide substrate, we found clusters of CTCs from patient samples. However, no cluster of CTCs was found from patient samples on the micromagnet-patterned glass slide. Most CTCs found from patient samples were singlet or doublet cells. The array of micromagnets may scatter the clusters of CTCs on the channel substrate.

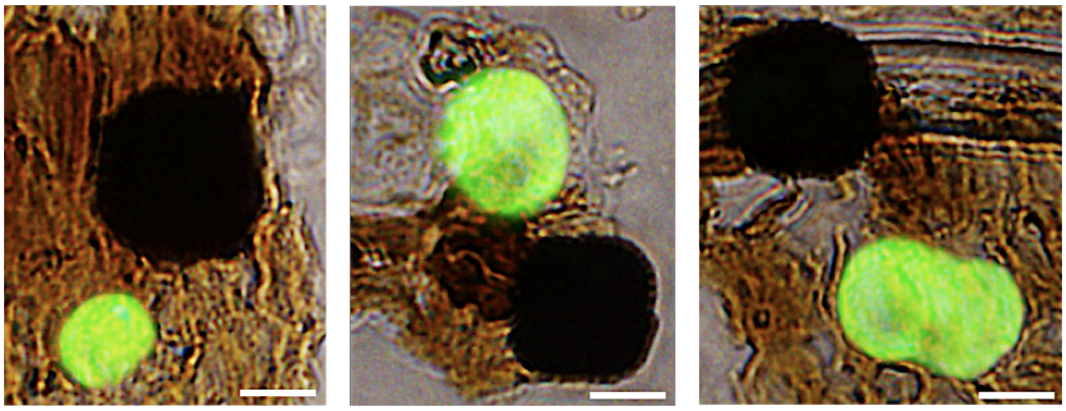

Figure 4.10: Overlay of fluorescence image and bright field image of a single CTC or two CTCs from patient blood samples captured by micromagnets. Scale bar is 10 μm.

4.2.2 Sensitivity

Table 4.6 shows the numbers of CTCs found from screened subject samples in which CTCs were captured by the glass coverslip microchip with a spacer placed close to the inlet of the microchannel. Samples number 1 and 2 were screened with the commercial CellSearch® screening system in parallel with our microchip-based screening system for evaluation. Our system had capture rates comparable with those of the CellSearch® system. In addition, the developed microchip-based system can detect as low as one single CTC from the 5 mL of whole blood-sample, evidence of its high sensitivity.

The results of the screened clinical samples of breast and prostate patient blood samples by the micromagnet-patterned glass slide are also shown in Table 4.7. It also demonstrates high sensitivity.

Sample number	Ferrofluid/blood (μL/mL)	Flow rate (mL/hr)	Screening volume (mL)	Numbers of CTCs	Gender	Cancer type	Numbers of CTCs/7.5 mL (Microchip)	Numbers of CTCs/7.5 mL (CellSearch®)
1	7.5	2.5	5	30	F	Breast	20	16
2	7.5	2.5	10	50	F	Breast	33	10
3	7.5	2.5	5	1	M	Prostate	0.6	3
4	7.5	2.5	5	1	F	Lung	0.6	N/A
5	7.5	2.5	5	1	F	Lung	0.6	N/A
6	7.5	2.5	7.5	5	F	Breast	3	N/A
7	7.5	2.5	5	19	F	Breast	13	N/A
8	7.5	2.5	5	28	F	Lung	19	N/A
9	7.5	2.5	5	>1000	F	Breast	> 666	N/A
10	7.5	2.5	7.5	1	F	Breast	0.6	N/A
11	7.5	2.5	7.5	1	F	Breast	0.6	N/A

Table 4.6: Summary of screened patient samples and CTC counts of blood samples from cancer patients with glass coverslip with a spacer (pathology information included)

Sample number	Ferrofluid/blood (μL/mL)	Flow rate (mL/hr)	Screening volume (mL)	Numbers of CTCs	Gender	Cancer type	Numbers of CTCs/7.5 mL (Microchip)
1	7.5	2.5	7.5	2	F	Breast	2
2	7.5	2.5	7.5	1	F	Breast	1
3	7.5	2.5	10	22	F	Breast	17
4	7.5	2.5	5.0	215	F	Breast	323
5	7.5	2.5	7.5	2	F	Breast	2
6	7.5	2.5	7.5	6	F	Breast	6
7	7.5	2.5	5.0	10	F	Breast	15
8	7.5	2.5	7.5	13	M	Prostate	13
9	7.5	2.5	7.5	7	M	Prostate	7
10	7.5	2.5	12.5	7	M	Prostate	4
11	7.5	2.5	7.5	3	F	Breast	3
12	7.5	2.5	7.5	6	F	Breast	6

Table 4.7: Results of screened patient samples with micromagnets patterned on the glass slide (pathology information included).

4.3 FLUORESCENCE IN-SITU HYBRIDIZATION RESULTS

The fluorescence *in-situ* hybridization method was used to study the copy numbers of HER-2/neu and CEP17 and ratio number for breast cancer cell lines, including SK-BR-3 and MDA-MB-231. The experimental results of SK-BR-3 and MDA-MB-231 are shown in Figure 4.11 and Figure 4.12.

Figure 4.11 shows the experimental results of SK-BR-3 cells (breast cancer cell lines) by the fluorescence in-situ hybridization method. Hybridization signals for HER-2/neu and CEP17 are shown in Figure 4.11. For SK-BR-3, Figure 4.11(a) shows twenty copies of HER-2/neu, while four copies of CEP17 were found. In Figure 4.11(b), thirty copies of HER-2/neu and six copies of CEP17 were shown. SK-BR-3 cell shows a high level of HER-2 amplification.

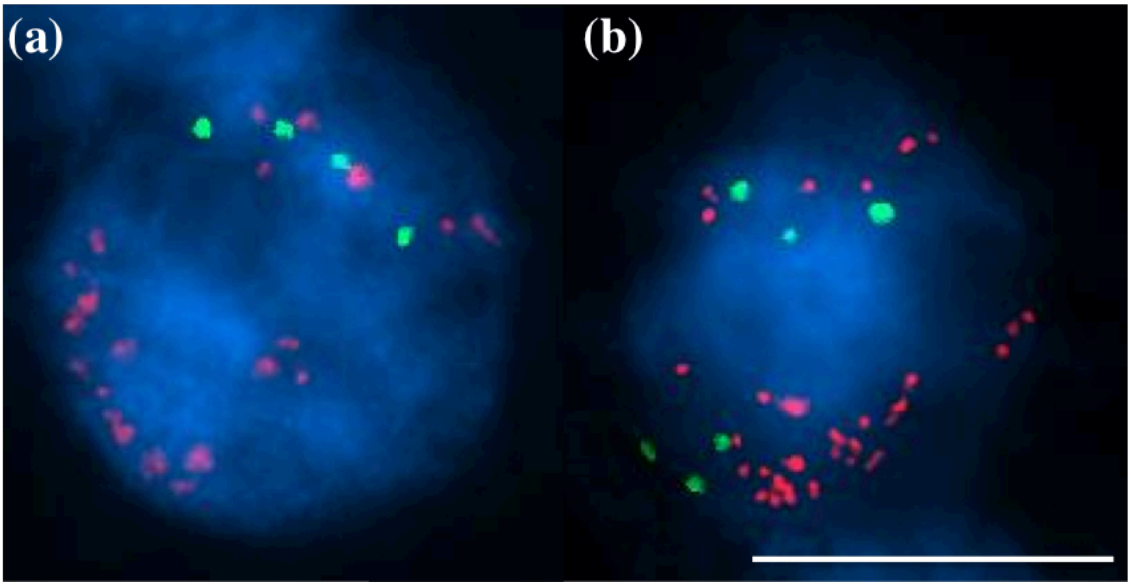

Figure 4.11: Results of fluorescence *in-situ* hybridization (FISH). Spiked cancer cell line, which was SK-BR-3, shows clear hybridization signals for HER-2/neu in orange and CEP17 in green. (a) SK-BR-3 cells show 20 copies of HER-2/neu and 4 copies of CEP17. (b) The general pattern found for SK-BR-3 cells presents 6 signals for CEP17 and 30 copies for HER-2. Scale bar is 10 mm.

Figure 4.12 shows hybridization signals for HER-2/neu and CEP17 in three MDA-MB-231 cells. The inset of Figure 4.12 shows the experimental result of the FISH method of a leukocyte used as a control cell as a normal cell sample. All three MDA-MB-231 cells show three copies of HER-neu and CEP17.

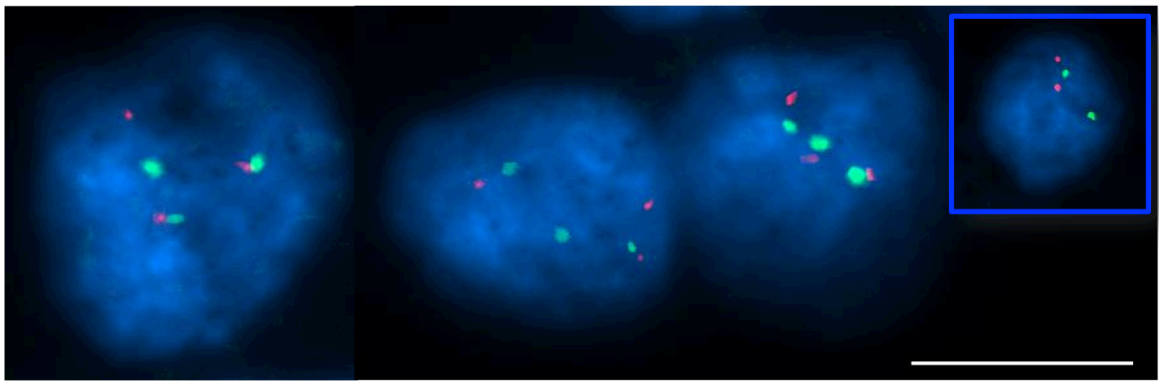

Figure 4.12: Results of the FISH method. Leukocyte was used as a positive control for the FISH analysis. Spiked cancer cell lines, which are MDA-MB-231, show clear hybridization signals for HER-2 in orange and CEP17 in green. All three MDA-MB-231 cells show three copies of HER-2 and three copies of the CEP17. Scale bar is 10 μm.

Table 4.8 shows the results of the quantitative information of the copy number of fluorescence signals found in all spiked breast cell lines (SK-BR-3 and MCA-MB-231). The spiked SK-BR-3 cell presents four copies of CEP17 in Figure 4.11(a) and six copies of CEP17 in Figure 4.11(b) but twenty copies of HER-2 [Figure 4.11(a)] and thirty copies of CEP17 [Figure 4.11(b)]. MDA-MB-231 cell line does not show HER-2 amplifications (the ratio of HER-2 with respect to CEP17 is one, as shown in Table 4.8). The SK-BR-3 cell line shows amplification of HER-2 with lots of HER-2 copies, as shown in Figure 4.11. The average copy number for HER-2 was five. Gene amplification for HER-2, which was five times larger than CEP17, was found.

Cell line	HER-2/neu copy number	CEP copy number	Ratio of HER-2 to CEP17
Leukocyte	3	3	1
SK-BR-3	27	5	5.4
MDA-MB-231	3	3	1

Table 4.8: Absolute and relative copy numbers of spiked HER-2 and CEP17 for SK-BR-3 and MDA-MB-231 cell lines.

For CTCs captured from breast cancer patients, the FISH method was used to study the gene expression of CTCs. Figure 4.13 shows the results of the FISH analysis. CTCs captured from breast cancer patients show clear hybridization signals for HER-2 in orange and CEP17 in green. Figure 4.12 (a) shows HER-2 amplification and ratio number to be 2.5 of a CTC from the patient 1 shows. In Figure 4.12 (b), a CTC captured from the patient number 2 shows ratio number to be two. For the patient number 2, a CTC shows significant high amplification of HER-2, as shown in Figure 4.12 (c). The ratio number was measured to be five.

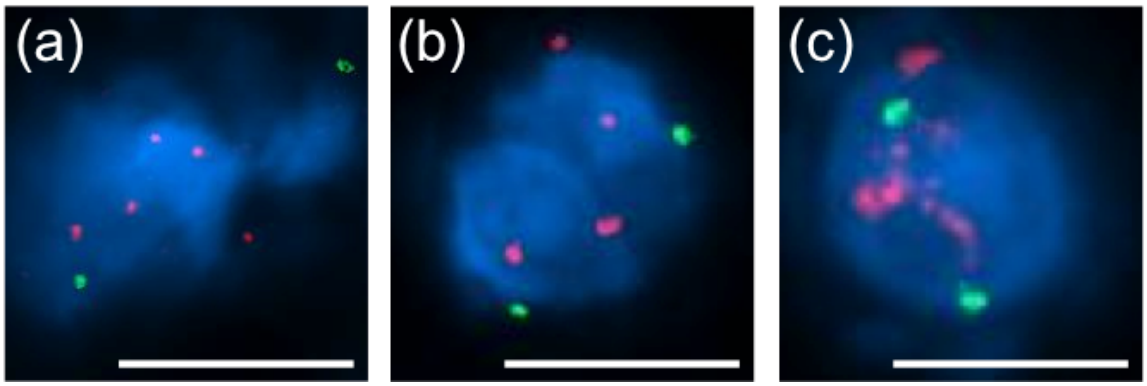

Figure 4.13: Results of the FISH method. CTCs captured from breast cancer patients show clear hybridization signals for HER-2 in orange and CEP17 in green. Scale bar is 10 mm.

4.4 SUMMARY

We discussed the gravity effect of RBCs in the microchannel on the cell separation in the microchannel. Next, we proved that the capture efficiency of the inverted microchannel is higher than the upright microchannel by the spiked experiments. Furthermore, spiked experiments demonstrate high capture efficiencies of the developed screening system for different cancer cell lines. Integration of micromagnets on the channel substrate presents both the high capture efficiency and stability (>90% capture efficiency for all spiked cell lines). The patterned micromagnets are capable of scattering the free particles and target cancer cells. In addition, the system has been successfully applied for clinical screening of patient samples to show high sensitivity and specificity. FISH analysis was also used to molecularly characterize the CTCs separated from patient samples.

Chapter 5

Conclusion and Future work

5.1 CONCLUSION

The developed screening system combines the power of immunomagnetic assay and microfluidic device to show the capability of isolating rare CTCs from blood samples with high capture efficiency, high sensitivity, high throughput, low cost, and easy fabrication.

We designed and developed a microchip-based immunomagnetic screening system with a computer-controlled rotational arm holding an array of up to six microchips in parallel for the high throughput screening. The system is operated in a flip-flop mode. Through the computer-controlled interface, the screening microchip can be placed in any position, such as an upright position and inverted position, during the screening process.

We also have demonstrated both theoretically and experimentally that the sedimentation of red blood cells with regard to the magnetic force acting on the nanoparticle-tagged cancer cells required for the cell separation is critical for capture efficiency, throughput, and purity. By precisely controlling the microchip position during the screening process, we can reduce the stagnation of red blood cells and non-specific bonding on the channel substrate by alternating the direction of magnetic force with respect to the gravity force on the target cells and determining the direction of red blood cell sedimentation.

We demonstrated that the amount of the nanoparticle suspension used for the screening was significantly reduced to 25% of the amount used in the commercially available and the only FDA-approved screening system (CellSearch®) because of the

microchip-based screening system and stronger magnetic force's acting on the nanoparticle-labeled tumor cells.

We demonstrated that the screening system has been used to isolate and detect multiple cancer cell lines, including breast cancer (SK-BR-3, MCF-7, and MDA-MB-231), colorectal cancer (COLO 205), and prostate cancer (PC3), to achieve high capture efficiency (97% in average) in the spiked screening experiments. Furthermore, the system has been successfully applied for the screening and isolation of CTCs from clinical blood samples, including metastatic breast, colorectal, prostate, and lung cancer patient samples.

We then demonstrated the design, calculation, and fabrication of an array of micromagnets. The patterned micromagnets provide a locally enhanced magnetic field and modulate the magnetic field distribution throughout the whole channel surface. With the addition of micromagnets patterned on the plain channel substrate, we demonstrated the capability of enhancing the retaining magnetic force and reducing the cell aggregation by increasing the channel space occupancy for 13%. The array of micromagnets also largely increased the stability of achieving high capture efficiency (more than 95% capture rate with less variation for all three different cell lines).

In the end, we used the fluorescence *in-situ* hybridization (FISH) method to study the genetic information of the CTCs captured by the screening system we developed. We measured the ratio of the copy number of HER-2 to chromosome 17 (CEP17) of SK-BR-3, comparing to the ratio number of MDA-MB-231. HER-2/neu was highly amplified in SK-BR-3 (HER-2 positive cell line) comparing to MDA-MB-231 (HER-2 negative cell line) that copy number of HER-2 in SK-BR-3 was twenty five while copy number of HER-2 in MDA-MB-231 was three. For the ratio of HER-2 copy number to CEP17 copy number, SK-BR-3 (ratio was five) showed higher ratio than MDA-MB-231 (ratio was one).

We have applied the developed screening system for the clinical screening. Over 40 patients have been successfully screened. CTCs captured from patient samples were observed and identified by the immunofluorescence staining method. Other than immunofluorescence staining technique, the FISH method was performed to study the HER-2 and CEP17 expression of the CTCs captured from breast cancer patients that CTCs showed amplification of HER-2/neu and ratio number of HER-2/CEP17 to be higher than 2.2.

The developed immunomagnetic microchip-based screening system provides a new clinical tool that could dramatically improve recognition and monitoring of cancer.

5.2 FUTURE WORK

In addition to the rarity nature of CTCs in blood sample, heterogeneity of CTCs is a challenge for the cell detection. Several techniques, such as the reverse transcription polymerase chain reaction (RT-PCR) method [135], the fluorescence *in-situ* hybridization (FISH) method [14], and immunohistochemistry (IHC) method [136], have been proposed to molecularly characterize the CTCs. Molecular characterization provide important information for molecularly targeted therapies and assessment of the treatment effect. For instance, trastuzumab (Herceptin®) is commonly used as adjuvant therapy for HER-2 positive breast cancer. For colorectal cancer, FOLFOX is often used therapy with bevacizumab, which is incorporated with chemotherapy [137, 138]. In order to accurately and efficiently assess the treatment efficacy, separation of CTCs followed by downstream analysis is important for cancer. Moreover, single cell profiling of CTCs provides an alternative to the CTC heterogeneity study for drug discovery of cancer [45]. Analyzing CTCs' genomic and transcriptomic profile is critical for studying tumor biology.

Multiplexed assay with versatile antibodies is required for rare CTCs detection due to tumor heterogeneity and epithelial–to mesenchymal transition (EMT) that some

metastatic cancer cells may express low level of EpCAM [139-141]. Therefore, hybrid magnetic nano-carrier conjugated with multiple antibodies specific for common biomarkers, such as epithelial cell adhesion molecule (EpCAM), human epidermal growth factor receptor 2 (HER-2), epidermal growth factor receptor (EGFR), cluster of differentiation 146 (CD146), and mucin 1 (MUC1) expressed on different cancer cells is necessary for cancer cell detection [41]. With a combination of versatile immunomagnetic nanocarrier conjugated with antibodies, coating of multiple antibodies on separate areas of the channel substrate, and multiplexed staining of cancer cells, can enhance the capability of detection of heterogenetic CTCs.

Increasing efforts have been devoted in the detection of disseminated tumor cells (DTCs) from the bone marrow (BM) recently [142]. Besides, circulating tumor cells (CTCs) in peripheral blood, DTC is also considered as a surrogate marker for minimal residual disease in breast cancer [143]. A cancer stem cell theory states that a tumor grows and forms at a secondary tumor site can be caused by a small subpopulation of cancer cells, which are cancer stem cells/DTCs [144]. For the biomarker expression, most DTCs in BM are CD44 positive [145]. Therefore, detection of DTCs can be a potential application for the developed immunomagnetic microchip-based screening system.

References

[1] http://www.businesswire.com/news/home/20110609006160/en/Report-Cancer-Diagnostics-Market-Grow-776-mn. (2011). *Report: Cancer Diagnostics Market to Grow from $776 mn to $5.3 bn: companiesandmarkets.com*.

[2] N. C. Institute, "Metastatic Cancer," 03/28/2013 2013.

[3] S. Paget, "THE DISTRIBUTION OF SECONDARY GROWTHS IN CANCER OF THE BREAST," *The Lancet,* vol. 133, pp. 571-573, 1889.

[4] D. Ribatti, "Stephen Paget and the "Seed and Soil" Theory of Metastatic Dissemination," in *Protagonists of Medicine*, ed: Springer Netherlands, 2010, pp. 65-71.

[5] K. Hida, N. Ohga, T. Kurosu, Y. Totsuka, and M. Shindoh, "Crosstalk between Blood Vessels and Tumor Microenvironment," *Oral Science International,* vol. 7, pp. 1-10, 2009.

[6] D. Ribatti, G. Mangialardi, and A. Vacca, "Stephen Paget and the 'seed and soil'theory of metastatic dissemination," *Clinical and experimental medicine,* vol. 6, pp. 145-149, 2006.

[7] L. A. Mina and G. W. Sledge, "Rethinking the metastatic cascade as a therapeutic target," *Nature Reviews Clinical Oncology,* vol. 8, pp. 325-332, 2011.

[8] P. Mehlen and A. Puisieux, "Metastasis: a question of life or death," *Nature Reviews Cancer,* vol. 6, pp. 449-458, 2006.

[9] H. Abts, M. Emmerich, S. Miltenyi, A. Radbruch, and H. Tesch, "CD20 positive human B lymphocytes separated with the magnetic cell sorter (MACS) can be induced to proliferation and antibody secretion in vitro," *Journal of Immunological Methods,* vol. 125, pp. 19-28, 12/20/ 1989.

[10] S. Mocellin, U. Keilholz, C. R. Rossi, and D. Nitti, "Circulating tumor cells: the 'leukemic phase'of solid cancers," *Trends in molecular medicine,* vol. 12, pp. 130-139, 2006.

[11] P. Paterlini-Brechot and N. L. Benali, "Circulating tumor cells (CTC) detection: Clinical impact and future directions," *Cancer Letters,* vol. 253, pp. 180-204, 8/18/ 2007.

[12] B. Mostert, S. Sleijfer, J. A. Foekens, and J. W. Gratama, "Circulating tumor cells (CTCs): detection methods and their clinical relevance in breast cancer," *Cancer treatment reviews,* vol. 35, pp. 463-474, 2009.

[13] W. Kemmner, "Currently Used Markers for CTC Isolation-Advantages, Limitations and Impact on Cancer Prognosis," *Journal of Clinical & Experimental Pathology,* 2011.

[14] S. Meng, D. Tripathy, S. Shete, R. Ashfaq, H. Saboorian, B. Haley, *et al.*, "uPAR and HER-2 gene status in individual breast cancer cells from blood and tissues," *Proceedings of the National Academy of Sciences,* vol. 103, pp. 17361-17365, 2006.

[15] J. E. Joy, E. E. Penhoet, and D. B. Petitti, *Saving women's lives: strategies for improving breast cancer detection and diagnosis*: National Academies Press, 2005.

[16] S. J. Dotan E Fau - Cohen, K. R. Cohen Sj Fau - Alpaugh, N. J. Alpaugh Kr Fau - Meropol, and N. J. Meropol, "Circulating tumor cells: evolving evidence and future challenges," 20091130 DCOM- 20100202.

[17] D. M. Kavanagh, M. Kersaudy-Kerhoas, R. S. Dhariwal, and M. P. Y. Desmulliez, "Current and emerging techniques of fetal cell separation from maternal blood," *Journal of Chromatography B,* vol. 878, pp. 1905-1911, 7/15/ 2010.

[18] H. Mohamed, M. Murray, J. N. Turner, and M. Caggana, "Isolation of tumor cells using size and deformation," *Journal of Chromatography A,* vol. 1216, pp. 8289-8295, 11/20/ 2009.

[19] S. Tan, L. Yobas, G. Lee, C. Ong, and C. Lim, "Microdevice for the isolation and enumeration of cancer cells from blood," *Biomedical Microdevices,* vol. 11, pp. 883-892, 2009/08/01 2009.

[20] B. Xu T Fau - Lu, Y.-C. Lu B Fau - Tai, A. Tai Yc Fau - Goldkorn, and A. Goldkorn, "A cancer detection platform which measures telomerase activity from live circulating tumor cells captured on a microfilter," 20100816 DCOM-20101110.

[21] Z. Liu, F. Huang, J. Du, W. Shu, H. Feng, X. Xu, *et al*., "Rapid isolation of cancer cells using microfluidic deterministic lateral displacement structure," *Biomicrofluidics,* vol. 7, p. 011801, 2013.

[22] M. Hosokawa, T. Hayata, Y. Fukuda, A. Arakaki, T. Yoshino, T. Tanaka, *et al*., "Size-selective microcavity array for rapid and efficient detection of circulating tumor cells," *Analytical chemistry,* vol. 82, pp. 6629-6635, 2010.

[23] P. Chen, Y.-Y. Huang, K. Hoshino, and X. Zhang, "Multiscale immunomagnetic enrichment of circulating tumor cells: from tubes to microchips," *Lab on a Chip,* 2014.

[24] D. R. Gossett, W. M. Weaver, A. J. Mach, S. C. Hur, H. T. K. Tse, W. Lee, *et al*., "Label-free cell separation and sorting in microfluidic systems," *Analytical and bioanalytical chemistry,* vol. 397, pp. 3249-3267, 2010.

[25] S. C. Hur, A. J. Mach, and D. Di Carlo, "High-throughput size-based rare cell enrichment using microscale vortices," *Biomicrofluidics,* vol. 5, p. 022206, 2011.

[26] J. A. Davis, D. W. Inglis, K. J. Morton, D. A. Lawrence, L. R. Huang, S. Y. Chou, *et al*., "Deterministic hydrodynamics: taking blood apart," *Proceedings of the National Academy of Sciences,* vol. 103, pp. 14779-14784, 2006.

[27] W. Zhang, K. Kai, D. S. Choi, T. Iwamoto, Y. H. Nguyen, H. Wong, *et al*., "Microfluidics separation reveals the stem-cell–like deformability of tumor-initiating cells," *Proceedings of the National Academy of Sciences,* vol. 109, pp. 18707-18712, 2012.

[28] P. R. C. Gascoyne, J. Noshari, T. J. Anderson, and F. F. Becker, "Isolation of rare cells from cell mixtures by dielectrophoresis," *ELECTROPHORESIS,* vol. 30, pp. 1388-1398, 2009.

[29] M. Yu, S. Stott, M. Toner, S. Maheswaran, and D. A. Haber, "Circulating tumor cells: approaches to isolation and characterization," *The Journal of cell biology,* vol. 192, pp. 373-382, 2011.

[30] S. Nagrath, L. V. Sequist, S. Maheswaran, D. W. Bell, D. Irimia, L. Ulkus, *et al.*, "Isolation of rare circulating tumour cells in cancer patients by microchip technology," *Nature,* vol. 450, pp. 1235-1239, 2007.

[31] S. L. Stott, C.-H. Hsu, D. I. Tsukrov, M. Yu, D. T. Miyamoto, B. A. Waltman, *et al.*, "Isolation of circulating tumor cells using a microvortex-generating herringbone-chip," *Proceedings of the National Academy of Sciences,* vol. 107, pp. 18392-18397, 2010.

[32] W. Miltenyi S Fau - Muller, W. Muller W Fau - Weichel, A. Weichel W Fau - Radbruch, and A. Radbruch, "High gradient magnetic cell separation with MACS," 19900507 DCOM- 19900507.

[33] A. H. Talasaz, A. A. Powell, D. E. Huber, J. G. Berbee, K.-H. Roh, W. Yu, *et al.*, "Isolating highly enriched populations of circulating epithelial cells and other rare cells from blood using a magnetic sweeper device," *Proceedings of the National Academy of Sciences,* vol. 106, pp. 3970-3975, 2009.

[34] K. Hoshino, Y.-Y. Huang, N. Lane, M. Huebschman, J. W. Uhr, E. P. Frenkel, *et al.*, "Microchip-based immunomagnetic detection of circulating tumor cells," *Lab on a Chip,* vol. 11, pp. 3449-3457, 2011.

[35] Y.-y. Huang, K. Hoshino, P. Chen, C.-h. Wu, N. Lane, M. Huebschman, *et al.*, "Immunomagnetic nanoscreening of circulating tumor cells with a motion controlled microfluidic system," *Biomedical microdevices,* pp. 1-9, 2012.

[36] T.-H. Wu, Y. Chen, S.-Y. Park, J. Hong, T. Teslaa, J. F. Zhong, *et al.*, "Pulsed laser triggered high speed microfluidic fluorescence activated cell sorter," *Lab on a chip,* vol. 12, pp. 1378-1383, 2012.

[37] J. Krüger, K. Singh, A. O'Neill, C. Jackson, A. Morrison, and P. O'Brien, "Development of a microfluidic device for fluorescence activated cell sorting," *Journal of Micromechanics and Microengineering,* vol. 12, p. 486, 2002.

[38] A. Benez, A. Geiselhart, R. Handgretinger, U. Schiebel, and G. Fierlbeck, "Detection of circulating melanoma cells by immunomagnetic cell sorting," *Journal of Clinical Laboratory Analysis,* vol. 13, pp. 229-233, 1999.

[39] B. D. Plouffe, M. Mahalanabis, L. H. Lewis, C. M. Klapperich, and S. K. Murthy, "Clinically relevant microfluidic magnetophoretic isolation of rare-cell populations for diagnostic and therapeutic monitoring applications," *Analytical chemistry,* vol. 84, pp. 1336-1344, 2012.

[40] S. Kumar, J. Aaron, and K. Sokolov, "Directional conjugation of antibodies to nanoparticles for synthesis of multiplexed optical contrast agents with both delivery and targeting moieties," *Nature Protocols,* vol. 3, pp. 314-320, 2008.

[41] C.-H. Wu, Y.-Y. Huang, P. Chen, K. Hoshino, H. Liu, E. P. Frenkel, *et al.*, "Versatile Immunomagnetic Nanocarrier Platform for Capturing Cancer Cells," *ACS nano,* 2013.

[42] E. Ozkumur, A. M. Shah, J. C. Ciciliano, B. L. Emmink, D. T. Miyamoto, E. Brachtel, *et al.*, "Inertial Focusing for Tumor Antigen–Dependent and–Independent Sorting of Rare Circulating Tumor Cells," *Science translational medicine,* vol. 5, pp. 179ra47-179ra47, 2013.

[43] J. J. Chalmers, M. Zborowski, L. Sun, and L. Moore, "Flow through, immunomagnetic cell separation," *Biotechnology progress,* vol. 14, pp. 141-148, 1998.

[44] M. Zborowski and J. J. Chalmers, "Rare cell separation and analysis by magnetic sorting," *Analytical chemistry,* vol. 83, pp. 8050-8056, 2011.
[45] A. A. Powell, A. H. Talasaz, H. Zhang, M. A. Coram, A. Reddy, G. Deng, *et al.*, "Single cell profiling of circulating tumor cells: transcriptional heterogeneity and diversity from breast cancer cell lines," *PLoS One,* vol. 7, p. e33788, 2012.
[46] http://www.cellsearchctc.com/
[47] M. Balic, N. Dandachi, G. Hofmann, H. Samonigg, H. Loibner, A. Obwaller, *et al.*, "Comparison of two methods for enumerating circulating tumor cells in carcinoma patients," *Cytometry Part B: Clinical Cytometry,* vol. 68, pp. 25-30, 2005.
[48] M. C. Miller, G. V. Doyle, and L. W. M. M. Terstappen, "Significance of circulating tumor cells detected by the CellSearch system in patients with metastatic breast colorectal and prostate cancer," *Journal of oncology,* vol. 2010, 2009.
[49] S. Riethdorf, H. Fritsche, V. Müller, T. Rau, C. Schindlbeck, B. Rack, *et al.*, "Detection of circulating tumor cells in peripheral blood of patients with metastatic breast cancer: a validation study of the CellSearch system," *Clinical Cancer Research,* vol. 13, pp. 920-928, 2007.
[50] M. Cristofanilli, G. T. Budd, M. J. Ellis, A. Stopeck, J. Matera, M. C. Miller, *et al.*, "Circulating Tumor Cells, Disease Progression, and Survival in Metastatic Breast Cancer," *New England Journal of Medicine,* vol. 351, pp. 781-791, 2004/08/19 2004.
[51] G. T. Budd, M. Cristofanilli, M. J. Ellis, A. Stopeck, E. Borden, M. C. Miller, *et al.*, "Circulating tumor cells versus imaging—predicting overall survival in metastatic breast cancer," *Clinical Cancer Research,* vol. 12, pp. 6403-6409, 2006.
[52] S. J. Cohen, C. J. A. Punt, N. Iannotti, B. H. Saidman, K. D. Sabbath, N. Y. Gabrail, *et al.*, "Relationship of circulating tumor cells to tumor response, progression-free survival, and overall survival in patients with metastatic colorectal cancer," *Journal of Clinical Oncology,* vol. 26, pp. 3213-3221, 2008.
[53] J. S. de Bono, H. I. Scher, R. B. Montgomery, C. Parker, M. C. Miller, H. Tissing, *et al.*, "Circulating tumor cells predict survival benefit from treatment in metastatic castration-resistant prostate cancer," *Clinical Cancer Research,* vol. 14, pp. 6302-6309, 2008.
[54] D. F. Hayes, M. Cristofanilli, G. T. Budd, M. J. Ellis, A. Stopeck, M. C. Miller, *et al.*, "Circulating tumor cells at each follow-up time point during therapy of metastatic breast cancer patients predict progression-free and overall survival," *Clinical Cancer Research,* vol. 12, pp. 4218-4224, 2006.
[55] J. G. Moreno, M. C. Miller, S. Gross, W. J. Allard, L. G. Gomella, and L. W. M. M. Terstappen, "Circulating tumor cells predict survival in patients with metastatic prostate cancer," *Urology,* vol. 65, pp. 713-718, 2005.
[56] M. Yu, A. Bardia, B. S. Wittner, S. L. Stott, M. E. Smas, D. T. Ting, *et al.*, "Circulating breast tumor cells exhibit dynamic changes in epithelial and mesenchymal composition," *science,* vol. 339, pp. 580-584, 2013.

[57] M. Yu, D. T. Ting, S. L. Stott, B. S. Wittner, F. Ozsolak, S. Paul, *et al*., "RNA sequencing of pancreatic circulating tumour cells implicates WNT signalling in metastasis," *Nature,* 2012.

[58] S. Wang, H. Wang, J. Jiao, K. J. Chen, G. E. Owens, K. i. Kamei, *et al*., "Three−Dimensional Nanostructured Substrates toward Efficient Capture of Circulating Tumor Cells," *Angewandte Chemie,* vol. 121, pp. 9132-9135, 2009.

[59] S. Mittal, I. Y. Wong, W. M. Deen, and M. Toner, "Antibody-functionalized fluid-permeable surfaces for rolling cell capture at high flow rates," *Biophysical journal,* vol. 102, pp. 721-730, 2012.

[60] S. Mittal, I. Y. Wong, A. A. Yanik, W. M. Deen, and M. Toner, "Discontinuous Nanoporous Membranes Reduce Non−Specific Fouling for Immunoaffinity Cell Capture," *Small,* 2013.

[61] J. Yang, Y. Huang, X.-B. Wang, F. F. Becker, and P. R. C. Gascoyne, "Cell Separation on Microfabricated Electrodes Using Dielectrophoretic/Gravitational Field-Flow Fractionation," *Analytical Chemistry,* vol. 71, pp. 911-918, 1999/03/01 1999.

[62] S. Shim, P. Gascoyne, J. Noshari, and K. S. Hale, "Dynamic physical properties of dissociated tumor cells revealed by dielectrophoretic field-flow fractionation," *Integrative Biology,* vol. 3, pp. 850-862, 2011.

[63] L. Zabaglo, M. G. Ormerod, M. Parton, A. Ring, I. E. Smith, and M. Dowsett, "Cell filtration−laser scanning cytometry for the characterisation of circulating breast cancer cells," *Cytometry Part A,* vol. 55, pp. 102-108, 2003.

[64] T. Matsunaga, M. Hosokawa, A. Arakaki, T. Taguchi, T. Mori, T. Tanaka, *et al*., "High-efficiency single-cell entrapment and fluorescence in situ hybridization analysis using a poly (dimethylsiloxane) microfluidic device integrated with a black poly (ethylene terephthalate) micromesh," *Analytical chemistry,* vol. 80, pp. 5139-5145, 2008.

[65] G. Vona, A. Sabile, M. Louha, V. Sitruk, S. Romana, K. Schütze, *et al*., "Isolation by size of epithelial tumor cells: a new method for the immunomorphological and molecular characterization of circulating tumor cells," *The American journal of pathology,* vol. 156, pp. 57-63, 2000.

[66] P. Rostagno, J. L. Moll, J. C. Bisconte, and C. Caldani, "Detection of rare circulating breast cancer cells by filtration cytometry and identification by DNA content: sensitivity in an experimental model," *Anticancer research,* vol. 17, pp. 2481-2485, 1997.

[67] O. Lara, X. Tong, M. Zborowski, and J. J. Chalmers, "Enrichment of rare cancer cells through depletion of normal cells using density and flow-through, immunomagnetic cell separation," *Experimental hematology,* vol. 32, pp. 891-904, 2004.

[68] R. J. Cote, P. P. Rosen, M. L. Lesser, L. J. Old, and M. P. Osborne, "Prediction of early relapse in patients with operable breast cancer by detection of occult bone marrow micrometastases," *Journal of Clinical Oncology,* vol. 9, pp. 1749-1756, 1991.

[69] M. K. Baker, K. Mikhitarian, W. Osta, K. Callahan, R. Hoda, F. Brescia, *et al*., "Molecular detection of breast cancer cells in the peripheral blood of advanced-stage breast cancer patients using multimarker real-time reverse transcription-

polymerase chain reaction and a novel porous barrier density gradient centrifugation technology," *Clinical cancer research,* vol. 9, pp. 4865-4871, 2003.

[70] S. Zheng, H. K. Lin, B. Lu, A. Williams, R. Datar, R. J. Cote*, et al.*, "3D microfilter device for viable circulating tumor cell (CTC) enrichment from blood," *Biomedical microdevices,* vol. 13, pp. 203-213, 2011.

[71] S. J. Tan, L. Yobas, G. Y. H. Lee, C. N. Ong, and C. T. Lim, "Microdevice for the isolation and enumeration of cancer cells from blood," *Biomedical microdevices,* vol. 11, pp. 883-892, 2009.

[72] J. Takagi, M. Yamada, M. Yasuda, and M. Seki, "Continuous particle separation in a microchannel having asymmetrically arranged multiple branches," *Lab on a Chip,* vol. 5, pp. 778-784, 2005.

[73] J. Zhou, S. Kasper, and I. Papautsky, "Enhanced size-dependent trapping of particles using microvortices," *Microfluidics and Nanofluidics,* pp. 1-13, 2013.

[74] M. E. Warkiani, G. Guan, K. B. Luan, W. C. Lee, A. A. S. Bhagat, P. K. Chaudhuri*, et al.*, "Slanted spiral microfluidics for the ultra-fast, label-free isolation of circulating tumor cells," *Lab on a Chip,* 2014.

[75] G. Guan, L. Wu, A. A. Bhagat, Z. Li, P. C. Y. Chen, S. Chao*, et al.*, "Spiral microchannel with rectangular and trapezoidal cross-sections for size based particle separation," *Scientific reports,* vol. 3, 2013.

[76] M. Zborowski, C. B. Fuh, R. Green, L. Sun, and J. J. Chalmers, "Analytical magnetapheresis of ferritin-labeled lymphocytes," *Analytical chemistry,* vol. 67, pp. 3702-3712, 1995.

[77] T. Zhu, R. Cheng, S. A. Lee, E. Rajaraman, M. A. Eiteman, T. D. Querec*, et al.*, "Continuous-flow ferrohydrodynamic sorting of particles and cells in microfluidic devices," *Microfluidics and Nanofluidics,* vol. 13, pp. 645-654, 2012.

[78] T. Zhu, D. J. Lichlyter, M. A. Haidekker, and L. Mao, "Analytical model of microfluidic transport of non-magnetic particles in ferrofluids under the influence of a permanent magnet," *Microfluidics and Nanofluidics,* vol. 10, pp. 1233-1245, 2011.

[79] J. H. Kang, S. Krause, H. Tobin, A. Mammoto, M. Kanapathipillai, and D. E. Ingber, "A combined micromagnetic-microfluidic device for rapid capture and culture of rare circulating tumor cells," *Lab on a Chip,* vol. 12, pp. 2175-2181, 2012.

[80] K. Hoshino, P. Chen, Y.-Y. Huang, and X. Zhang, "Computational analysis of microfluidic immunomagnetic rare cell separation from a particulate blood flow," *Analytical chemistry,* vol. 84, pp. 4292-4299, 2012.

[81] C.-H. Chiou, Y.-Y. Huang, M.-H. Chiang, H.-H. Lee, and G.-B. Lee, "New magnetic tweezers for investigation of the mechanical properties of single DNA molecules," *Nanotechnology,* vol. 17, p. 1217, 2006.

[82] J.-W. Choi, C. H. Ahn, S. Bhansali, and H. T. Henderson, "A new magnetic bead-based, filterless bio-separator with planar electromagnet surfaces for integrated bio-detection systems," *Sensors and Actuators B: Chemical,* vol. 68, pp. 34-39, 2000.

[83] K. Smistrup, O. Hansen, H. Bruus, and M. F. Hansen, "Magnetic separation in microfluidic systems using microfabricated electromagnets—experiments and

simulations," *Journal of Magnetism and Magnetic Materials,* vol. 293, pp. 597-604, 2005.

[84] K. Smistrup, P. T. Tang, O. Hansen, and M. F. Hansen, "Microelectromagnet for magnetic manipulation in lab-on-a-chip systems," *Journal of Magnetism and Magnetic Materials,* vol. 300, pp. 418-426, 2006.

[85] X. Yu, X. Feng, J. Hu, Z.-L. Zhang, and D.-W. Pang, "Controlling the magnetic field distribution on the micrometer scale and generation of magnetic bead patterns for microfluidic applications," *Langmuir,* vol. 27, pp. 5147-5156, 2011.

[86] M. Bu, T. B. Christensen, K. Smistrup, A. Wolff, and M. F. Hansen, "Characterization of a microfluidic magnetic bead separator for high-throughput applications," *Sensors and Actuators A: Physical,* vol. 145, pp. 430-436, 2008.

[87] A. Walther, C. Marcoux, B. Desloges, R. Grechishkin, D. Givord, and N. M. Dempsey, "Micro-patterning of NdFeB and SmCo magnet films for integration into micro-electro-mechanical-systems," *Journal of Magnetism and Magnetic Materials,* vol. 321, pp. 590-594, 2009.

[88] N. M. Dempsey, A. Walther, F. May, D. Givord, K. Khlopkov, and O. Gutfleisch, "High performance hard magnetic NdFeB thick films for integration into micro-electro-mechanical systems," *Applied Physics Letters,* vol. 90, pp. 092509-092509, 2007.

[89] D. Nawarathna, N. Norouzi, J. McLane, H. Sharma, N. Sharac, T. Grant, *et al.*, "Shrink-induced sorting using integrated nanoscale magnetic traps," *Applied physics letters,* vol. 102, pp. 063504-063504, 2013.

[90] F. Dumas-Bouchiat, L.-F. Zanini, M. Kustov, N. M. Dempsey, R. Grechishkin, K. Hasselbach, *et al.*, "Thermomagnetically patterned micromagnets," *Applied Physics Letters,* vol. 96, pp. 102511-102511, 2010.

[91] L.-F. Zanini, N. M. Dempsey, D. Givord, G. Reyne, and F. Dumas-Bouchiat, "Autonomous micro-magnet based systems for highly efficient magnetic separation," *Applied Physics Letters,* vol. 99, pp. 232504-232504, 2011.

[92] J. Xia, X. Chen, C. Z. Zhou, Y. G. Li, and Z. H. Peng, "Development of a low-cost magnetic microfluidic chip for circulating tumour cell capture," *IET nanobiotechnology,* vol. 5, pp. 114-120, 2011.

[93] D. W. Inglis, R. Riehn, R. H. Austin, and J. C. Sturm, "Continuous microfluidic immunomagnetic cell separation," *Applied Physics Letters,* vol. 85, pp. 5093-5095, 2004.

[94] X. Lou, J. Qian, Y. Xiao, L. Viel, A. E. Gerdon, E. T. Lagally, *et al.*, "Micromagnetic selection of aptamers in microfluidic channels," *Proceedings of the National Academy of Sciences,* vol. 106, pp. 2989-2994, 2009.

[95] T. Deng, M. Prentiss, and G. M. Whitesides, "Fabrication of magnetic microfiltration systems using soft lithography," *Applied physics letters,* vol. 80, pp. 461-463, 2002.

[96] T. Dong, Q. Su, Z. Yang, Y. Zhang, E. B. Egeland, D. D. Gu, *et al.*, "A smart fully integrated micromachined separator with soft magnetic micro-pillar arrays for cell isolation," *Journal of Micromechanics and Microengineering,* vol. 20, p. 115021, 2010.

[97] Y. J. Liu, S. S. Guo, Z. L. Zhang, W. H. Huang, D. Baigl, M. Xie, *et al.*, "A micropillar−integrated smart microfluidic device for specific capture and sorting of cells," *Electrophoresis,* vol. 28, pp. 4713-4722, 2007.

[98] A.-E. Saliba, L. Saias, E. Psychari, N. Minc, D. Simon, F.-C. Bidard, *et al.*, "Microfluidic sorting and multimodal typing of cancer cells in self-assembled magnetic arrays," *Proceedings of the National Academy of Sciences,* vol. 107, pp. 14524-14529, 2010.

[99] O. Osman, C. Vézy, J. Pivetal, M. Frénea-Robin, N. Haddour, F. Buret, *et al.*, "A novel device for continuous flow magnetic trapping and sorting of human cells using flat micro–patterned NdFeB films."

[100] L. S. Lim, M. Hu, M. C. Huang, W. C. Cheong, A. T. L. Gan, X. L. Looi, *et al.*, "Microsieve lab-chip device for rapid enumeration and fluorescence in situ hybridization of circulating tumor cells," *Lab on a Chip,* vol. 12, pp. 4388-4396, 2012.

[101] S.-J. Dawson, D. W. Y. Tsui, M. Murtaza, H. Biggs, O. M. Rueda, S.-F. Chin, *et al.*, "Analysis of circulating tumor DNA to monitor metastatic breast cancer," *New England Journal of Medicine,* vol. 368, pp. 1199-1209, 2013.

[102] M. Pestrin, S. Bessi, F. Galardi, M. Truglia, A. Biggeri, C. Biagioni, *et al.*, "Correlation of HER2 status between primary tumors and corresponding circulating tumor cells in advanced breast cancer patients," *Breast cancer research and treatment,* vol. 118, pp. 523-530, 2009.

[103] A. Martowicz, G. Spizzo, G. Gastl, and G. Untergasser, "Phenotype-dependent effects of EpCAM expression on growth and invasion of human breast cancer cell lines," *BMC cancer,* vol. 12, p. 501, 2012.

[104] D. F. C. M. Smeets, "Historical prospective of human cytogenetics: from microscope to microarray," *Clinical Biochemistry,* vol. 37, pp. 439-446, 6// 2004.

[105] S. Ménard, E. Tagliabue, M. Campiglio, and S. M. Pupa, "Role of HER2 gene overexpression in breast carcinoma," *Journal of Cellular Physiology,* vol. 182, pp. 150-162, 2000.

[106] S. K. Muthuswamy, M. Gilman, and J. S. Brugge, "Controlled Dimerization of ErbB Receptors Provides Evidence for Differential Signaling by Homo- and Heterodimers," *Molecular and Cellular Biology,* vol. 19, pp. 6845-6857, 1999.

[107] P. P. Lee, C. Yee, P. A. Savage, L. Fong, D. Brockstedt, J. S. Weber, *et al.*, "Characterization of circulating T cells specific for tumor-associated antigens in melanoma patients," *Nature medicine,* vol. 5, pp. 677-685, 1999.

[108] D. J. Slamon, G. M. Clark, S. G. Wong, W. J. Levin, A. Ullrich, and W. L. McGuire, "Human breast cancer: correlation of relapse and survival with amplification of the HER-2/neu oncogene," *Science,* vol. 235, pp. 177-182, 1987.

[109] D. J. Slamon, W. Godolphin, L. A. Jones, J. A. Holt, S. G. Wong, D. E. Keith, *et al.*, "Studies of the HER-2/neu proto-oncogene in human breast and ovarian cancer," *Science,* vol. 244, pp. 707-712, 1989.

[110] M. F. Press, L. Bernstein, P. A. Thomas, L. F. Meisner, J.-Y. Zhou, Y. Ma, *et al.*, "HER-2/neu gene amplification characterized by fluorescence in situ hybridization: poor prognosis in node-negative breast carcinomas," *Journal of Clinical Oncology,* vol. 15, pp. 2894-2904, 1997.

[111] G. Pauletti, W. Godolphin, M. F. Press, and D. J. Slamon, "Detection and quantitation of HER-2/neu gene amplification in human breast cancer archival material using fluorescence in situ hybridization," *Oncogene,* vol. 13, p. 63, 1996.
[112] W.-R. Xing, K. W. Gilchrist, C. P. Harris, W. Samson, and L. F. Meisner, "FISH detection of HER-2/neu oncogene amplification in early onset breast cancer," *Breast cancer research and treatment,* vol. 39, pp. 203-212, 1996.
[113] P. L. Depowski, T. P. Brien, C. E. Sheehan, S. Stylos, R. L. Johnson, and J. S. Ross, "Prognostic significance of p34cdc2 cyclin-dependent kinase and MIB1 overexpression, and HER-2/neu gene amplification detected by fluorescence in situ hybridization in breast cancer," *American journal of clinical pathology,* vol. 112, pp. 459-469, 1999.
[114] B. Saffari, L. A. Jones, A. El-Naggar, J. C. Felix, J. George, and M. F. Press, "Amplification and overexpression of HER-2/neu (c-erbB2) in endometrial cancers: correlation with overall survival," *Cancer research,* vol. 55, pp. 5693-5698, 1995.
[115] G. N. Ranzani, N. S. Pellegata, C. Previderè, A. Saragoni, A. Vio, M. Maltoni, *et al.*, "Heterogeneous protooncogene amplification correlates with tumor progression and presence of metastases in gastric cancer patients," *Cancer research,* vol. 50, pp. 7811-7814, 1990.
[116] M. F. Press, M. C. Pike, V. R. Chazin, G. Hung, J. A. Udove, M. Markowicz, *et al.*, "Her-2/neu expression in node-negative breast cancer: direct tissue quantitation by computerized image analysis and association of overexpression with increased risk of recurrent disease," *Cancer Research,* vol. 53, pp. 4960-4970, 1993.
[117] Veridex, "An Introduction to the CellSearch™ System."
[118] F. Shamsipour, A. H. Zarnani, R. Ghods, M. Chamankhah, F. Forouzesh, S. Vafaei, *et al.*, "Conjugation of monoclonal antibodies to super paramagnetic iron oxide nanoparticles for detection of her2/neu antigen on breast cancer cell lines," *Avicenna Journal of Medical Biotechnology,* vol. 1, p. 27, 2009.
[119] T. A. Larson, J. Bankson, J. Aaron, and K. Sokolov, "Hybrid plasmonic magnetic nanoparticles as molecular specific agents for MRI/optical imaging and photothermal therapy of cancer cells," *Nanotechnology,* vol. 18, p. 325101, 2007.
[120] H.-M. Song, Q. Wei, Q. K. Ong, and A. Wei, "Plasmon-resonant nanoparticles and nanostars with magnetic cores: synthesis and magnetomotive imaging," *ACS nano,* vol. 4, pp. 5163-5173, 2010.
[121] Q. Wei, H.-M. Song, A. P. Leonov, J. A. Hale, D. Oh, Q. K. Ong, *et al.*, "Gyromagnetic imaging: dynamic optical contrast using gold nanostars with magnetic cores," *Journal of the American Chemical Society,* vol. 131, pp. 9728-9734, 2009.
[122] Q. A. Pankhurst, J. Connolly, S. K. Jones, and J. Dobson, "Applications of magnetic nanoparticles in biomedicine," *Journal of physics D: Applied physics,* vol. 36, p. R167, 2003.
[123] K. V. Sharp, R. J. Adrian, J. G. Santiago, and J. I. Molho, "Liquid flows in microchannels," *The MEMS Handbook, Mohamed Gad-El-Hak, editor. CRC Press, Boca Raton,* 2002.

[124] X. F. Peng and G. P. Peterson, "The effect of thermofluid and geometrical parameters on convection of liquids through rectangular microchannels," *International Journal of Heat and Mass Transfer,* vol. 38, pp. 755-758, 1995.
[125] C. W. Yung, J. Fiering, A. J. Mueller, and D. E. Ingber, "Micromagnetic–microfluidic blood cleansing device," *Lab on a Chip,* vol. 9, pp. 1171-1177, 2009.
[126] V. I. Furdui and D. J. Harrison, "Immunomagnetic T cell capture from blood for PCR analysis using microfluidic systems," *Lab on a Chip,* vol. 4, pp. 614-618, 2004.
[127] S. Karl, M. David, L. Moore, B. T. Grimberg, P. Michon, I. Mueller*, et al.*, "Enhanced detection of gametocytes by magnetic deposition microscopy predicts higher potential for Plasmodium falciparum transmission," *Malar J,* vol. 7, p. 66, 2008.
[128] K. S. Kim and J.-K. Park, "Magnetic force-based multiplexed immunoassay using superparamagnetic nanoparticles in microfluidic channel," *Lab on a Chip,* vol. 5, pp. 657-664, 2005.
[129] A. D. Stroock, S. K. W. Dertinger, A. Ajdari, I. Mezić, H. A. Stone, and G. M. Whitesides, "Chaotic mixer for microchannels," *Science,* vol. 295, pp. 647-651, 2002.
[130] Y.-y. Huang, P. Chen, K. Hoshino, C.-h. Wu, N. Lane, M. Huebschman*, et al.*, "PATTERNED NANOMAGNETS ON-CHIP FOR SCREENING CIRCULATING TUMOR CELLS IN BLOOD."
[131] K.-H. Han and A. Bruno Frazier, "Continuous magnetophoretic separation of blood cells in microdevice format," *Journal of Applied Physics,* vol. 96, pp. 5797-5802, 2004.
[132] A. B. Al-Mehdi, K. Tozawa, A. B. Fisher, L. Shientag, A. Lee, and R. J. Muschel, "Intravascular origin of metastasis from the proliferation of endothelium-attached tumor cells: a new model for metastasis," *Nature medicine,* vol. 6, pp. 100-102, 2000.
[133] P. Uva, A. Lahm, A. Sbardellati, A. Grigoriadis, A. Tutt, and E. de Rinaldis, "Comparative Membranome expression analysis in primary tumors and derived cell lines," *PloS one,* vol. 5, p. e11742, 2010.
[134] D. C. Lazar, E. H. Cho, M. S. Luttgen, T. J. Metzner, M. L. Uson, M. Torrey*, et al.*, "Cytometric comparisons between circulating tumor cells from prostate cancer patients and the prostate-tumor-derived LNCaP cell line," *Physical biology,* vol. 9, p. 016002, 2012.
[135] S. J. Cohen, R. K. Alpaugh, S. Gross, S. M. O'Hara, D. A. Smirnov, L. W. M. M. Terstappen*, et al.*, "Isolation and characterization of circulating tumor cells in patients with metastatic colorectal cancer," *Clinical colorectal cancer,* vol. 6, pp. 125-132, 2006.
[136] T. J. Pelkey, H. F. Frierson, and D. E. Bruns, "Molecular and immunological detection of circulating tumor cells and micrometastases from solid tumors," *Clinical chemistry,* vol. 42, pp. 1369-1381, 1996.
[137] H. S. Hochster, L. L. Hart, R. K. Ramanathan, B. H. Childs, J. D. Hainsworth, A. L. Cohn*, et al.*, "Safety and efficacy of oxaliplatin and fluoropyrimidine regimens with or without bevacizumab as first-line treatment of metastatic colorectal

cancer: results of the TREE Study," *Journal of Clinical Oncology,* vol. 26, pp. 3523-3529, 2008.

[138] H. Hurwitz, L. Fehrenbacher, W. Novotny, T. Cartwright, J. Hainsworth, W. Heim, *et al*., "Bevacizumab plus irinotecan, fluorouracil, and leucovorin for metastatic colorectal cancer," *New England journal of medicine,* vol. 350, pp. 2335-2342, 2004.

[139] A. M. Sieuwerts, J. Kraan, J. Bolt, P. van der Spoel, F. Elstrodt, M. Schutte, *et al*., "Anti-epithelial cell adhesion molecule antibodies and the detection of circulating normal-like breast tumor cells," *Journal of the National Cancer Institute,* vol. 101, pp. 61-66, 2009.

[140] B. Mostert, J. Kraan, J. Bolt-de Vries, P. van der Spoel, A. M. Sieuwerts, M. Schutte, *et al*., "Detection of circulating tumor cells in breast cancer may improve through enrichment with anti-CD146," *Breast cancer research and treatment,* vol. 127, pp. 33-41, 2011.

[141] B. Aktas, M. Tewes, T. Fehm, S. Hauch, R. Kimmig, and S. Kasimir-Bauer, "Stem cell and epithelial-mesenchymal transition markers are frequently overexpressed in circulating tumor cells of metastatic breast cancer patients," *Breast Cancer Res,* vol. 11, p. R46, 2009.

[142] T. Reya, S. J. Morrison, M. F. Clarke, and I. L. Weissman, "Stem cells, cancer, and cancer stem cells," *nature,* vol. 414, pp. 105-111, 2001.

[143] T. Fehm, N. Krawczyk, E.-F. Solomayer, G. Becker-Pergola, S. Dürr-Störzer, H. Neubauer, *et al*., "ERalpha-status of disseminated tumour cells in bone marrow of primary breast cancer patients," *Breast Cancer Research,* vol. 10, p. R76, 2008.

[144] M. Al-Hajj, M. S. Wicha, A. Benito-Hernandez, S. J. Morrison, and M. F. Clarke, "Prospective identification of tumorigenic breast cancer cells," *Proceedings of the National Academy of Sciences,* vol. 100, pp. 3983-3988, 2003.

[145] M. Balic, H. Lin, L. Young, D. Hawes, A. Giuliano, G. McNamara, *et al*., "Most early disseminated cancer cells detected in bone marrow of breast cancer patients have a putative breast cancer stem cell phenotype," *Clinical Cancer Research,* vol. 12, pp. 5615-5621, 2006.

Vita

Yu-Yen Huang was born in Tainan, Taiwan. He received the B.S. degree in mechanical engineering from Nation Chung Cheng University, Chia-yi, Taiwan, in 2003, and the M.S. degree in engineering science from National Cheng Kung University, Tainan, Taiwan, in 2005.

He enrolled in the Ph.D. program at the Department of Biomedical Engineering, the University of Texas at Austin, in September 2008. His main research is focused on the development of the immunomagnetic microfluidic chip based detection system for rare cancer cell study supervised by Professor John X.J. Zhang. He has more than 10 years experience in the design and fabrication of micro-electro-mechanical system (MEMS) technology for optical and biological applications.

Permanent email: eric09012008@utexas.edu

This dissertation was typed by the author.